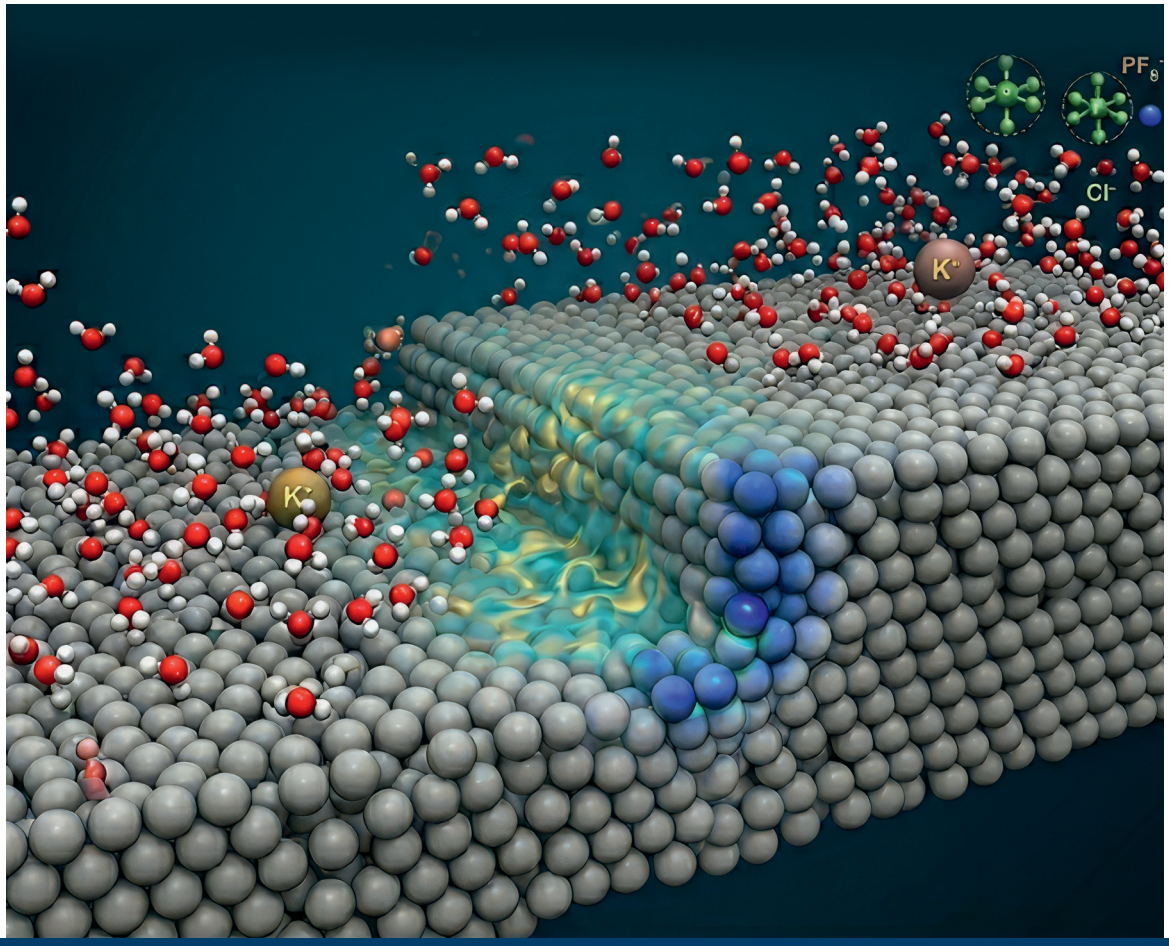

Semiclassical Thermodynamics of Metal-Solution Interfaces: A Density-Potential Functional Theory Study

Zengming Zhang

Energie & Umwelt / Energy & Environment
Band / Volume 718
ISBN 978-3-95806-947-3

Mitglied der Helmholtz-Gemeinschaft

JÜLICH
Forschungszentrum

Schriften des Forschungszentrums Jülich
Reihe Energie & Umwelt / Energy & Environment Band / Volume 718

Forschungszentrum Jülich GmbH
Institute of Energy Technologies (IET)
Theorie und computergestützte Modellierung von Materialien
in der Energietechnik (IET-3)

Semiclassical Thermodynamics of Metal-Solution Interfaces: A Density-Potential Functional Theory Study

Zengming Zhang

Schriften des Forschungszentrums Jülich
Reihe Energie & Umwelt / Energy & Environment Band / Volume 718

ISSN 1866-1793 ISBN 978-3-95806-947-3

Bibliografische Information der Deutschen Nationalbibliothek.
Die Deutsche Nationalbibliothek verzeichnet diese Publikation in der
Deutschen Nationalbibliografie; detaillierte Bibliografische Daten
sind im Internet über http://dnb.d-nb.de abrufbar.

Herausgeber und Vertrieb:	Forschungszentrum Jülich GmbH Zentralbibliothek, Verlag 52425 Jülich Tel.: +49 2461 61-5368 Fax: +49 2461 61-6103 zb-publikation@fz-juelich.de www.fz-juelich.de/zb
Umschlaggestaltung:	Grafische Medien, Forschungszentrum Jülich GmbH
Druck:	Grafische Medien, Forschungszentrum Jülich GmbH
Copyright:	Forschungszentrum Jülich 2026

Schriften des Forschungszentrums Jülich
Reihe Energie & Umwelt / Energy & Environment, Band / Volume 718

D 82 (Diss. RWTH Aachen University, 2026)

ISSN 1866-1793
ISBN 978-3-95806-946-6 (Print)
ISBN 978-3-95806-947-3 (E-Book)

Vollständig frei verfügbar über das Publikationsportal des Forschungszentrums Jülich (JuSER)
unter www.fz-juelich.de/zb/openaccess.

Erklärungen zur Dissertation

Ich erkläre hiermit eidesstattlich, dass ich die Dissertation selbstständig verfasst, alle in Anspruch genommenen Hilfen in der Dissertation angegeben habe und die schriftliche und elektronische Fassung übereinstimmen.

Ort, Datum Unterschrift

Die Grundsätze zur Sicherung guter wissenschaftlicher Praxis der RWTH Aachen habe ich eingehalten.

Ort, Datum Unterschrift

Die Veröffentlichung verletzt keine bestehenden Betriebsgeheimnisse.

Ort, Datum Unterschrift

Publications Covered in This Thesis:

Chapter 2

1. **Zhang Z**[#], Yu H[#], A. Bone R[#], S. Bandarenka*, Schwarz K*, Huang J*, et al. Getting the basics right: capacitance, entropy and stress of electrified solid/liquid interfaces. *In preparation.*

Chapter 3 & Chapter 4

2. **Zhang Z**, Huang J*, Microstructure of Electrical Double Layers at Highly Charged States[J]. *JACS Au*, 2025, 5 (7), 3453-3467.

Chapter 5

3. **Zhang Z**, Huang J*, et al. Potential of Zero Stress of Solid-Liquid Interfaces. *In preparation*.

Chapter 6

4. **Zhang Z**, Huang J*, Semiclassical Theory of Stepped Electrodes and Step Bunching, *In preparation*.

Other Publications

5. **Zhang Z**[#], Liang Z[#], Huang J*, Entropy of metal/solution interfaces: thermodynamic framework, theoretical models, and roles of interfacial water [J]. *Journal of Electrochemistry*, 2025, 2515010.

6. **Zhang Z**, Li C, Zhang J, Huang J*, et al. Dynamic response of ion transport in nanoconfined electrolytes[J]. *Nano Letters*, 2023, 23(23), 10703-10709.

7. Chen J[#], **Zhang Z**[#], Chen Y, Huang J*, et al. Structural Basis of Ultralow Capacitances at Metal–Nonaqueous Solution Interfaces[J]. *Journal of the American Chemical Society*, 2025, 147(5), 4060–4068.

*# Equal contributions; * Corresponding author*

Abstract

Electrified metal-electrolyte interfaces play a central role in electrochemical energy conversion and storage technologies. Despite extensive experimental and theoretical efforts, a comprehensive understanding of electrical double layers (EDL) remains elusive in several key aspects. In particular, existing models struggle to describe (i) the structure and thermodynamic properties of EDL at highly charged states, i.e., at potentials, far from the potential of zero charge (PZC), where many important electrocatalytic reactions take place; (ii) the surface stress and mechanical response of solid-liquid interfaces, for which classical electrocapillary concepts based on surface tension are thermodynamically inconsistent; and (iii) the EDL structure and thermodynamic driving forces at stepped metal surfaces, where atomic-scale heterogeneity strongly influences both catalytic activity and morphological stability. These limitations largely stem from the reliance on classical continuum theories that neglect the quantum-mechanical response of metal electrons and fail to consistently couple interfacial electrostatics with mechanics under constant-potential conditions.

In response to these challenges, this thesis addresses three interrelated research directions: first, the development of an improved theoretical description of EDLs at highly charged metal-solution interfaces across a wide range of electrolyte compositions; second, the establishment of a thermodynamically consistent framework for quantifying surface stress at solid-liquid interfaces under constant-potential conditions; and third, the elucidation of the thermodynamic origins of EDL formation and morphology evolution at stepped metal electrodes. To achieve these objectives, a semiclassical density-potential functional theoretical (DPFT) framework is developed and applied, which unifies the quantum-mechanical electronic response of the metal, including electron spillover, with a statistical thermodynamic description of the electrolyte. This approach enables a computationally efficient and physically consistent investigation of metal-solution interfaces under realistic electrochemical conditions.

In the first part of this work, the classical Gouy–Chapman–Stern (GCS) model is critically assessed against experimental differential double-layer capacitance data for mercury electrodes over a wide potential range and across diverse electrolyte compositions. While GCS-based descriptions perform adequately near the potential of zero charge, they fail to capture key experimental features at highly charged states, including electrolyte-dependent shifts in the potential of zero charge, asymmetric capacitance profiles, and solvent-specific effects. To overcome these limitations, the DPFT framework is refined by introducing a physically motivated description of interfacial permittivity that distinguishes free solvent molecules from those bound in ionic solvation shells, as well as by incorporating potential-dependent metal-solvent short-

range interactions and partial ion desolvation at highly charged surfaces. The resulting model quantitatively reproduces experimental capacitance profiles across different cations, anions, solvents, and concentrations, providing a robust description of EDL structure under far-from-zero-charge conditions.

In the second part, the DPFT framework is extended to investigate the thermodynamics and mechanics of solid metal-solution interfaces. By identifying surface stress, rather than surface tension, as the fundamental thermodynamic quantity for solid-liquid interfaces and by explicitly applying the Shuttleworth equation, a thermodynamically consistent methodology is established to compute potential-dependent surface stress. Within this framework, a new interfacial descriptor—the potential of zero stress (PZS)—is defined to characterize the stress-neutral state and discuss its relationship with the potential of zero free charge (PZFC). The results show that the potential dependence of surface stress is governed by the strain sensitivity of the potential of zero charge, leading to either monotonic or nonmonotonic behavior with electrode potential. By further incorporating strain-dependent metal–solvent interactions, the model reveals the key role of interfacial water in controlling the sign, magnitude, and tunability of surface stress.

In the final part of this thesis, the DPFT framework is applied to stepped metal surfaces to elucidate the thermodynamic origins of structural evolution at electrified interfaces. Using vicinal Au and Ag electrodes as model systems, the theory successfully reproduces experimentally observed trends in the PZFC, including its systematic decrease with increasing step density. Beyond global quantities such as PZFC, local potentials of zero charge are introduced to capture the intrinsic heterogeneity of the EDL at stepped surfaces. By connecting these step-induced shifts to variations in interfacial free energy, the model demonstrates that step bunching at elevated electrode potentials is thermodynamically driven at more positive potentials and strongly modulated by electrolyte composition.

Overall, this thesis provides a unified and computationally efficient theoretical framework for describing interfacial thermodynamics at electrified metal-solution interfaces under constant-potential conditions. Key advances include the identification of partial ion desolvation as a governing mechanism at highly charged surfaces, the introduction of the PZS as a fundamental mechanical descriptor for solid-liquid interfaces, and the establishment of a thermodynamic mechanism for step bunching driven by interfacial free-energy minimization. The insights gained bridge microscopic electronic structure with macroscopic electro-mechano-chemical behavior and provide a foundation for the rational design and control of stable

and efficient electrocatalytic interfaces through electrolyte selection, potential control, and surface morphology engineering.

Zusammenfassung

Elektrifizierte Metall-Elektrolyt-Grenzflächen spielen eine zentrale Rolle in elektrochemischen Energieumwandlungs- und Speichertechnologien. Trotz umfangreicher experimenteller und theoretischer Bemühungen bleibt ein umfassendes Verständnis der elektrischen Doppelschichten (Electrical Double Layers, EDL) in mehreren Schlüsselaspekten schwer fassbar. Insbesondere haben bestehende Modelle Schwierigkeiten mit der Beschreibung (i) der Struktur und der thermodynamischen Eigenschaften von EDL in stark geladenen Zuständen, d. h. bei Potenzialen weit entfernt vom Ladungsnullpunkt (Potential of Zero Charge, PZC), wo viele wichtige elektrokatalytische Reaktionen stattfinden; (ii) des Oberflächenstresses und der mechanischen Reaktion von Fest-Flüssig-Grenzflächen, für die klassische elektrokapillare Konzepte, die auf der Oberflächenspannung basieren, thermodynamisch inkonsistent sind; und (iii) der EDL-Struktur und der thermodynamischen Antriebskräfte an gestuften Metalloberflächen, wo die Heterogenität auf atomarer Ebene sowohl die katalytische Aktivität als auch die morphologische Stabilität stark beeinflusst. Diese Einschränkungen resultieren größtenteils aus der Abhängigkeit von klassischen Kontinuumstheorien, die die quantenmechanische Reaktion der Metallelektronen vernachlässigen und es versäumen, die Grenzflächenelektrostatik unter Bedingungen konstanten Potenzials konsistent mit der Mechanik zu koppeln.

Als Reaktion auf diese Herausforderungen befasst sich diese Arbeit mit drei zusammenhängenden Forschungsrichtungen: erstens der Entwicklung einer verbesserten theoretischen Beschreibung von EDLs an stark geladenen Metall-Lösungs-Grenzflächen über einen weiten Bereich von Elektrolytzusammensetzungen; zweitens der Etablierung eines thermodynamisch konsistenten Rahmens zur Quantifizierung des Oberflächenstresses an Fest-Flüssig-Grenzflächen unter Bedingungen konstanten Potenzials; und drittens der Aufklärung der thermodynamischen Ursprünge der EDL-Bildung und der Morphologieentwicklung an gestuften Metallelektroden. Um diese Ziele zu erreichen, wird ein semiklassischer dichte-potenzial-funktional-theoretischer (DPFT) Rahmen entwickelt und angewendet, der die quantenmechanische elektronische Reaktion des Metalls, einschließlich des Elektronen-Spillovers, mit einer statistisch-thermodynamischen Beschreibung des Elektrolyten vereint. Dieser Ansatz ermöglicht eine recheneffiziente und physikalisch konsistente Untersuchung von Metall-Lösungs-Grenzflächen unter realistischen elektrochemischen Bedingungen.

Im ersten Teil dieser Arbeit wird das klassische Gouy-Chapman-Stern (GCS)-Modell kritisch anhand experimenteller Daten zur differenziellen Doppelschichtkapazität für Quecksilberelektroden über einen weiten Potenzialbereich und über verschiedene Elektrolytzusammensetzungen hinweg bewertet.

Während GCS-basierte Beschreibungen in der Nähe des Ladungsnullpunkts angemessene Ergebnisse liefern, gelingt es ihnen nicht, wichtige experimentelle Merkmale in stark geladenen Zuständen zu erfassen, einschließlich elektrolytabhängiger Verschiebungen des Ladungsnullpunkts, asymmetrischer Kapazitätsprofile und lösungsmittelspezifischer Effekte. Um diese Einschränkungen zu überwinden, wird der DPFT-Rahmen durch die Einführung einer physikalisch motivierten Beschreibung der Grenzflächenpermittivität verfeinert, die zwischen freien Lösungsmittelmolekülen und solchen, die in ionischen Solvatationshüllen gebunden sind, unterscheidet, sowie durch die Einbeziehung potenzialabhängiger Metall-Lösungsmittel-kurzreichweitiger Wechselwirkungen und der partiellen Ionendesolvatation an stark geladenen Oberflächen. Das resultierende Modell reproduziert quantitativ experimentelle Kapazitätsprofile über verschiedene Kationen, Anionen, Lösungsmittel und Konzentrationen hinweg und liefert eine robuste Beschreibung der EDL-Struktur unter Bedingungen weit entfernt vom Ladungsnullpunkt.

Im zweiten Teil wird der DPFT-Rahmen erweitert, um die Thermodynamik und Mechanik von festen Metall-Lösungs-Grenzflächen zu untersuchen. Indem der Oberflächenstress (surface stress) und nicht die Oberflächenspannung (surface tension) als grundlegende thermodynamische Größe für Fest-Flüssig-Grenzflächen identifiziert wird und durch die explizite Anwendung der Shuttleworth-Gleichung, wird eine thermodynamisch konsistente Methodik zur Berechnung des potenzialabhängigen Oberflächenstresses etabliert. Innerhalb dieses Rahmens wird ein neuer Grenzflächendeskriptor – das Potenzial des Nullstresses (potential of zero stress, PZS) – definiert, um den spannungsneutralen Zustand zu charakterisieren und seine Beziehung zum Potenzial der freien Nullladung (potential of zero free charge, PZFC) zu diskutieren. Die Ergebnisse zeigen, dass die Potenzialabhängigkeit des Oberflächenstresses von der Dehnungsempfindlichkeit (strain sensitivity) des Ladungsnullpunkts bestimmt wird, was zu einem entweder monotonen oder nicht-monotonen Verhalten mit dem Elektrodenpotenzial führt. Durch die weitere Einbeziehung dehnungsabhängiger Metall-Lösungsmittel-Wechselwirkungen offenbart das Modell die Schlüsselrolle von Grenzflächenwasser bei der Steuerung von Vorzeichen, Größe und Abstimmbarkeit des Oberflächenstresses.

Im letzten Teil dieser Arbeit wird der DPFT-Rahmen auf gestufte Metalloberflächen angewendet, um die thermodynamischen Ursprünge der Strukturentwicklung an elektrifizierten Grenzflächen aufzuklären. Unter Verwendung von vizinalen Au- und Ag-Elektroden als Modellsysteme reproduziert die Theorie erfolgreich die experimentell beobachteten Trends im PZFC, einschließlich seiner systematischen Abnahme mit zunehmender Stufendichte. Über globale Größen wie das PZFC hinaus werden lokale

Ladungsnullpunkte eingeführt, um die intrinsische Heterogenität der EDL an gestuften Oberflächen zu erfassen. Durch die Verknüpfung dieser stufeninduzierten Verschiebungen mit Schwankungen der freien Grenzflächenenergie zeigt das Modell, dass Step-Bunching (Stufenbündelung) bei erhöhten Elektrodenpotenzialen thermodynamisch angetrieben und stark durch die Elektrolytzusammensetzung moduliert wird.

Insgesamt bietet diese Arbeit einen einheitlichen und recheneffizienten theoretischen Rahmen zur Beschreibung der Grenzflächenthermodynamik an elektrifizierten Metall-Lösungs-Grenzflächen unter Bedingungen konstanten Potenzials. Zu den wichtigsten Fortschritten gehören die Identifizierung der partiellen Ionendesolvatation als maßgeblichen Mechanismus an stark geladenen Oberflächen, die Einführung des PZS als grundlegenden mechanischen Deskriptor für Fest-Flüssig-Grenzflächen und die Etablierung eines thermodynamischen Mechanismus für Step-Bunching, angetrieben durch die Minimierung der freien Grenzflächenenergie. Die gewonnenen Erkenntnisse schlagen eine Brücke zwischen mikroskopischer elektronischer Struktur und makroskopischem elektro-mechano-chemischen Verhalten und bilden eine Grundlage für das rationale Design und die Kontrolle stabiler und effizienter elektrokatalytischer Grenzflächen durch Elektrolytauswahl, Potenzialsteuerung und Oberflächenmorphologie-Engineering.

Table of Contents

Chapter 1. Introduction

1.1. Motivation

The electrical double layer (EDL) is an interfacial region formed between an electronic conductor, typically a metal, and an adjacent ionic conductor, mostly an electrolyte solution, playing a fundamental role in electrochemical energy conversion and storage systems[1–8]. Its thermodynamic properties, such as double-layer capacitance, C_{dl}, and mechanical properties, such as surface stress, g_{ss}, arise from mixed quantum- and classical mechanical interactions between metal electrons and the surrounding ions and solvent. These hybrid quantum and classical interactions lead to pronounced spatial variations in ion concentration, electrostatic potential, and dielectric permittivity in the vicinity of the interface. These distributions regulate physicochemical processes and electro-mechano-chemical properties of solid-liquid interfaces. For instance, the resulting local reaction environment critically influences the kinetics and selectivity of electrocatalytic reactions, thereby directly impacting the performance of electrochemical devices[2,9].

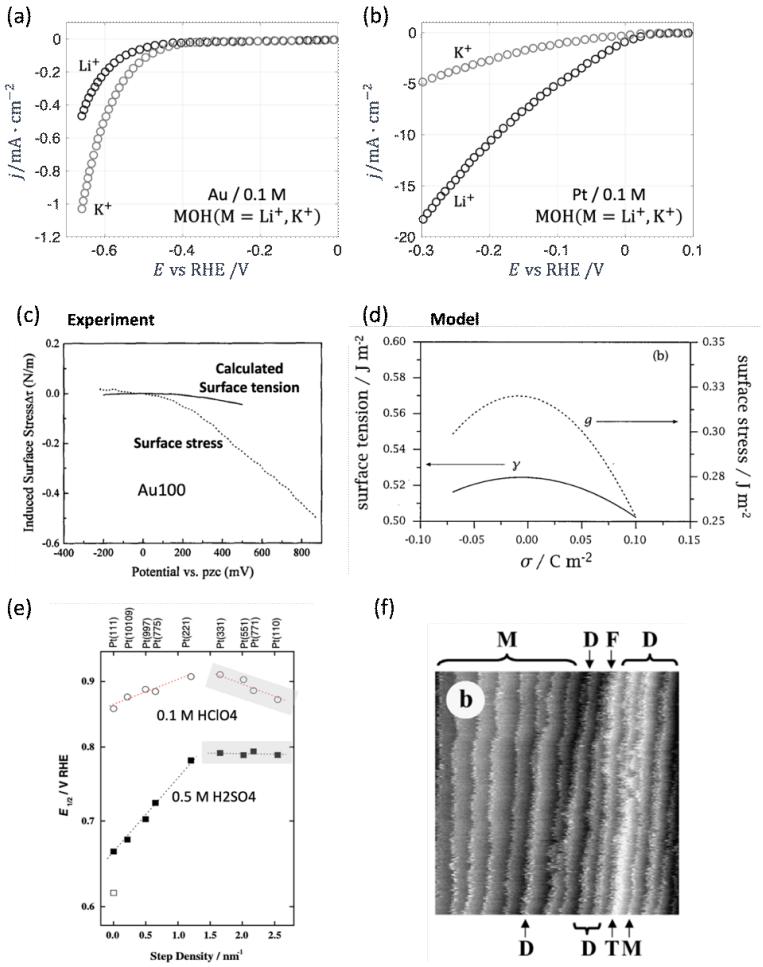

Figure 1. (a, b) Experimental observations of inversions in cation-dependent HER activity under alkaline conditions. (c, d) Comparison between surface stress and surface tension from experimental observations and model calculations. (e) Correlations between step density and reactivity of stepped Pt electrodes and (f) STM image of stepped Ag electrode with the letters ''M'', ''D'', ''T'', and ''F'' indicating mono-, double-, triple- and four-layer steps. Subplot (a) and (b) are reproduced with permission from ref[10]; Subplot (c) and (d) are reproduced with permission from ref[11] and ref[12], respectively. Subplot (e) and (f) are reproduced with permission from ref[13,14] and ref[15], respectively.

1.1.1. Highly charged states

Notable EDL effects are seen even for the simplest electrocatalytic reaction, the hydrogen evolution reaction (HER), on the simplest electrode (Au) and the simplest electrolytes (alkali metals).For example, Goyal et al.[16] and Monteiro et al.[10] demonstrated that K^+ promotes the HER under alkaline conditions on gold electrode at low overpotentials, but inhibits the reaction at more cathodic potentials, as shown in Figure 1(a, b). However, the mechanisms behind cation effects remain a topic of debate[17,18] and the proposed mechanisms for cation effects include the blocking of catalytic sites by cations, chemical interactions between cations and reaction intermediates, and alterations in the interfacial water structure[19]. Yet, the large consensus is that it is crucial to understand the structure and properties of EDL under realistic reaction conditions.

Despite the large body of recent experimental and computational research on unraveling the electrolyte effects in electrocatalysis, the contemporary understanding of EDL formation is rooted in the classical EDL theory developed from the 1850s to the 1950s[9]. The classical Gouy-Chapman-Stern (GCS) model is the primary framework of understanding EDLs. The GCS model describes the EDL as a dielectric continuum with point-like ions. The EDL comprises an inner layer between the metal surface edge and the central plane of rigidly aligned counter ions (Helmholtz plane, HP), and an outer diffuse layer in which the ion distribution is determined by the competition between electrostatic force and thermal motion. The differential double-layer capacitance, C_{dl}, is a fundamental lumped parameter reflecting the EDL structure and all its properties.[20] The equivalent thickness of the EDL decreases due to counterion accumulation and then increases due to counterion overcrowding when the electrode potential, E_{M}, deviates from the potential of zero charge (PZC, E_{pzc}). A camel-shaped C_{dl} profile is very commonly observed in dilute solutions. The minimum point of the C_{dl} versus potential profile is very close to the E_{pzc}[21,22]. The cathodic peak of the C_{dl} profile is attributed to cation overcrowding, while the anodic peak anion overcrowding. Larger ion sizes lower the peak height. In highly concentrated solutions, the C_{dl} profile becomes bell-shaped, indicating a continuous increase in the EDL thickness as E_{M} moves away from E_{pzc}, as elucidated by Kornyshev[23]. We note more recent works reveal that the two peaks are ascribed mainly to orientational polarization of interfacial water molecules[24,25].

Recent attention has largely focused on the EDL in the potential range near the PZC[26]. For instance, the studies by Ojha et. al. found that the Gouy-Chapman minimum is not observed in Pt(111)-$HClO_4$ aqueous interfaces until the electrolyte concentration is decreased to 0.1 mM[27]. However, the EDL properties at potentials far away from the vicinity of the PZC is rarely studied, partly due to the difficulty in accurately

measuring C_{dl} in a wide potential range; this is a severe oversight as important electrocatalytic reduction reactions occur at significantly more negative potentials than the PZC. For example, the onset potentials of HER on Pd(111), Pt(111), Ag(111) and Au(111) in 0.1M aqueous solution with $\mathrm{pH} = 13$ are about $-0.87, -0.74, -1.37,$ and -1.32 V vs. SHE scales, respectively[28], while the corresponding PZCs are $0.1, 0.3, -0.5,$ and 0.5 V_{SHE}[29]. Similarly, the onset potential of CO_2 reduction reaction on Cu(111) in 0.05M H_2SO_4 solution ($\mathrm{pH} = 1$) is around -0.86 V_{SHE}[30], while the PZC of Cu(111) is around 0.7 V_{SHE}[31]. The onset potential of CO_2 reduction reaction (CO_2RR) on Au(111) in 0.1M H_2SO_4 solution ($\mathrm{pH} = 3$) is about -0.5 V_{SHE}[32], around 1 V negative of its PZC.

1.1.2. Surface stress

The GCS model was originally developed for the EDL at liquid-liquid interfaces[33–37]. However, it is widely applied to solid-liquid interfaces in practical electrochemical applications[23,38,37,39,40]. This widespread use masks a critical issue: the thermodynamic assumptions underlying the GCS model are not directly transferable to solid-liquid interfaces[41–44,12,8]. Specifically, surface tension or interfacial free energy, which governs liquid-liquid systems, is not directly measurable on solid surfaces and lacks a consistent definition, due to the fact that surface atoms cannot move smoothly like in the liquid metal[45,41,42,46], as shown in Figure 1(c). This discrepancy has led to significant and ongoing debate in the literature[42,44,46]. A growing consensus now recognizes that surface stress, rather than interfacial tension, should serve as the fundamental thermodynamic quantity for solid-liquid interfaces[43,12,47,8].

Surface stress of solid-liquid interfaces remains challenging to quantify both experimentally[48–50,43,11,51] and theoretically[52–55,12,8]. Microcantilever-based methods[49,48,50] provide an experimental access. In this method, a free-standing single-crystal cantilever was clamped within an electrochemical cell, and its bending was detected using the servo voltage of a scanning tunneling microscope (STM) tip. By maintaining constant tunneling current and bias, deflections were directly linked to variations in interfacial stress, with sensitivity sufficient to resolve changes as small as $0.1\ \mathrm{N\ m^{-1}}$. The dependence of surface stress on electrode potential for Au(111) and Au(100) has been experimentally investigated[11,56]. These studies show that the potential-dependent variation is substantial and highly sensitive to the surface structure. Specifically, the surface stress is lower on an initially reconstructed surface than on an unreconstructed one. Moreover, the surface stress differs markedly from the surface tension, indicating that the surface tension itself varies with the elastic strain.

On the theoretical side, Needs[54] performed the first *ab initio* calculations of the surface stress tensor for Al(111) and (110) surfaces. The calculations, based on density functional theory (DFT) and the Nielsen-

Martin stress theorem, revealed that both surfaces exhibit significant tensile surface stress. This tensile stress was found to originate primarily from the reduction in electron kinetic energy at the surface due to the smoothing of electron spillover, highlighting the crucial role of the electronic response in determining surface mechanical properties.

While surface stress of metal-vacuum interfaces can be readily calculated, quantitative evaluation for metal-solution interfaces under constant-potential conditions remain scarce. Schmickler and Leiva[12] investigated the surface stress and surface tension of solid metal electrodes in contact with an electrolyte under constant-charge conditions by combining a jellium description of the metal with the GCS model for the solution. Their analysis revealed a parabolic-like dependence of surface stress with surface charge density near the PZC (see Figure 1(d)), dominated by the metal's electronic properties. However, the potential dependence of surface stress cannot be obtained by the Schmickler-Levia model. In addition, many fundamental questions related to surface stress remain elusive. For example, how do electrolyte properties, such as ionic concentration and ion identity, affect surface stress? How do metal-specific factors, including crystal facet and electron spillover, contribute to surface stress variations? Furthermore, how do mesoscale geometrical characteristics of electrodes, such as atomic steps, terraces, and other morphological heterogeneities, influence the interfacial mechanical response? Collectively, these unresolved issues highlight the need for more comprehensive modeling approaches capable of describing surface stress under realistic electrochemical conditions.

1.1.3. EDL at stepped surfaces

The EDL at stepped metal-solution interfaces plays a dual role in controlling electrocatalytic activity and surface stability under operating conditions[57–59,46,60,61], yet the thermodynamic origins of their structural evolution remain insufficiently understood. Atomic step sites on metal surfaces such as Pt[62–65], Au[66–68], and Ag[69,70] are widely recognized as highly active centers for adsorption, charge transfer, and bond activation due to their low coordination and distinct electronic structure. Stepped surfaces therefore serve as important model systems bridging ideal single-crystal electrodes and realistic, defect-rich catalysts.

Experimental studies on stepped platinum electrodes have revealed strong correlations between step density and catalytic activity, but also pronounced deviations from linear scaling relations. In particular, both the potential of zero charge and oxygen reduction reaction activity cease to scale linearly with step density once terraces become sufficiently narrow[13,14], as shown in Figure 1(e). Similar non-additive behavior has been observed for other reactions and metal surfaces[71,72], indicating that the influence of

steps extends beyond their immediate atomic vicinity. These anomalies have been attributed to strain relaxation and electronic perturbations near step edges, resulting in step bunching, as shown in Figure 1(f), which modifies the electrostatic environment and reactivity of terrace atoms and invalidates simple terrace-step additivity assumptions.

Despite these insights, a fundamental understanding of how atomic-scale surface heterogeneity modifies EDL structure and interfacial thermodynamics under constant-potential conditions remains lacking. Classical EDL models implicitly assume laterally homogeneous, planar electrodes and therefore cannot capture step-induced dipoles, long-range electrostatic interactions between steps, or their coupling to electrolyte structure. Consequently, key interfacial quantities such as the potential of zero charge, interfacial free energy, and surface stress cannot be consistently defined for stepped electrodes. Moreover, experimental observations of potential-dependent step motion, step bunching, and electrochemically induced surface reconstruction suggest that stepped surfaces evolve dynamically to minimize interfacial free energy, yet the underlying thermodynamic driving forces remain unresolved.

1.2. Objective

The primary objective of this doctoral project is to extent our understanding of metal-solution interfaces from near-zero-charge to far-from-zero-charge conditions, from electrical properties to mechanical properties, from smooth surfaces to stepped surfaces, using double-layer capacitance, C_{dl}, surface tension, γ, and surface stress, g, as key descriptors. The focus is on realistic electrochemical conditions, particularly under highly charged states and potential-dependent morphological changes in the electrode surface due to reconstruction. This enhanced understanding will provide critical insights into designing efficient electrocatalytic systems. The overall goal leads to three specific objectives.

The first objective is to develop a semiclassical, mesoscopic model for EDL across a wide range of electrolyte compositions and potential conditions. While the classical GCS model can well describe the differential near the PZC with several empirical parameters, it fails to capture the C_{dl} profile in a wide potential range and it is insufficient to capture the variations in the C_{dl} profiles with varying electrolyte cations, anions, and solvent. Currently, DFT is the working horse of atomistic modeling of EDLs, offering unbiased insights into the electronic and geometric structures of the EDL. However, the description of the electrolyte solution is often oversimplified and the treatment of the electrode potential is inaccurate and computationally expensive. In short, the DFT-based approach is not mature to study the EDL microstructure in large parametric space.[73] Therefore, there is a need to develop a computationally-efficient, constant-potential theoretical methodology to understand the microstructure of the EDL near highly-charged electrodes and varying electrolyte parameters.

The second objective of this thesis is to advance the fundamental understanding of surface stress at solid metal-solution interfaces under constant-potential conditions. In contrast to liquid metal interfaces, classical electrocapillary concepts based on surface tension are not thermodynamically adequate for solids, as elastic strain and electronic redistribution contribute directly to the interfacial free energy. As a result, both experimental quantification and theoretical prediction of surface stress in electrochemical environments remain challenging, particularly under realistic constant-potential conditions. To address these challenges, this work employs the DPFT framework, which combines an orbital-free quantum mechanical description of metallic electrons with a classical statistical field treatment of the electrolyte[74,75]. The DPFT approach has been shown to accurately capture the trends of the C_{dl} profiles of Hg[76], Ag[74] and Au[77] single crystals across a wide range of electrolyte compositions and electrode potentials, while remaining computationally efficient. By extending this framework to include elastic strain and applying the Shuttleworth relation, this thesis establishes a thermodynamically consistent methodology

to compute potential-dependent surface stress and to elucidate the coupling between electronic structure, electrolyte composition, and mechanical stability at electrified solid-liquid interfaces.

The third objective is to advance our understanding in origin of step bunching at metal-solution interfaces under realistic electrochemical conditions. In contrast to well-established descriptions of step bunching for vicinal surfaces in vacuum, the thermodynamic driving forces governing morphological stability at electrified solid-liquid interfaces remain poorly understood. In this part, interfacial free energy is identified as a central thermodynamic descriptor linking EDL structure, step-induced dipoles, and surface morphology at constant potential. Using the DPFT framework, this study systematically investigates how step density, electrode potential, and electrolyte composition influence the PZFC and the relative stability of single- and multi-step configurations. By quantitatively connecting step dipole moments and interfacial free-energy differences to step bunching behavior, this objective aims to establish a thermodynamic foundation for understanding morphology evolution at stepped electrodes and to provide predictive insight into how electrochemical conditions can be used to control surface stability in electrocatalytic systems.

1.3. Methodology

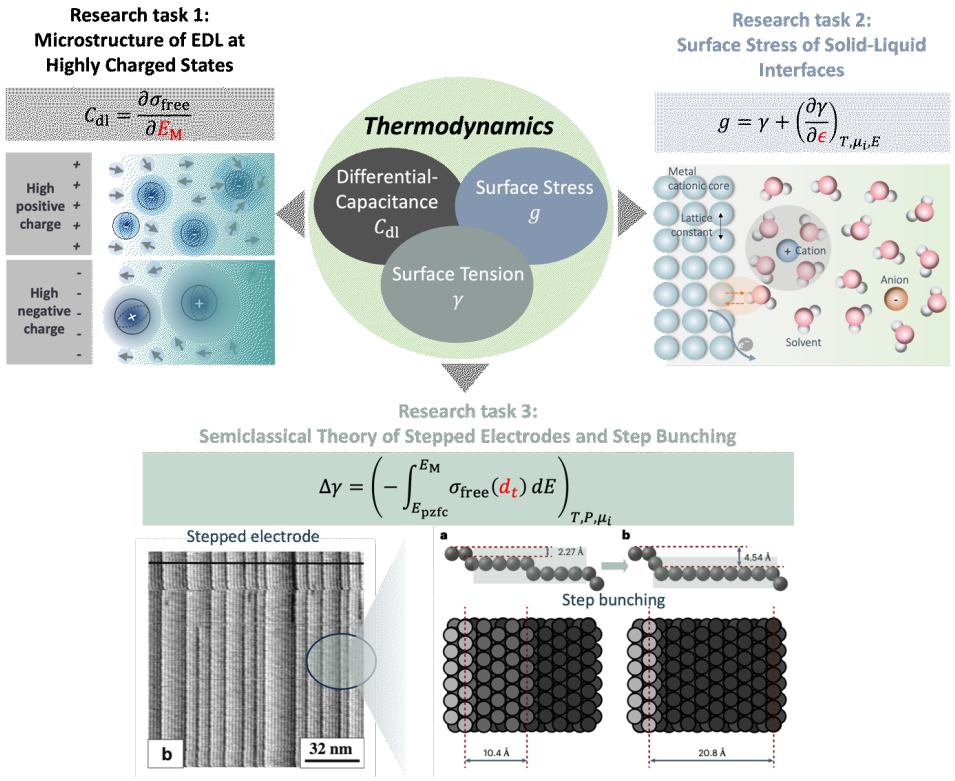

Figure 2. Research frameworks of this PhD project. This PhD project is divided into three research tasks. Research task1: Microstructure of EDL at highly charged states; Research task 2: Surface stress of solid-liquid interfaces; Research task 3: Semiclassical theory of stepped electrodes and step bunching.

In the research task 1, we choose mercury as the model electrode because the C_{dl} profiles in an extended potential range exist have been measured for this electrode[37,78]. In addition, the C_{dl} profiles have been measured in a wide parametric space of the electrolyte solution, including different cations like Na^+ and K^+, different weakly adsorbing anions like F^- and PF_6^-, and different solvent molecules like water and dimethyl sulfoxide (DMSO), as shown in the left-hand-side of the Figure 2. We start our analysis by addressing an obvious question: how good is the classical GCS model for the mercury EDL in a wide potential range in various electrolyte solutions? Then, to further improve over the GCS model, we employ

the recent semiclassical DPFT approach[74,75], which has been employed to understand the C_{dl} profiles of Ag single crystals in aqueous solutions[74] and Au single crystals in nonaqueous solutions[77]. The DPFT approach integrates an orbital-free quantum mechanical description of the metal electrons and a classical statistical field description of the electrolyte solution, providing a computationally efficient description of the EDL[74,75,77]. In achieving a quantitative agreement between the DPFT model and experimental C_{dl} profiles, the DPFT model is improved by introducing two key physical phenomena that are missing in classical EDL models, namely, the dependency of metal-solvent short-range interactions on the electrode potential and the ion partial desolvation at highly charged surfaces. Leveraging a refined DPFT model that incorporates these two critical physical effects, we proceed to evaluate experimental C_{dl} profiles across a spectrum of ion concentrations within various electrolyte solutions. This analysis encompasses diverse types of cations, anions, and solvent molecules. By systematically considering these effects, the improved DPFT model offers an efficacious tool to understand the EDL structure under more realistic reaction conditions.

In research task 2, we study the potential-dependent surface stress of solid metal-solutions interfaces, as illustrated in the right-hand-side of the Figure 2. In contrast to liquid metal electrodes, where surface tension provides a well-defined thermodynamic quantity, solid electrodes exhibit elastic resistance to deformation, requiring a more careful thermodynamic treatment. We therefore begin by establishing a consistent thermodynamic framework within the DPFT model, in which key interfacial quantities—including surface tension γ, interfacial free energy F_{int}, elastic strain ϵ, and surface stress g—are rigorously defined under constant-potential conditions. To validate the applicability of the DPFT framework for solid electrodes, we benchmark the model against experimental C_{dl} data for $\mathrm{Au}(110,111,100)/\mathrm{KPF}_6$, HClO_4[79–82] and $\mathrm{Ag}(111,100,110)/\mathrm{KPF}_6$[83–85] aqueous solution systems with weak ionic adsorption, where specific ionic adsorption is weak. This benchmarking ensures that the electrostatic structure of the EDL is accurately captured before addressing interfacial mechanical properties. We then compare alternative computational routes for evaluating surface tension and interfacial free energy to verify thermodynamic consistency and numerical robustness within the DPFT framework. Building on this validated methodology, we perform a comprehensive parametric analysis to elucidate the physical origins of surface stress at electrified solid-liquid interfaces. Specifically, we systematically examine the effects of electrolyte composition and ion concentration, electrode crystallography, kinetic energy functionals of the electron density, and surface geometry. This approach allows us to disentangle the relative contributions of electronic spillover, electrostatic forces, and elastic strain, and to identify the key factors governing potential-dependent surface stress.

Building on the insights gained from research task 2, research task 3 extends the DPFT framework to stepped metal electrodes, as shown at the bottom of Figure 2, with the goal of elucidating how atomic-scale surface heterogeneity modifies interfacial electrostatics and thermodynamics under constant-potential conditions. We first validate the model by reproducing the experimentally observed trend that the potential of zero free charge (PZFC) decreases systematically with increasing step density for vicinal metal surfaces[86,87]. This validation establishes the capability of the DPFT framework to capture step-induced electrostatic effects beyond planar electrode models.

We then quantitatively analyze how step density and electrode potential influence interfacial free energy, explicitly accounting for step-induced dipole moments and their interactions. By comparing single-step and multi-step surface configurations, we assess the thermodynamic stability of different step arrangements and identify the conditions under which step bunching becomes energetically favorable. Through this analysis, interfacial free energy is established as a key thermodynamic descriptor linking EDL structure, step-induced electrostatics, and morphology evolution at electrified interfaces under realistic electrochemical conditions.

1.4. Structure of this thesis

The remainder of this thesis is organized to progressively develop the theoretical foundations, methodological framework, and application-focused studies required to address the research objectives outlined in Chapter 1.

Chapter 2 introduces the thermodynamic framework for electrified interfaces. A clear distinction is made between liquid-liquid and solid-liquid interfaces, highlighting the different thermodynamic variables and constraints governing each system. Particular emphasis is placed on the role of surface tension, surface stress, interfacial free energy, and elastic strain, thereby establishing the conceptual basis required for the subsequent analysis of EDLs and interfacial mechanics under electrochemical conditions.

Chapter 3 presents the theoretical models employed in this work. The classical GCS model is first introduced as the conventional framework for describing EDL, together with its underlying assumptions and known limitations. This is followed by a detailed presentation of the semiclassical DPFT framework developed and applied in this thesis. The variational formulation, numerical implementation, and procedures for calculating thermodynamic quantities within DPFT are described in detail, providing the methodological foundation for all subsequent chapters.

Chapters 4-6 constitute the core of the thesis and correspond directly to the three main research tasks. In Chapter 4, the microstructure of EDL at highly charged states is investigated. By systematically comparing classical GCS predictions with refined DPFT-based models, this chapter demonstrates how potential-dependent metal-solvent interactions and partial ion desolvation give rise to experimentally observed capacitance behavior and electrolyte-specific effects under far-from-zero-charge conditions.

Chapter 5 focuses on the surface stress of electrified solid-liquid interfaces. After calibrating the DPFT framework against experimental differential capacitance data, this chapter establishes a thermodynamically consistent methodology for computing surface stress under constant-potential conditions. Distinct potential-dependent surface stress behaviors, including monotonically increasing, monotonically decreasing, and nonmonotonic behaviors, can be rationalized with different dependencies of water adsorption on the elastic strain.

In Chapter 6, the DPFT framework is extended to stepped metal-solution interfaces to investigate the thermodynamic origins of surface morphology evolution. This chapter examines the microstructure of the EDL at stepped surfaces, validates the model by reproducing experimentally observed trends in the potential of zero free charge, and quantifies the dependence of interfacial free energy on step density

and electrode potential. These results provide a thermodynamic explanation for step bunching and other electrochemically induced morphological changes.

Finally, Chapter 7 summarizes the overall conclusions of the thesis and discusses the broader implications of the results for electrocatalysis and interface design. The limitations of the present work are critically assessed, and promising directions for future research are outlined.

Chapter 2. Thermodynamic framework

*Reproduced with minor changes from '**Zhang Z.**, Bandarenka A.*, Schwarz K.*, Huang J.*, et al. Getting the basics right: capacitance, entropy and stress of electrified solid/liquid interfaces. (in preparation)'.*

2.1. Fundamental thermodynamic equations for a system

2.1.1. System specifications

An EDL is an grand-canonical interfacial system[9,88,89]. As schematically illustrated in Figure 3, the metal phase is in contact with an electron reservoir, and the electrochemical potential of electrons in the metal phase and equivalently the metal's inner electric potential, ϕ_{M}, can be controlled in experiments. The liquid region is in contact with a reservoir of electrolyte solution containing cations, anions, and solvent molecules at constant concentrations. The electric potential in the solution, ϕ_{S}, is typically referenced to the value in the bulk solution. The electrochemical potential of ionic and solvent species, denoted $\tilde{\mu}_{\mathrm{i}}$, are regulated through the bulk concentration, $n_{\mathrm{i}}^{\mathrm{b}}$, where the superscript b indicates the reservoir (bulk) phase.

Within a molecular picture of the interface, the outer Helmholtz plane (OHP) defines the middle plane of solvated ions that are closest the electrode surface. Under certain conditions, ions located at the OHP may partially shed their hydration shells and displace interfacial water molecules to establish direct contact with the electrode. This process is ion specific, referred to as specific adsorption. Chemisorption is a subcategory of specific adsorption with chemical bonds formed between the electrode and the specifically adsorbed species[90,91]. In chemisorption, the adsorbate can share electrons with the electrode to carry out the so-called partial charge transfer, resulting in the partially charged chemisorbate[92]. The centers of these specifically adsorbed ions define the inner Helmholtz plane (IHP).

The interfacial region itself has a fixed volume, V, which is negligible compared to that of the adjacent reservoirs. Its temperature, T, remains constant due to thermal equilibration with the surrounding bulk phases. Particle densities within the EDL are therefore determined by the electrochemical potentials imposed by the metal and solution reservoirs, reflecting continuous exchange of electrons, ions, and solvent molecules under grand-canonical conditions.

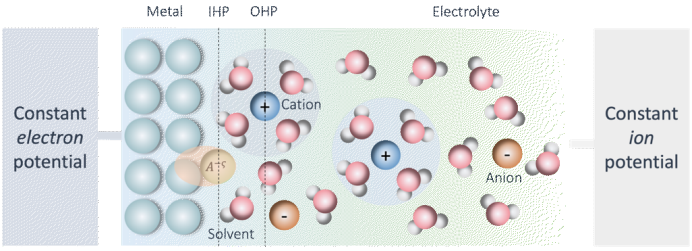

Figure 3. Schematic illustration of EDLs with partially charged chemisorbed ions ($A^{-\varsigma}$). The metal side is connected to an electron reservoir to hold the electrochemical potential of electrons constant. The solution side is connected to an electrolyte reservoir to hold the electrochemical potentials of ions and solvent constant. The solvation shells of cations and anions are explicitly shown. Bounded and free solvent molecules are treated separately. OHP is the outer Helmholtz plane, which represents the middle plane of solvated ions that are closest the electrode surface. IHP is the inner Helmholtz plane, which represents the locus of centers of these specifically adsorbed species. Reproduced with permission from ref.[88]

In the following section, we begin with reviewing the basic thermodynamics of EDLs. In the reviewing process we emphasize the different variants of surface charges, capacitances and their characteristic potentials. In addition, we discuss the difference between liquid-liquid and solid-liquid interfaces from a thermodynamic perspective, highlighting the key role of surface stress in understanding the solid-liquid interfaces.

2.1.2. Fundamental thermodynamic equations

Here we limit ourselves to ideally reversible paths of changing the EDL states. The first thermodynamic law can be expressed as,

$$dU = \delta Q - \delta W, \tag{1}$$

where U is the internal energy, Q, heat, and W, work. According to the second thermodynamic law, the change in entropy dS is equal to the heat transfer δQ divided by the temperature T,

$$dS = \delta Q/T. \tag{2}$$

Thus, we rewrite the Eq.(1) as,

$$dU - TdS = dF = -\delta W, \tag{3}$$

which serves as the definition of the Helmholtz free energy, F. The work term, $-\delta W$, can be decomposed into expansion work, $-PdV$, where P denotes the pressure, and non-expansion work. Assuming chemical work is the sole non-expansion contribution in this system, the latter is given by $\sum_{\mathrm{i}} \tilde{\mu}_{\mathrm{i}} dn_{\mathrm{i}}$. It follows that,

$$dF = \sum_{\mathrm{i}} \tilde{\mu}_{\mathrm{i}} dn_{\mathrm{i}} - PdV, \tag{4}$$

which can be rearranged as,

$$dF + PdV = \sum_{\mathrm{i}} \tilde{\mu}_{\mathrm{i}} dn_{\mathrm{i}}. \tag{5}$$

Combining the first and second thermodynamic laws gives,

$$dU = TdS + \sum_{\mathrm{i}} \tilde{\mu}_{\mathrm{i}} dn_{\mathrm{i}} - PdV. \tag{6}$$

By invoking Euler's theorem for homogeneous functions, which applies because U is an extensive property, we obtain the Euler relation,

$$U = TS + \sum_{\mathrm{i}} \tilde{\mu}_{\mathrm{i}} n_{\mathrm{i}} - PV. \tag{7}$$

Total differentiation of Eq.(7) gives,

$$dU = TdS + SdT + \sum_{\mathrm{i}} \tilde{\mu}_{\mathrm{i}} dn_{\mathrm{i}} + \sum_{\mathrm{i}} n_{\mathrm{i}} d\tilde{\mu}_{\mathrm{i}} - PdV - VdP, \tag{8}$$

and combining Eq.(6) and Eq.(8) leads to,

$$0 = SdT + \sum_{\mathrm{i}} n_{\mathrm{i}} d\tilde{\mu}_{\mathrm{i}} - VdP, \tag{9}$$

which is the standard form of the Gibbs-Duhem equation.

For systems containing interfaces, the principal challenge lies in defining the appropriate surface contributions to Eqs.(6) and (7). As originally formulated by Gibbs[93], the reversible work required to create

new surface area introduces an additional term, γA, where γ is the surface free energy and A is the surface area. Introducing this term yields the fundamental equation for the surface,

$$U^{\mathrm{s}} = TS^{\mathrm{s}} + \sum_{\mathrm{i}} \tilde{\mu}_{\mathrm{i}}\, {n_i}^{\mathrm{s}} - PV^{\mathrm{s}} + \gamma A, \tag{10}$$

where the superscript s represents the surface phase. It is important to note the physical meaning of γ across different interfaces. While γ represents the isotropic surface tension for fluid interfaces, its application to solid interfaces requires careful distinction. As demonstrated by Couchman et al.[94,95], solid surfaces can undergo elastic strain. Thus, γ in this formalism strictly represents the surface free energy (the work to create new surface), which is distinct from the mechanical surface stress involved in elastically stretching a sold. The strain is defined as,

$$\epsilon_{ij} = \frac{\delta_{ij} A_{el}}{A}, \tag{11}$$

where A_{el} is the elastically deformed area and δ_{ij} is the Kronecker symbol reflecting the surface strain is tensor. The change in energy associated with an elastic deformation is $g_{ij} d\left(\delta_{ij} A_{el}\right)$, with g_{ij} being the surface stress, while a plastic deformation is γdA_p. Therefore, Eq.(6) is transformed to,

$$dU^{\mathrm{s}} = TdS^{\mathrm{s}} - PdV^{\mathrm{s}} + \sum_{\mathrm{i}} \tilde{\mu}_{\mathrm{i}} d{n_i}^{\mathrm{s}} + \gamma dA_p + A g_{ij} d\epsilon_{ij}. \tag{12}$$

Combining with Eq.(12) and $dA = dA_p + dA_{el}$, differentiation of Eq.(10) lead to a general **surface Gibbs-Duhem equation**,

$$0 = S^{\mathrm{s}} dT + \sum_{\mathrm{i}} {n_i}^{\mathrm{s}} d\tilde{\mu}_{\mathrm{i}} - V^{\mathrm{s}} dP + Ad\gamma - A\left(g_{ij} - \gamma\delta_{ij}\right) d\epsilon_{ij}. \tag{13}$$

This form provides the thermodynamic foundation for deriving three key interfacial relations: the Gibbs adsorption equation, the Lippman equation, and the Shuttleworth equation. Under conditions of constant temperature and pressure, Eq.(13) reduces to the generalized **Gibbs adsorption equation**[96],

$$-d\gamma = \left(\sum_{\mathrm{i}} \Gamma_{\mathrm{i}} d\tilde{\mu}_{\mathrm{i}}\right)_{T,P} - \left(g_{ij} - \gamma\delta_{ij}\right) d\epsilon_{ij}, \tag{14}$$

where $\Gamma_{\mathrm{i}} = {n_i}^{\mathrm{s}}/A$ is the surface excess concentration of species i. For a liquid electrode, the surface strain is disappeared, namely, $d\epsilon_{ij} = 0$, and Eq.(14) can be written as,

$$-d\gamma = \left(\sum_{\mathrm{i}} \Gamma_{\mathrm{i}} d\tilde{\mu}_{\mathrm{i}}\right)_{T,P}. \tag{15}$$

2.2. Liquid-liquid interfaces

2.2.1. Surface tension and Lippmann equation

We first consider the interface between a liquid metal electrode and an electrolyte solution. The interface is in contact with two bulk phases (see Figure 3): the metal (subscript M) and the electrolyte solution (subscript S). For generality, partially charged chemisorbed species, denoted by subscript ad, are considered. The metal phase consists of metal atoms M, metal ions M^{z+}, and electrons e^{-}. These species are present in both the metal bulk and the interfacial region, but not in the liquid solution. Electrolyte cations and anions and solvent molecules are present in the solution bulk and interfacial region.

Under these conditions, the Gibbs adsorption equation (Eq.(15)) becomes,

$$-d\gamma = \sum_{\mathrm{i}}^{\mathrm{M}} \Gamma_{\mathrm{i}} d\tilde{\mu}_{\mathrm{i}} + \sum_{\mathrm{j}}^{\mathrm{ad}} \Gamma_{\mathrm{j}} d\tilde{\mu}_{\mathrm{j}} + \sum_{\mathrm{i}}^{\mathrm{S}} \Gamma_{\mathrm{i}} d\tilde{\mu}_{\mathrm{i}}. \tag{16}$$

At the interface, metal atoms, metal ions, and electrons are in equilibrium with their counterparts in the metal bulk. Their chemical potentials therefore equal the corresponding bulk values and satisfy $\mu_{\mathrm{M}} = \mu_{\mathrm{M}^{z+}} + z\mu_{\mathrm{e}}$. For a metallic electrode, the chemical potentials of metal atoms and electrons are fixed by the bulk phase, hence $d\mu_{\mathrm{e}} = d\mu_{\mathrm{M}} = 0$. Decomposing the electrochemical potential into chemical and the electrostatic parts, the metal contribution in Eq.(16) becomes,

$$\begin{aligned}
&\sum_{\mathrm{i}}^{\mathrm{M}} \Gamma_i d\tilde{\mu}_i = \Gamma_{\mathrm{M}^{z+}} d\tilde{\mu}_{\mathrm{M}^{z+}} + \Gamma_{\mathrm{e}} d\tilde{\mu}_{\mathrm{e}} + \Gamma_{\mathrm{M}} d\mu_{\mathrm{M}} \\
&= \Gamma_{\mathrm{M}^{z+}} d\mu_{\mathrm{M}^{z+}} + \Gamma_{\mathrm{e}} d\mu_{\mathrm{e}} + (ze_0\Gamma_{\mathrm{M}^{z+}} - e_0\Gamma_{\mathrm{e}}) d\phi_{\mathrm{M}} + \Gamma_{\mathrm{M}} d\mu_{\mathrm{M}} \\
&= \Gamma_{\mathrm{M}^{z+}} d(\mu_{\mathrm{M}} - z\mu_{\mathrm{e}}) + \Gamma_{\mathrm{e}} d\mu_{\mathrm{e}} + \Gamma_{\mathrm{M}} d\mu_{\mathrm{M}} + \sigma_{\mathrm{M}} d\phi_{\mathrm{M}} \\
&= \sigma_{\mathrm{M}} d\phi_{\mathrm{M}},
\end{aligned} \tag{17}$$

where $\sigma_{\mathrm{M}} = ze_0\Gamma_{\mathrm{M}^{z+}} - e_0\Gamma_{\mathrm{e}}$ is the metal surface charge density.

We take the chemisorption of a monovalent anion, A^-, as an example,

$$A^- + * \leftrightarrow A_{ad}^{-\varsigma} + (1-\varsigma)e^-, \tag{18}$$

where $*$ denotes the adsorption site, ς the fraction of the electron remaining on the chemisorbate, and $(1-\varsigma)$ the fraction of the electron transferred in the chemisorption reaction. Because the vacant site acts as a reactant, its chemical potential (μ_*) must be included in the equilibrium conditions, yielding, $\tilde{\mu}_{A^-} + \mu_* = \tilde{\mu}_{A_{ad}} + (1-\varsigma)\tilde{\mu}_e$. Assuming the total number of surface sites is conserved, the surface Gibbs-Duhem relation dictates that the chemical potential of occupied and vacant sites is coupled. Consequently, by defining the effective adsorbate chemical potential relative to the vacant site, the adsorbate contribution in Eq.(16) simplifies to,

$$\begin{aligned}\sum_j^{ad} \Gamma_j d\tilde{\mu}_j &= \Gamma_{ad} d\tilde{\mu}_{ad} = \Gamma_{ad} d(\tilde{\mu}_{A^-} - (1-\varsigma)\tilde{\mu}_e) \\ &= \Gamma_{ad} d\mu_{A^-} - e_0 \Gamma_{ad} d\phi_S + (1-\varsigma) e_0 \Gamma_{ad} d\phi_M.\end{aligned} \tag{19}$$

For species in the solution, it follows that

$$\sum_i^S \Gamma_i d\tilde{\mu}_i = \sum_i^S \Gamma_i d\mu_i + \sum_i^S z_i e_0 \Gamma_i \, d\phi_S. \tag{20}$$

Electroneutrality of the overall system requires,

$$\sigma_M - \varsigma e_0 \Gamma_{ad} = -\sum_i^S z_i e_0 \Gamma_i. \tag{21}$$

Substituting Eqs.(17), (19)-(20) into Eq.(16) and using Eq.(21) yields the **Lippmann equation**,

$$\begin{aligned}-d\gamma &= \sigma_M d\phi_M + \Gamma_{ad} d\mu_{A^-} - e_0 \Gamma_{ad} d\phi_S + (1-\varsigma) e_0 \Gamma_{ad} d\phi_M \\ &\quad + \sum_i^S \Gamma_i d\mu_i + \sum_i^S z_i e_0 \Gamma_i \, d\phi_S \\ &= [\sigma_M + (1-\varsigma) e_0 \Gamma_{ad}] d(\phi_M - \phi_S) + \Gamma_{ad} d\mu_{A^-} + \sum_i^S \Gamma_i d\mu_i\end{aligned} \tag{22}$$

$$= \sigma_{\mathrm{tot}} d\phi_{\mathrm{S}}^{\mathrm{M}} + \Gamma_{\mathrm{ad}} d\mu_{\mathrm{A}^-} + \sum_{\mathrm{i}}^{\mathrm{S}} \Gamma_{\mathrm{i}} d\mu_{\mathrm{i}},$$

where $\phi_{\mathrm{S}}^{\mathrm{M}} = \phi_{\mathrm{M}} - \phi_{\mathrm{S}}$ is the inner potential difference between metal bulk and solution bulk, and $\sigma_{\mathrm{tot}} = \sigma_{\mathrm{M}} + (1-\varsigma)e_0\Gamma_{\mathrm{ad}}$ is the total surface charge density.

When the solution composition is fixed, differentiating the surface tension with respect to $\phi_{\mathrm{S}}^{\mathrm{M}}$ gives,

$$\sigma_{\mathrm{tot}} = -\left(\frac{\partial \gamma}{\partial \phi_{\mathrm{S}}^{\mathrm{M}}}\right)_{T,P,\mu_{\mathrm{i}}} = -\left(\frac{\partial \gamma}{\partial E_{\mathrm{M}}}\right)_{T,P,\mu_{\mathrm{i}}}, \tag{23}$$

where E_{M} is the electrode potential, differing from $\phi_{\mathrm{S}}^{\mathrm{M}}$ only by a constant reference offset[40]. Eq.(23) shows that, in the presence of specific adsorption, the surface tension γ exhibits a maximum at the electrode potential where the total surface charge density vanishes. This potential is referred to as the **potential of zero total charge (PZTC)**.

Electrocapillary measurements by Grahame and co-workers[37,78] provide experimental validation of the electrocapillary curve, $\gamma(E_{\mathrm{M}})$. Figure 4(a) shows the effect of electrolyte composition on the surface tension of a mercury electrode. The cathodic branch of the electrocapillary profiles remains nearly unchanged, whereas pronounced differences are observed on the anodic side. This asymmetry reflects preferential specific adsorption of anions relative to cations. The corresponding total surface charge density curves are shown in Figure 4(b).

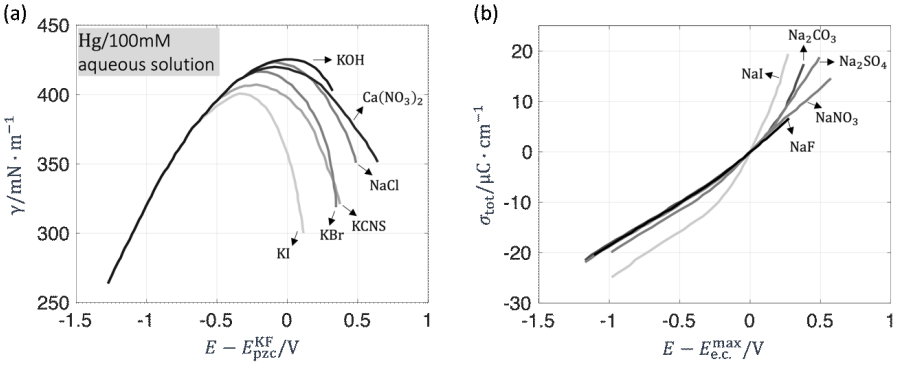

Figure 4. Electrolyte effect on the (a) surface tension and (b) total surface charge density of a mercury electrode as a function of the electrode potential for 100 mM aqueous solutions. Subplot (a) and (b) are reproduced with permission from Grahame[37,78].

In the absence of specifically adsorbed ions, Eq.(22) reduces to,

$$-d\gamma = \sigma_{\mathrm{M}} d\phi_{\mathrm{S}}^{\mathrm{M}} + \sum_{\mathrm{i}}^{\mathrm{S}} \Gamma_{\mathrm{i}} d\mu_{\mathrm{i}}, \tag{24}$$

where $\sigma_{\mathrm{M}} = \sigma_{\mathrm{tot}} = \sigma_{\mathrm{free}}$ with σ_{free} being the free surface charge density.

2.2.2. Various capacitances

The partially charged chemisorbed ions $A^{-\varsigma}$, complicates the definition and calculation of surface charge densities. Six different types of surface charge densities can be defined in this case[97], as depicted in Figure 5, including the total surface charge density (σ_{tot}), the free surface charge density (σ_{free}), the metal surface charge density (σ_{M}), the total and net charge density of chemisorbates ($\sigma_{\mathrm{ad,tot}}$, $\sigma_{\mathrm{ad,net}}$), and the charge density involved in the partial charge transfer process (σ_{pct}).

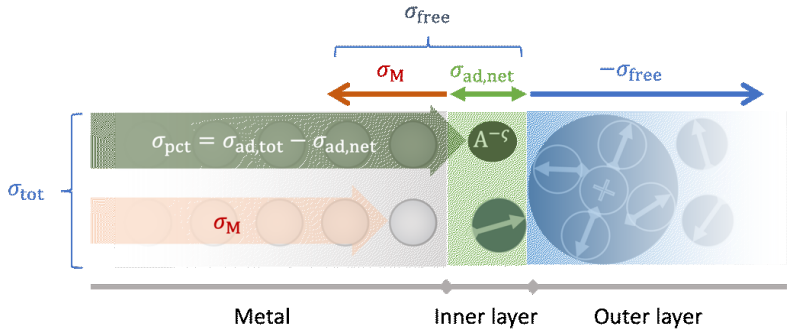

Figure 5. Surface charge densities of EDLs. The total charge density σ_{tot} measures the total amount of electrons flowing through the external circuit when the electrode is subject to a given potential. The metal charge density σ_{M} is a modelistic concept, describing the surface charge density within the metal region, of which the outer boundary is indefinite in the presence of chemisorbates. The total and net charge density of partially charged chemisorbates are $\sigma_{\mathrm{ad,tot}}$ and $\sigma_{\mathrm{ad,net}}$, respectively, and their difference is the amount of charge transferred between the metal and the chemisorbed ion, namely,

the charge involved in the partial charge transfer process, denoted σ_{pct}. The total charge density σ_{tot} is divided into σ_{pct} charging the chemisorbates and σ_{M} charging the metal. The amount of charge stored in the diffuse layer stretching from the OHP to the bulk solution is the negative of the free charge density σ_{free}. Since the overall EDL is electroneutral, σ_{free} is the sum of σ_{M} and $\sigma_{\mathrm{ad,net}}$, which establishes a rigid dichotomy between the metal and the chemisorbates. Reproduced from Ref.[97].

σ_{tot} is the total amount of electrons per unit area of the electrode flowing through the external circuit upon changing the electrode potential. At EDLs with chemisorption, σ_{tot} contains contributions from charging/discharging the EDL, chemisorbate adsorption/desorption, and the nontrivial coupling of these processes. The last aspect is illustrated using a thought experiment on chemisorption of a single anion at constant potential, as shown in Figure 6,

First, we freeze all other components of the EDL and move a monovalent anion from the bulk solution to the EDL. The moment the anion enters the EDL, an electron must flow out of the electrode to ensure overall electroneutrality of the EDL. Second, the anion comes closer to the electrode surface and experiences stronger electronic interactions with the metal, resulting in partial charge transfer between the anion and the metal. In this imaginary scenario, the partial charge transfer process only involves redistribution of electrons at the interface but no external flow of electrons. Third, the presence of this partially charged, chemisorbed anion induces an extra potential drop, changing the overall potential difference between the metal and the solution. To preserve the constant potential condition, a fraction of electron per anion flows back into the electrode, accompanied by an additional fraction of cation accumulates in the diffuse layer. Summing up the charge flow through the external circuit in the first and third step, the change in σ_{tot} is less than one electron upon chemisorption of a monovalent anion.

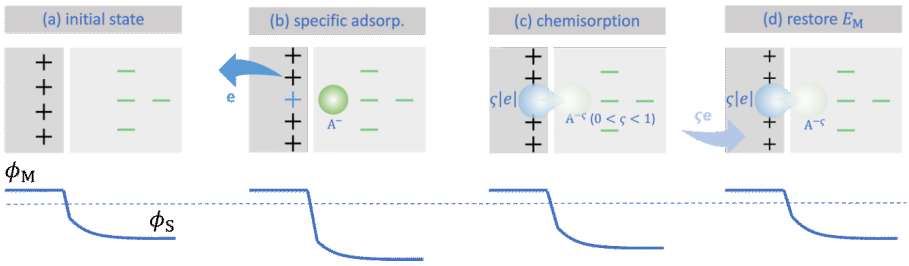

Figure 6. A thought experiment of an anion chemisorption. In step (a), the initial EDL has a positively charged metal and negatively charged diffuse layer, with the potential distribution sketched below. In

step (b), an anion comes into the inner layer of the EDL, accompanied by an electron flowing out of the electrode to ensure overall electroneutrality of the EDL and an enlarged potential difference at the interface. In step (c), partial charge transfer occurs between the metal and the anion, resulting in a partially charged anion and reducing the interfacial potential drop. In step (d), a fraction of electron per anion flows back into the electrode, accompanied by an additional fraction of cation accumulates in the diffuse layer. The initial potential difference between the metal and the solution is retained.

Generalizing this example, we consider chemisorption of multiple types of species including ions and solvent molecules with surface coverages $\theta_i = \frac{N_i}{N_{\mathrm{site}}}$ with N_{site} being the areal density of adsorption sites on the adsorbent, and N_i that of chemisorbates i. The charge of these species in the bulk solution is denoted q_i^{b}, which is nonzero for ions and zero for solvent. The total charge density of chemisorbates $\sigma_{\mathrm{ad,tot}}$, corresponding to the charge flow in the first step of the thought experiment, is,

$$\sigma_{\mathrm{ad,tot}} = \sum_i \theta_i N_{\mathrm{site}}\, q_i^{\mathrm{b}}, \tag{25}$$

accompanied by an equal amount of electron flow in the metal electrode.

Partial charges of these chemisorbed ions are denoted as q_i which are different from q_i^{b}. For instance, chemisorbed water molecules in the first layer above Pt(111) are reported to be positively charged. We denote the net charge density of chemisorbates $\sigma_{\mathrm{ad,net}}$,

$$\sigma_{\mathrm{ad,net}} = \sum_i \theta_i N_{\mathrm{site}}\, q_i. \tag{26}$$

The amount of charge transferred from chemisorbates to the electrode is,

$$\sigma_{\mathrm{pct}} = \sigma_{\mathrm{ad,tot}} - \sigma_{\mathrm{ad,net}}. \tag{27}$$

The ionic charge stored in the diffuse layer are free charge according to Frumkin,[16] because addition/removal of these ions involves no formation/cleavage of chemical bonds. Therefore, σ_{free}, in terms of the electrode charge therefore being negative of the ionic charge stored in the diffuse layer, reads,[17]

$$\sigma_{\mathrm{free}} = -\int_{z_{\mathrm{OHP}}}^{z_\infty} \left(\sum_i n_i \, q_i^{\mathrm{b}} \right) \mathrm{d}z, \tag{28}$$

where z_{OHP} denotes the OHP, z_∞ the bulk solution, and n_i the number density of ions.

Following the same reasoning in the thought experiment, the total surface charge density is,

$$\sigma_{\mathrm{tot}} = -\sigma_{\mathrm{ad,tot}} + \sigma_{\mathrm{free}}, \tag{29}$$

where $-\sigma_{\mathrm{ad,tot}}$ corresponds to charge flow through the external circuit in the first step, and σ_{free} that in the third step. The negative sign exists before $\sigma_{\mathrm{ad,tot}}$ because $\sigma_{\mathrm{ad,tot}}$ is defined for adsorbates and the corresponding charge on the electrode surface has the same magnitude but opposite signs. We note that σ_{free} and $\sigma_{\mathrm{ad,tot}}$ are coupled. As an immediate consequence of this coupling, chemisorption of a monovalent anion results in a fraction of an elementary charge flowing in the external circuit.

We can also define the amount of charge on the metal surface σ_{M}. In absence of chemisorption, we have $\sigma_{\mathrm{M}} = \sigma_{\mathrm{free}}$. However, this relation usually does not hold for the EDLs at transition metals due to the presence of partially charged chemisorbates with a net charge density of $\sigma_{\mathrm{ad,net}}$. Instead, we can calculate σ_{M} from the following requirement of electroneutrality,

$$\sigma_{\mathrm{M}} = \sigma_{\mathrm{free}} - \sigma_{\mathrm{ad,net}}, \tag{30}$$

which is not measurable.

Differentiating the Lippmann equation again, from Eq.(23), gives,

$$-\left(\frac{\partial^2 \gamma}{\partial {E_{\mathrm{M}}}^2}\right)_{T,P,\mu_{\mathrm{i}}} = \left(\frac{\partial \sigma}{\partial E}\right)_{T,P,\mu_{\mathrm{i}}}. \tag{31}$$

The charge density variants lead to corresponding differential capacitance variants defined as,

$$C(E) = \left(\frac{\partial \sigma}{\partial E}\right)_{\tilde{\mu}_i}, \tag{32}$$

where we have highlighted that the capacitance depends on the electrode potential E and that the electrochemical potentials $\tilde{\mu}_i$ are kept constant.

Therefore, we obtain the total differential capacitance,

$$C_{\mathrm{tot}}(E) = \left(\frac{\partial \sigma_{\mathrm{tot}}}{\partial E}\right)_{\tilde{\mu}_i}, \tag{33}$$

which, according to Eq. (29), is decomposed as,

$$C_{\mathrm{tot}}(E) = C_{\mathrm{ad}}(E) + C_{\mathrm{dl}}(E) \tag{34}$$

where the pseudo-capacitance of adsorption is,

$$C_{\mathrm{ad}}(E) = -\left(\frac{\partial \sigma_{\mathrm{ad,tot}}}{\partial E}\right)_{\tilde{\mu}_i}, \tag{35}$$

and the differential free double-layer capacitance is,

$$C_{\mathrm{dl}}(E) = \left(\frac{\partial \sigma_{\mathrm{free}}}{\partial E}\right)_{\tilde{\mu}_i}, \tag{36}$$

C_{ad} usually dominate over C_{dl} in the presence of chemisorbates as shown in Refs.[14, 18]. In addition, it is important to note that since the EDL structure is influenced by chemisorbates, C_{ad} and C_{dl} are not independent.

2.3. Solid-liquid interfaces

2.3.1. Revised thermodynamic framework

At solid-liquid interfaces, the surface tension depends on the surface strain, a generalized Gibbs adsorption Eq.(14) at constant temperature and pressure is given,

$$-d\gamma = \left(\sum_{\mathrm{i}} \Gamma_{\mathrm{i}} d\tilde{\mu}_{\mathrm{i}}\right)_{T,P} - \left(g_{ij} - \gamma \delta_{ij}\right) d\epsilon_{ij}, \tag{37}$$

Electrochemical potentials in Eq.(37) can be further decomposed into chemical and electrostatic components in the similar way for the liquid-liquid interfaces,

$$-d\gamma = \sigma_{\mathrm{tot}} dE_{\mathrm{M}} + \Gamma_{\mathrm{ad}} d\mu_{\mathrm{A}^-} + \sum_{\mathrm{i}}^{\mathrm{S}} \Gamma_{\mathrm{i}} d\mu_{\mathrm{i}} - \left(g_{ij} - \gamma \delta_{ij}\right) d\epsilon_{ij}. \tag{38}$$

2.3.2. Surface stress and its characteristic potential(s)

From Eq.(38), we obtain the relationship between surface tension and surface stress under constant potential conditions,

$$g_{ij} = \left(\gamma\delta_{ij} + \frac{\partial\gamma}{\partial\epsilon_{ij}}\right)_{T,P,\mu_{\mathrm{i}},E_{\mathrm{M}}}, \tag{39}$$

which is known as **the Shuttleworth equation**[52,41,43,12,46]. For liquid metal surfaces, the second term, $\frac{\partial\gamma}{\partial\epsilon_{ij}}$, vanishes, which means that surface stress equals to surface tension, $g = \gamma$. In contrast, for solid surfaces, elastic resistance to deformation renders the surface tension strain-dependent, leading to a fundamental distinction between surface tension and surface stress.

Conceptual analysis of surface stress

This distinction is particularly important for electrified solid-liquid interfaces, even in the absence of specific adsorption. According to the Lippmann equation, the surface tension follows an approximately parabolic dependence on electrode potential,

$$\gamma \approx \gamma_0 - \frac{1}{2}C_{\mathrm{dl}}(E - E_{\mathrm{pzc}})^2, \tag{40}$$

where, E_{pzc} is the potential of zero charge, C_{dl} is assumed to be a constant. The potential dependence of g is described by the Gokhshtein equation, which can be derived from Eq.(39), *c.f.*, Valincius[98],

$$\left(\frac{\partial g}{\partial E}\right)_{\epsilon} = -\sigma - \left(\frac{\partial\sigma}{\partial\epsilon}\right)_{T,P,\mu_{\mathrm{i}},E}, \tag{41}$$

at constant T, P and μ_{i}, where the second term on the right-hand side is given by,

$$\left(\frac{\partial\sigma}{\partial\epsilon}\right)_{T,P,\mu_{\mathrm{i}},E} = \left[\frac{\partial}{\partial\epsilon}\int_{E_{\mathrm{pzc}}}^{E} C_{\mathrm{dl}}\,d\phi\right]_{E} = -C_{\mathrm{dl}}\frac{\partial E_{\mathrm{pzc}}}{\partial\epsilon}. \tag{42}$$

Consequently, the potential dependence of the surface stress is approximated as,

$$\left(\frac{\partial g}{\partial E}\right)_{\epsilon} \approx -\sigma + C_{\mathrm{dl}}\frac{\partial E_{\mathrm{pzc}}}{\partial\epsilon}, \tag{43}$$

which makes explicit the two competing contributions that govern the potential dependence of surface stress: the capacitive charging of the metal surface and the strain dependence of the PZC. Eq.(43) parallels the modified electrocapillary relation given by Kramer[99], which indicates that deviations from classical Lippmann behavior arise from the additional strain-dependent term.

Several special cases of Eq.(43) are illustrated in Figure 7. If the strain dependence of the PZC is negligible, $C_{\mathrm{dl}} \frac{\partial E_{\mathrm{pzc}}}{\partial \epsilon} \approx 0$, we obtain $\left(\frac{\partial g}{\partial E}\right)_{\epsilon} \approx -\sigma$, meaning that $\left(\frac{\partial g}{\partial E}\right)_{\epsilon}$ decreases monotonically with electrode potential for σ increases monotonically with electrode potential. For this case, the surface stress exhibits a parabolic dependence on electrode potential, with an extremum close to E^{0}_{pzc}, consistent with the classical electrocapillary picture and with the scenario discussed by Kramer for weak elastic coupling[99]. In general, when the strain dependence of the PZC becomes so important that $\left|C_{\mathrm{dl}} \frac{\partial E_{\mathrm{pzc}}}{\partial \epsilon}\right| > |\sigma|$, $\left(\frac{\partial g}{\partial E}\right)_{\epsilon}$ shall remain positive or negative, depending on the sign of $\frac{\partial E_{\mathrm{pzc}}}{\partial \epsilon}$, over the relevant potential range. For this general case, the surface stress increases or decreases monotonically with electrode potential and crosses zero at a finite value of electrode potential.

Following the convention, a positive value of g indicates tensile surface stress (surface intends to contract), while a negative value indicates compressive surface stress (surface intends to expand) [54,43,46]. A characteristic electrode potential at which the surface stress itself vanishes, referred to the potential of zero surface stress (PZS), E_{pzs}, is observed in Figure 7(b). Previous studies, notably the estance measurements of Valincius et al.[100] and the theoretical analysis of Kramer[99], primarily focused on potentials at which the derivative of the surface stress with respect to potential vanishes, $\frac{\partial g}{\partial E} = 0$, corresponding to the extrema of electrocapillary or estance curves. Such "zero-estance" potentials characterize changes in the slope of $g(E)$ and may occur at multiple values depending on the electrolyte composition, adsorption, and elastic contributions, but they do not imply mechanical neutrality of the interface. By contrast, the PZS, which is, to the best of our knowledge, defined here for the first time, identifies the potential at which the $g(E)$ changes sign, marking the transition between compressive and tensile regimes. Interestingly, the PZS and the PZC are different. Within this framework, the relation between the PZS and the unstrained PZC can be approximated as,

$$E_{\mathrm{pzs}} \approx E^{0}_{\mathrm{pzc}} - \frac{\gamma^{0}_{\mathrm{max}}}{C_{\mathrm{dl}}} \left(\frac{\partial E_{\mathrm{pzc}}}{\partial \epsilon}\right)^{-1}, \tag{44}$$

where $\gamma_{\max}^{0}$ is the maximum surface tension at $\epsilon = 0$. Eq.(44) indicates that the PZS is distinct from the PZC, with the deviation determined by the strain dependence of the PZC. Eq.(44) can be used as an analytical framework to understand how metal charging and strain-induced shifts of the PZC jointly determine the emergence and location of the PZS.

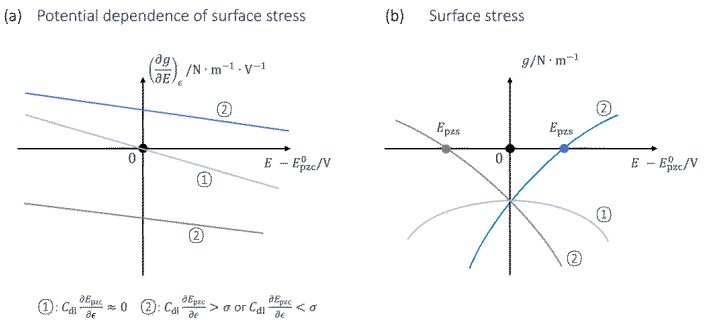

Figure 7. Conceptual analysis of (a) the potential dependence of the surface stress and (b) surface stress based on a simple model. When $C_{\mathrm{dl}}\frac{\partial E_{\mathrm{pzc}}}{\partial \epsilon} \approx 0$, which means that $\left(\frac{\partial g}{\partial E}\right)_\epsilon \approx -\sigma$ decreases monotonically with electrode potential with a zero value nearly the PZC. The surface stress profile shows a parabolic shape with a maximum value at nearly the PZC. When $\left|C_{\mathrm{dl}}\frac{\partial E_{\mathrm{pzc}}}{\partial \epsilon}\right| > |\sigma|$, which means that $\left(\frac{\partial g}{\partial E}\right)_\epsilon$ is positive or negative, depending on the sign of $\frac{\partial E_{\mathrm{pzc}}}{\partial \epsilon}$. The surface stress profile increases or decreases monotonically with the electrode potential and the surface stress has zero value. The relation between PZS and PZC, can be expressed as, $E_{\mathrm{pzs}} \approx E_{\mathrm{pzc}}^{0} - \frac{\gamma_{\max}^{0}}{C_{\mathrm{dl}}}\left(\frac{\partial E_{\mathrm{pzc}}}{\partial \epsilon}\right)^{-1}$.

When there is specific adsorption of ions, Eq.(41) should be written as,

$$\left(\frac{\partial g}{\partial E}\right)_\epsilon = -\sigma_{\mathrm{tot}} - \left(\frac{\partial \sigma_{\mathrm{tot}}}{\partial \epsilon}\right)_{T,P,\mu_{\mathrm{i}},E}, \tag{45}$$

at constant T, P and μ_{i}, where the second term on the right-hand side is given by,

$$\left(\frac{\partial \sigma_{\mathrm{tot}}}{\partial \epsilon}\right)_{T,P,\mu_{\mathrm{i}},E} = \left[\frac{\partial}{\partial \epsilon}\int_{E_{\mathrm{pztc}}}^{E} C_{\mathrm{tot}} d\phi\right]_E. \tag{46}$$

Consequently, the potential dependence of the surface stress is written as,

$$\left(\frac{\partial g}{\partial E}\right)_{\epsilon} = -\sigma_{\mathrm{tot}} - \left[\frac{\partial}{\partial \epsilon}\int_{E_{\mathrm{pztc}}}^{E} C_{\mathrm{tot}} d\phi\right]_{E}, \tag{47}$$

where σ_{tot} and C_{tot} denote the total surface charge density and the total differential capacitance, respectively, as descripted in the **section 2.2.2**. Both quantities are influenced by the specific adsorption of ions. Therefore, the potential dependence of the surface stress is intrinsically coupled to ion-specific adsorption.

Chapter 3. Theoretical models

*Reproduced with minor changes from '**Zhang Z**, Huang J*, Microstructure of Electrical Double Layers at Highly Charged States[J]. JACS Au, 2025, 5 (7), 3453-3467'.*

3.1. Introduction

This chapter presents the theoretical frameworks employed in this thesis to describe the structure and thermodynamic properties of EDL at metal-electrolyte interfaces. The chapter pursues two main goals. First, the classical GCS model is introduced as the conventional baseline framework for EDL theory. Its underlying assumptions, governing equations, and extensions accounting for finite ion size effects are discussed in detail. Second, the predictive capabilities and intrinsic limitations of the GCS model are critically assessed through direct comparison with experimental C_{dl} data. This analysis highlights the regimes in which classical continuum models provide a reasonable description of interfacial electrostatics, as well as the conditions under which they fail to capture key experimental trends. By systematically examining these limitations, this chapter provides the motivation for adopting more advanced theoretical approaches that explicitly account for electronic structure effects and electrolyte thermodynamics. In particular, it establishes the conceptual and methodological basis for the semiclassical DPFT framework introduced later in the chapter and employed extensively in the subsequent chapters of this thesis.

3.2. Gouy-Chapman-Stern (GCS) model

3.2.1. Model formulation

Within the classical GCS model, the differential double-layer capacitance can be considered as a series connection between the Helmholtz layer capacitance and the diffuse layer capacitance,

$$\frac{1}{C_{\mathrm{dl}}} = \frac{1}{C_{\mathrm{GC}}} + \frac{1}{C_{\mathrm{H}}}, \tag{48}$$

where the diffuse layer capacitance, C_{GC}, can be obtained from solving the modified Poisson-Boltzmann equation considering the ion size effect[23,101]. The PB equation describes the distributions of the electric potential and the ion concentrations in the electrolyte solution. Poisson equation reads,

$$\nabla \cdot \left(\epsilon_{\mathrm{s}}^{\mathrm{b}} \nabla \phi\right) = -\sum_{i} z_i F c_i, \tag{49}$$

where $\epsilon_{\mathrm{s}}^{\mathrm{b}}$ is the bulk dielectric permittivity of the electrolyte solution, ϕ the electric potential, z_i the charge number of ion i, F the Faraday's constant, c_i the concentration of ion i. Boltzmann equation further connects c_i and ϕ,

$$c_i = c_i^{\mathrm{b}} \exp\left(-\frac{z_i F}{RT}\phi\right), \tag{50}$$

where R is the gas constant, T the temperature. For a binary monovalent electrolyte solution in a one-dimensional space, the PB equation is rewritten as,

$$\nabla \cdot \left(\epsilon_{\mathrm{s}}^{\mathrm{b}} \nabla \phi\right) = -F c_i^{\mathrm{b}} \left[\exp\left(-\frac{F\phi}{RT}\right) - \exp\left(\frac{F\phi}{RT}\right)\right], \tag{51}$$

where c^{b} is the concentration of total anions (cations) in the solution bulk. The dimensionless form of the PB equation is shown as,

$$\frac{\partial^2 U}{\partial X^2} = \sinh(U), \tag{52}$$

with the dimensionless quantities, $U = F\phi/RT$, $X = x/\lambda_{\mathrm{D}}$, and the Debye length $\lambda_{\mathrm{D}} = \sqrt{\frac{RT\epsilon_{\mathrm{s}}^{\mathrm{b}}\epsilon_0}{2F^2 c_i^{\mathrm{b}}}}$.

The boundary conditions to close Eq.(52), a second-order differential equation, are,

$$U(X = 0) = U_{\mathrm{HP}}, \tag{53}$$

$$U(X = \infty) = 0, \tag{54}$$

where $X = 0$ represents the left boundary, at the HP, and $X = \infty$ is the right boundary, in the solution bulk. U_{HP} can be calculated from the electrode side,

$$\phi_{\mathrm{HP}} = E_{\mathrm{M}} - E_{\mathrm{pzc}} + \left(\frac{\partial \phi}{\partial x}\right)_{x=0^+} \frac{\epsilon_{\mathrm{s}}^{\mathrm{b}}}{\epsilon_{\mathrm{HP}}} \delta_{\mathrm{HP}}, \tag{55}$$

where ϵ_{HP} and δ_{HP} are the dielectric permittivity and the thickness of the space between the electrode and the HP, respectively. The coefficient $\epsilon_{\mathrm{s}}^{\mathrm{b}}/\epsilon_{\mathrm{HP}}$ is resulted from the following equality in terms of surface free charge density on the electrode surface,

$$\sigma_{\mathrm{free}} = -\epsilon_{\mathrm{s}}^{\mathrm{b}}\left(\frac{\partial\phi}{\partial x}\right)_{x=0^{+}} = -\epsilon_{\mathrm{HP}}\left(\frac{\partial\phi}{\partial x}\right)_{x=0^{-}}. \tag{56}$$

Solving Eq. (52) in the following steps,

$$2\frac{\partial^2 U}{\partial X^2}\frac{\partial U}{\partial X} = 2\sinh(U)\frac{\partial U}{\partial X}, \tag{57}$$

$$\mathrm{d}\left(\frac{\partial U}{\partial X}\right)^2 = \mathrm{d}(2\cosh U), \tag{58}$$

$$\left(\frac{\partial U}{\partial X}\right)_{X=0^{+}}^{2} = \left(2\sinh\left(\frac{U_{\mathrm{HP}}}{2}\right)\right)^2, \tag{59}$$

we obtain the relationship between the excess free surface charge density and the electric potential at the HP,

$$\sigma_{\mathrm{free}} = -\int (c_{+} - c_{-})F\mathrm{d}x = -\epsilon_{\mathrm{s}}^{\mathrm{b}}\left(\frac{\partial\phi}{\partial x}\right)_{x=0^{+}} = \frac{2\epsilon_{\mathrm{S}}RT}{F\lambda_{\mathrm{D}}}\sinh\left(\frac{F\phi_{\mathrm{HP}}}{2RT}\right). \tag{60}$$

While the classical PB formulation captures the essential electrostatic screening behavior in dilute solutions, it neglects the finite size of ions and solvent molecules. At higher electrolyte concentrations or under strong interfacial electric fields, this approximation breaks down due to ion crowding near the electrode surface. To address this limitation, steric effects can be incorporated by adopting a lattice-gas description of the electrolyte, leading to the Bikerman–Poisson–Boltzmann (BPB) model[102–104]. In the BPB model, each ion occupies a volume of ${a_{\mathrm{t}}}^3$, where a_{t} is the lattice size. The maximum particle number density is $n_{\mathrm{t}} = {a_{\mathrm{t}}}^{-3}$. The electrochemical potential for ion i reads,

$$\tilde{\mu}_i = \mu_i^0 + z_i e_0\phi + k_{\mathrm{B}}T\ln\frac{{a_{\mathrm{t}}}^3 n_i}{1 - {a_{\mathrm{t}}}^3\sum_i \gamma_i n_i}, \tag{61}$$

where μ_i^0 is the chemical potential under standard conditions, e_0 the elementary charge, k_B the Boltzmann constant, n_i the number density of ion i, $\gamma_\mathrm{i} = \left(\frac{2r_\mathrm{i}}{R_\mathrm{s}}\right)^3$ is the relative size of ions referenced to solvent with r_i being the radius of solvated ion and R_s the diameter of solvent. $(1 - {a_\mathrm{t}}^3 \sum_i \gamma_i n_i)/{a_\mathrm{t}}^3$ is the number density of solvent molecules. For a binary monovalent electrolyte solution, we have $n_-^0 = n_+^0 = n_0^\mathrm{b}$, with n_0^b the number density of total anions (cations) in the solution bulk. Under equilibrium conditions, the electrochemical potential for ion i is uniform in the whole EDL,

$$\tilde{\mu}_i = \mu_i^0 + z_i e_0 \phi + k_\mathrm{B} T \ln \frac{{a_\mathrm{t}}^3 n_i}{1 - {a_\mathrm{t}}^3 \sum_i \gamma_i n_i} = \mu_i^0 + k_\mathrm{B} T \ln \frac{{a_\mathrm{t}}^3 n_0^\mathrm{b}}{1 - {a_\mathrm{t}}^3 \sum_i \gamma_i n_0^\mathrm{b}}. \tag{62}$$

The number density of ion i is obtained as,

$$n_i = \frac{n_0^\mathrm{b} \exp\left(\frac{\mp e_0 \phi}{k_\mathrm{B} T}\right)}{1 + \frac{v}{2}\left(\gamma_+ \exp\left(\frac{-e_0 \phi}{k_\mathrm{B} T}\right) + \gamma_- \exp\left(\frac{e_0 \phi}{k_\mathrm{B} T}\right) - \gamma_+ - \gamma_-\right)}, \tag{63}$$

where the bulk volume fraction of solvated ions is $v = 2{a_\mathrm{t}}^3 n_0^\mathrm{b}$. The GCS model assumes $v = 0$.

Combining Eq. (49) and Eq. (63), the BPB model is described as,

$$\nabla \cdot \left(\epsilon_\mathrm{s}^\mathrm{b} \nabla \phi\right) = \frac{2 n_0^\mathrm{b} e_0 \sinh\left(\frac{\mp e_0 \phi}{k_\mathrm{B} T}\right)}{1 + \frac{v}{2}\left(\gamma_+ \exp\left(\frac{-e_0 \phi}{k_\mathrm{B} T}\right) + \gamma_- \exp\left(\frac{e_0 \phi}{k_\mathrm{B} T}\right) - \gamma_+ - \gamma_-\right)}. \tag{64}$$

The dimensionless form is,

$$\frac{\partial^2 U}{\partial X^2} = \frac{\sinh U}{1 + \frac{v}{2}\left(\gamma_\mathrm{c} e^{-U} + \gamma_\mathrm{a} e^{U} - \gamma_\mathrm{c} - \gamma_\mathrm{a}\right)}. \tag{65}$$

The diffuse layer capacitance, C_GC, can be obtained from solving the modified PB equation considering the ion size effect,

$$C_\mathrm{GC} = \frac{\partial \sigma_\mathrm{free}}{\partial U_\mathrm{HP}} = -\frac{\partial}{\partial U_\mathrm{HP}}\left(\frac{\partial U}{\partial X}\right)_{X = \mathrm{HP}^+}. \tag{66}$$

However, the total C_dl also depends critically on the compact region between the electrode surface and the Helmholtz plane, C_H in the Eq.(48) is the Helmholtz layer capacitance. As a historical note,

Grahame[37,105] determined the C_{H} versus electrode potential curve from the measured C_{dl} curve at ~ 1 M NaF after correcting for the diffuse layer capacitance described by the Gouy-Chapman theory. He then used the obtained C_{H} in Eq.(48) to analyze the C_{dl} curves for other concentrations. Therefore, Grahame himself did not model the C_{H} curve. For this reason, Kornyshev, Spohr, and Vorotyntsev described the Grahame approach as semi-empirical[38], named GCS_se. Different from this semiempirical approach, a primitive approach involves calculating C_{H} from $\frac{\epsilon_{\mathrm{H}}\epsilon_0}{\delta_{\mathrm{H}}}$ with ϵ_{H} and ϵ_0 being the dielectric permittivity of the space between the HP and the metal surface and vacuum, respectively, and δ_{H} the distance between the HP and the metal surface. This model is referred to as GCS_pm. We implement both approaches and a comparison in terms of C_{dl} between the GCS models and experiments in Hg-100mM NaF aqueous solution[105], as shown in Figure 8.

3.2.2. Comparison between experiment and the GCS models

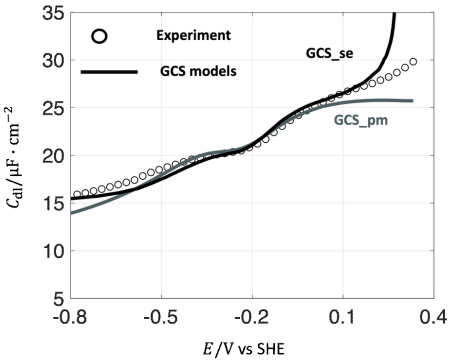

Figure 8. Comparison of C_{dl} between experiment (circle) and the GCS models (solid line) in Hg-100mM NaF aqueous solution. The GCS_se is compared with the primitive GCS model (GCS_pm). Fitted parameters are $\varepsilon_{\mathrm{H}} = 6$, $\delta_{\mathrm{H}} = 0.91$ Å, $r_- = 3$ Å, $r_+ = 7.5$ Å. Experimental data were reported by Grahame et al[105]. The electrode potential is at the SHE scale.

The fitting process of the GCS models are shown in Figure 9 and Figure 10. Additionally, we performed a sensitivity analysis of the GCS model. The resulting analysis, presented in Figure 9(e), shows that while the capacitance curve is slightly adjusted, the impact on the fitted parameters remains minimal across the studied concentration range. The GCS model results are calculated using the following model parameters: $\epsilon_{\mathrm{H}} = 6$, $\delta_{\mathrm{H}} = 0.91$ Å, $r_- = 3$ Å, $r_+ = 7.5$ Å. The fitted value of permittivity ϵ_{H} is within the usual value

between the 3 and 6 for the description of HP.[106] The fitted δ_{H} is an effective value reflecting the closest distance that ions can approach the electrode surface. The solvated ion radius $r_{\pm}$ takes into account the ion-solvation interactions. Notably, the fitted radius of solvated Na^{+} is larger than the value of 3 Å estimated by AIMD simulations[107] for Na^{+} with one layer of water. This suggests that the GCS model effectively considers more-than-one water layers in the solvation shell of Na^{+}.

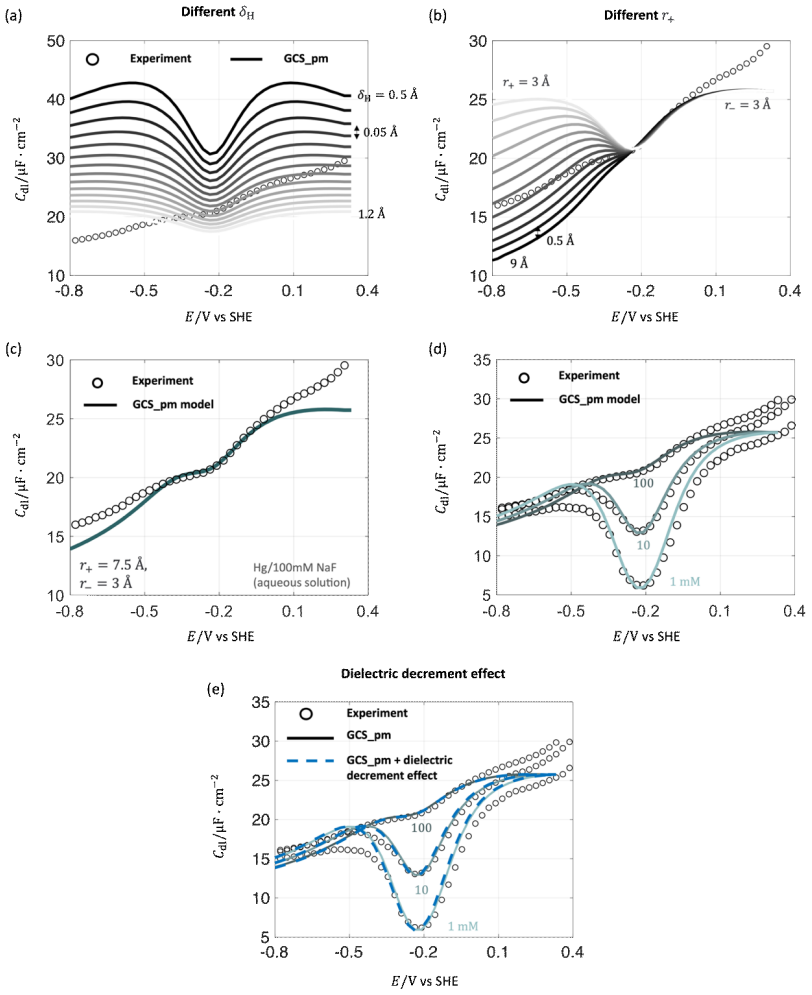

Figure 9. The GCS_pm model[23,101]. (a, b) the GCS_pm model with different δ_H and r_+, respectively. Comparison of C_{dl} between the GCS_pm model and experimental results at (c) 100mM concentration (d) varying ion concentration. (e) Comparison between the GCS_pm model, with and without accounting the dielectric decrement effect, and experimental results at varying ion concentrations. The permittivity values for 1mM, 10mM and 100mM are 78.48, 78.35 and 77.07, respectively, estimated using the empirical equation (16) in ref.[108]. Experimental data were reported by Grahame et al[105]. Fitted parameters are $\varepsilon_H = 6$, $\delta_H = 0.91$ Å, $r_- = 3$ Å, $r_+ = 7.5$ Å. The electric potential is on the SHE scale.

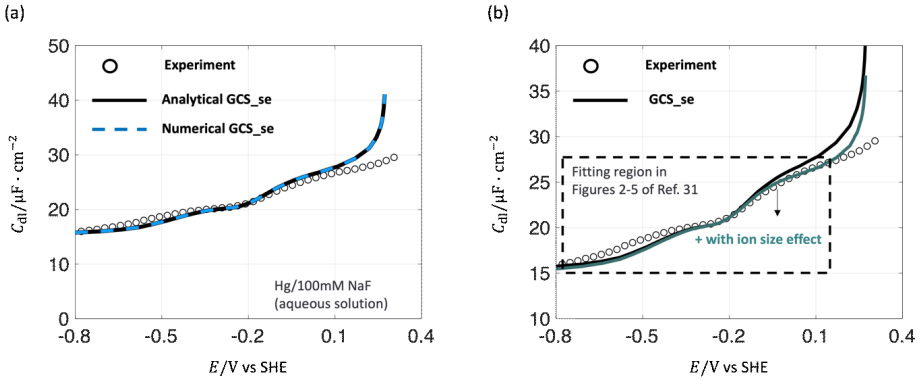

Figure 10. Comparison of C_{dl} between the GCS_se model and experimental results in Hg-100mM NaF aqueous solution. (a) Numerical (dashed line) and analytical GCS_se (solid line) model, (b)The numerical GCS_se model considering the ion size effect. Experimental data were reported by Grahame et al[105]. The electric potential is on the SHE scale.

In general, GCS_se and GCS_pm models can well reproduce the C_{dl} curves of the Hg-NaF aqueous interface near $E_{pzc} = -0.22$ V vs SHE. The discrepancy between the GCS_pm model and the experimental data is observed at more positive potentials $E > 0.1\ V_{SHE}$, and more negative potentials $E < -0.3\ V_{SHE}$. The GCS_se model improves over GCS_pm in matching experimental data, but still overpredicts capacitance values at potentials beyond 0.2 V from the PZC. The divergence at more positive potentials is explained in the literature usually as the consequence of specifically adsorbed anions[39,106,109–114]. For example, in the study of Wang et. al.,[39] a modified GCS model considering anion specific adsorption can neatly capture the whole C_{dl} profile in Ag(111)-NaF aqueous solution[39]. Since the specific adsorption

of F^- in the given potential range is rather weak and thus unlikely responsible for the observed divergence[37], we argue that there could be other causes.

3.2.3. Assessment of limitations of GCS models

Afterwards, we systematically compare the C_{dl} curves between experiments and the GCS_pm model for different cations, anions and solvent molecules[105,112,115,116], as shown in Figure 11. We exhibit the comparison at a high concentration, 100mM, because the C_{dl} curves in more dilute solutions can be readily grasped once the more concentrated case is well understood. The solid points in Figure 11 represent the PZC, corresponding to the Gouy-Chapman minimum in dilute solutions. In Figure 11(a), the experimental C_{dl} profiles in the cathodic region are nearly identical for Na^+ and K^+ which have different solvation ion sizes. However, the GCS_pm model results in Figure 11(b) show significant differences. In the GCS_pm model, the cathodic peak of C_{dl} is smaller for Na^+ than K^+, as Na^+ has a larger hydrated radius[117]. In the anodic region, the two pieces of results calculated by the GCS_pm model are identical since the same anion, F^-, is considered. We note that experimental results are taken from two separate studies[105,115], so we cannot exclude the possibility that the differences between the two experiments are just experimental errors, though the magnitude of differences exceeds the experimental error estimated by Grahame[118].

The anion effects are examined in Figure 11(c). The experimental C_{dl} profiles in the cathodic region are nearly the same, as expected, since the same cation, K^+, is used in both measurements. Consistent with the GCS_pm model, experimental data exhibit a smaller anodic C_{dl} peak for PF_6^- than for F^-, as PF_6^- has a larger hydrated radius. However, the GCS models cannot account for the difference in the PZC. PF_6^- has a more negative PZC compared to F^-[112]. Moreover, the rising trend at more anodic potentials for F^- is not captured by the GCS_pm model.

In Figure 11(e), we examine the effects of solvent molecules on the experimental C_{dl} profiles. Experiments show that the PZC is more positive in DMSO than H_2O, which cannot be explained by the GCS_pm model. Moreover, it is interesting to note that the C_{dl} profiles intersect at around $0.05\ \mathrm{V\ vs\ SHE}$. At potentials negative of $0.05\ \mathrm{V\ vs\ SHE}$, the experimental C_{dl} is smaller for DMSO than H_2O, while the opposite trend is observed at potentials positive of $0.05\ \mathrm{V\ vs\ SHE}$. On the contrary, the GCS_pm model gives a C_{dl} profile constantly smaller for DMSO than H_2O. The reasons for the magnitude difference are, at least, twofold. On the one hand, DMSO has a lower permittivity ($\epsilon_s^b = 46.8$) compared to H_2O ($\epsilon_s^b = 78.5$). On the other hand, both K^+ and PF_6^- ions have larger solvated radius in DMSO than H_2O, as shown in Figure 11(f).

In a word, the GCS_se and GCS_pm model efficaciously describes the C_{dl} in the potential region near the PZC. However, it is deficient to describe the C_{dl} profile far away from the PZC. The deficiency is more apparent when the electrolyte effects on the PZC and the C_{dl} are considered. Therefore, there is a clear need for an improved model for mercury's EDL. As mentioned in the introduction, the DPFT will be employed as the model framework to analyze all above C_{dl} curves. Our proposed DPFT framework can be seen as an improved description of the complex behavior of C_{H} within a more detailed and physically motivated structure. It also goes beyond the GCS framework by incorporating a microscopic treatment of free and bound solvent molecules, potential-dependent metal-solvent short-range interactions, and partial desolvation of ions. In the next section, we will introduce three improvements to the DPFT model compared to our previous works[74,77,88].

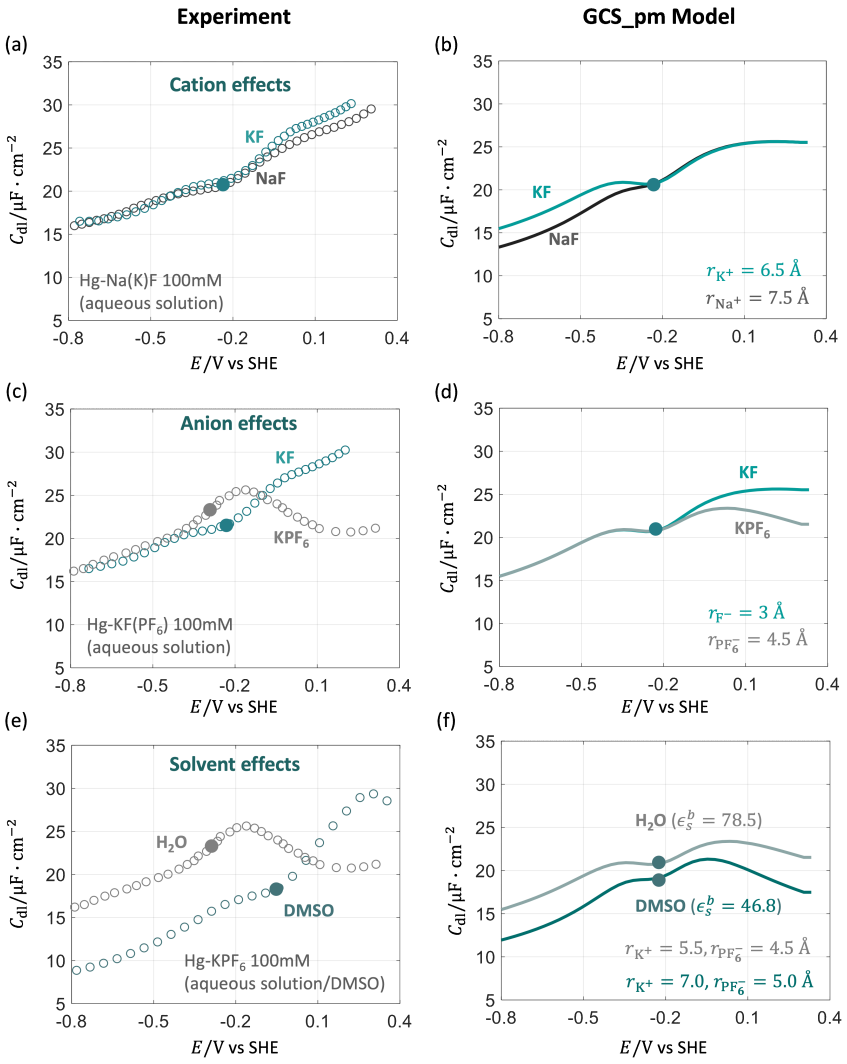
Experiment
GCS_pm Model
(a)
Cation effects
KF
NaF
Hg-Na(K)F 100mM
(aqueous solution)
(b)
KF
NaF
$r_{K^+} = 6.5$ Å
$r_{Na^+} = 7.5$ Å
(c)
Anion effects
KF
KPF_6
Hg-KF(PF_6) 100mM
(aqueous solution)
(d)
KF
KPF_6
$r_{F^-} = 3$ Å
$r_{PF_6^-} = 4.5$ Å
(e)
Solvent effects
H_2O
DMSO
Hg-KPF_6 100mM
(aqueous solution/DMSO)
(f)
H_2O ($\epsilon_s^b = 78.5$)
DMSO ($\epsilon_s^b = 46.8$)
$r_{K^+} = 5.5, r_{PF_6^-} = 4.5$ Å
$r_{K^+} = 7.0, r_{PF_6^-} = 5.0$ Å
$C_{dl}/\mu F \cdot cm^{-2}$
E/V vs SHE

Figure 11. Comparison of C_{dl} between experimental results[105,112,115,116] (a, c, e) and the GCS_pm model (b, d, f) for the EDL at the Hg-electrolyte solution interface with a concentration of 100 mM. (a, b) Effects of cations, Na^{+} and K^{+}, on C_{dl}, (c, d) Effects of anions, PF_6^{-} and F^{-}, on C_{dl}, and (e, f) Effects of solvent molecules, water and DMSO, on C_{dl}. Other parameters used in the GCS model are provided in the **Table 1** and **Table 2**. The solid points denote the potentials of zero charge.

3.3. Density-potential functional theoretical models

The framework and new modifications of the DPFT are introduced in this section. We realize that our previous DPFT model, denoted DPFT_pre, is deficient in describing the interfacial permittivity as it may go unrealistically higher than the permittivity of bulk water, see Figure 3 (h) in ref[74]. Herein, we refine the description of interfacial permittivity, following Dreyer et al.[119], by distinguishing free solvent molecules from those trapped in the solvation shell of ions, and further accounting for the dielectric screening capabilities of the trapped solvent molecules. This updated DPFT model is denoted DPFT. As to be rationalized in the subsequent analysis of experimental data, the DPFT model is further modified by introducing the potential dependence of short-range metal-solvent interactions, denoted the DPFT_sol model, and the partial desolvation of ions at highly charged surfaces, denoted the DPFT_desol model. A summary of features of the three DPFT models is given in Figure 12.

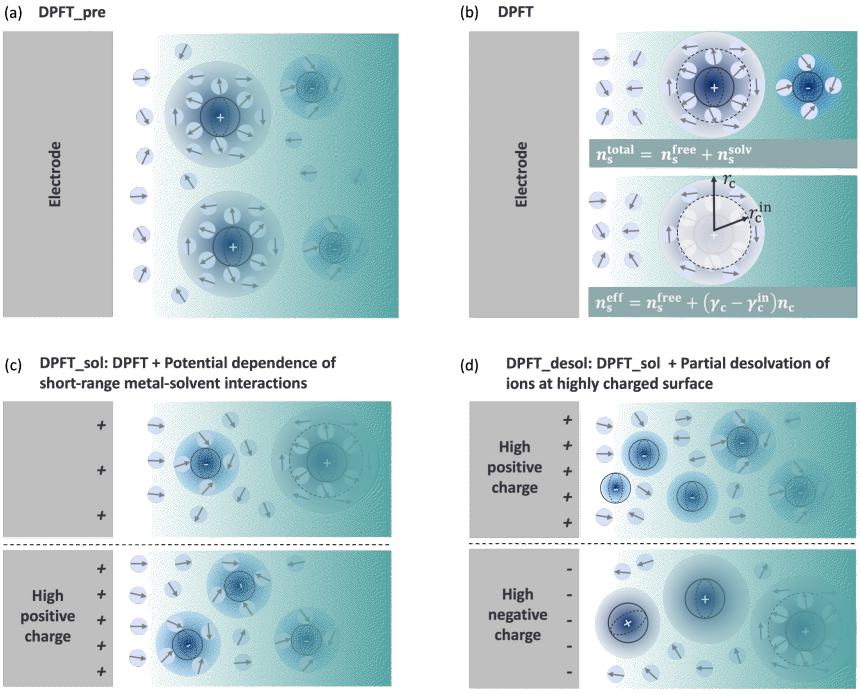

Figure 12. Schematic diagram of four versions of the DPFT. (a) DPFT_pre: the previous DPFT model[74]. (b) DPFT: the solvent molecules are divided into free ones with a number density of n_s^{free} and trapped ones with a number density of n_s^{solv}. (c) DPFT_sol: DPFT + the potential dependence of short-range metal-solvent interactions. (d) DPFT_desol: DPFT_sol + the partial desolvation of ions at highly charged surfaces.

In the DPFT, the volumetric density of the grand potential of the EDL is given by[74,75],

$$g = f_{qm}[n_e, \nabla n_e] + f_c[\phi, \nabla\phi, \{n_i\}] + f_{int}[\phi, \nabla\phi, \{n_i\}] - \left[n_e\tilde{\mu}_e + \sum_{i=a,c,s} n_i\tilde{\mu}_i\right], \quad (67)$$

where f_{qm}, f_c and f_{int} represent the three contributions to the Helmholtz free energy, namely, the quantum part for the electron gas, the classical part for the electrolyte solution, and the short-range interactions between the electron gas and the electrolyte solution, respectively. The last term ensures modelling the EDL as an open system in contact with both an electron reservoir and an electrolyte solution

reservoir. $\tilde{\mu}_{\mathrm{e}}$ and $\tilde{\mu}_{\mathrm{i}}(\mathrm{i}=\mathrm{c},\mathrm{a},\mathrm{s})$ represent the electrochemical potentials of electrons and solution species, respectively. f_{qm} consists of kinetic energy of non-interacting electrons (t_{ni}), exchange (u_{X}) and correlation (u_{C}) energies, and pseudopotential energy (p_{cc}), written as,

$$\begin{aligned} f_{\mathrm{qm}} &= t_{\mathrm{ni}}[n_e,\nabla n_e,\dots]+u_{\mathrm{X}}[n_e,\nabla n_e,\dots]+u_{\mathrm{C}}[n_e,\nabla n_e,\dots]+p_{\mathrm{cc}}[n_e] \\ &= e_{\mathrm{au}}a_0^{-3}\left[t_{\mathrm{TF}}(F_s(s)+\theta_{\mathrm{T}}s^2)+u_{\mathrm{X}}^0(1+\theta_{\mathrm{X}}s^2)+\left(u_{\mathrm{C}}^0+\theta_{\mathrm{C}}n_{\mathrm{e}}a_0^3t^2\right)+v_{\mathrm{cc}}n_{\mathrm{e}}\right], \end{aligned} \tag{68}$$

where $e_{\mathrm{au}}=e_0^2/(4\pi\epsilon_0 a_0)$ is the atomic energy with a_0 being the Bohr radius, e_0 the unit of electron charge, and ϵ_0 the vacuum permittivity. The kinetic energy of electrons is described by the semilocal approximation functionals[120–122]. $t_{\mathrm{TF}}=\frac{3}{10}(3\pi^2)^{\frac{2}{3}}(n_{\mathrm{e}}a_0^3)^{\frac{5}{3}}$ is the Thomas-Fermi volumetric kinetic energy density, and $(F_s(s)+\theta_{\mathrm{T}}s^2)$ is the correction for the inhomogeneity[120–122]. $F_s(s)$ is the so-called Pauli enhancement factor, $s=|\nabla n_{\mathrm{e}}|/\left(2(3\pi^2)^{\frac{1}{3}}(n_{\mathrm{e}})^{\frac{4}{3}}\right)$ is the reduced gradient term and θ_{T} is a gradient coefficient tuning the contribution of the gradient term. Here we take $\theta_{\mathrm{T}}=\frac{5}{3}$, a value commonly used in describing the metal[120–122]. For the approximation, some functionals are widely used for modeling transition metals, e.g. Thomas-Fermi-von Weiszäcker (TFvW), Pauli-Gaussian (PG) and Luo, Karasiev and Trickey (LKT) functionals[122]. These modify the enhancement term in Eq.(68), replaced $F_s(s)$ with 1 for the TFvW, with $e^{-\mu s^2}$ for the PG, and with $\mathrm{sech}(as)$ for the LKT. The newly added parameters are, $\mu=1$ for PG, $a=1.3$ for LKT[122]. The exchange-correlation energy is described by the PBE functional with the exchange energy of a uniform electron gas, $u_{\mathrm{X}}^0=-\frac{3}{4}\left(\frac{3}{\pi}\right)^{\frac{1}{3}}(n_{\mathrm{e}}a_0^3)^{\frac{4}{3}}$, $\theta_{\mathrm{X}}=0.1235$ is the variable tuning the contribution of the gradient term in the exchange energy. Similarly, u_{C}^0 is the correlation energy of a uniform electron gas, for which we use the interpolation relation of Perdew et al.,[120]

$$\begin{aligned} u_{\mathrm{C}}^0 &= -2\alpha_1 n_{\mathrm{e}}a_0^3(1+\alpha_2 r_s)\ln\left(1+\frac{1}{\xi}\right), \\ r_s &= \left(\frac{3}{4\pi n_{\mathrm{e}}a_0^3}\right)^{\frac{1}{3}}, \\ \xi &= 2\alpha_1\left(\alpha_3 r_s^{\frac{1}{2}}+\alpha_4 r_s+\alpha_5 r_s^{\frac{3}{2}}+\alpha_6 r_s^2\right), \end{aligned} \tag{69}$$

where $\alpha_1 = 0.0310907, \alpha_2 = 0.21370, \alpha_3 = 7.5957, \alpha_4 = 3.5876, \alpha_5 = 1.6382, \alpha_6 = 0.49294$. $\theta_C = 0.0667$ is a gradient coefficient in the correlation energy and $t = a_0^4|\nabla n_e|/\left(4\left(\frac{3}{\pi}\right)^{\frac{1}{6}}(n_e a_0^3)^{\frac{7}{6}}\right)$ is another reduced density gradient in terms of dimensional n_e and coordinates. v_{cc} is the pseudopotential of metal cationic cores effectively describing the influence of metal cationic cores on valence electrons in addition to the mean-field electrostatic force that is included elsewhere. The decay of v_{cc} from its bulk value v_{cc}^0 within the metal to zero outside the metal surface is modeled using an error function,

$$v_{cc} = \frac{v_{cc}^0}{2}[1 - \mathrm{erf}(x)]. \tag{70}$$

It should be noted that in this work v_{cc}^0 is calibrated to reproduce the experimentally measured potential of zero charge.

f_c describes the classical interactions between charged particles, which is a functional of the density of charged particles n_i and electric potential ϕ and its gradient $\nabla\phi$, written as,

$$\begin{aligned} f_c &= \left[(n_{cc} - n_e)e_0\phi - \frac{1}{2}\epsilon_{op}(\nabla\phi)^2\right] \\ &+ \left[(n_c - n_a)e_0\phi - n_s\beta^{-1}\ln\frac{\sinh(\beta p_s|\nabla\phi|)}{\beta p_s|\nabla\phi|}\right] \\ &+ \sum_{i=a,c,s}\beta^{-1}n_i\left(\ln\left(n_i\Lambda_i^3\right) - 1\right) + \Phi_{ex}(\{n_i\}), \end{aligned} \tag{71}$$

where n_{cc} is the number density of metal atomic-core charges, as only the valence electrons are explicitly considered in n_e. We can obtain the dimensionless $\bar{n}_{cc}^{metal} = 4N_{Au}^{ve}\left(\frac{a_0}{a_{Au}}\right)^3$ with N_{metal}^{ve}representing the number of valence electrons of metal atom, and a_{metal} is the lattice constant of the cubic closed-packed cell of metal. The first term on the right-hand side of Eq.(71) represents the Hartree energy of electrons and cationic cores of the electrode, and the self-energy of the electric field with ϵ_{op} being the optical permittivity, for example, $9.8\epsilon_0$ for Au and $3\epsilon_0$ for Ag[123,124]. The second term is the potential energies of charged particles in solution, with $n_i(i = a, c, s)$ the number density of anion, cation and solvent, $\beta = (k_B T)^{-1}$ the inverse thermal energy, and p_s the solvent dipole moment. The third term represents the Gibbs free energy of an ideal-gas reference system, with Λ_i denoting the thermal wavelength of species i. The fourth term, $\Phi_{ex}(\{n_i\})$, accounts for excess Gibbs free energy due to finite-size effects. In this work,

we adopt the Bikerman theory, a lattice gas approach that incorporates entropy of mixing in electrolyte solution[102–104]. The Bikerman theory assumes all charged particles occupy the same volume Λ_{B}, giving a maximum number density of $n_{\max} = (\Lambda_{\mathrm{B}})^{-3}$.

It is noted that, on the electrolyte solution side, the radius of the solvated cations is inherited from the analysis based on the GCS_pm model in Figure 11. The large value suggests that solvated cations contain multiple solvent layers. In our previous work[74,77,88], all trapped solvent molecules were frozen and a small optical dielectric permittivity was used for them. In this work, we make a more reasonable assumption that the solvent molecules beyond the first layer of the solvent cations can also shield the electric field via orientational polarization. In this refined description, the solvent molecules are divided into free ones with a number density of $n_{\mathrm{s}}^{\mathrm{free}}$ and trapped ones with a number density of $n_{\mathrm{s}}^{\mathrm{solv}}$, as shown in Figure 12(b). Therefore, the total number density of solvent molecules $n_{\mathrm{s}}^{\mathrm{total}}$ is expressed as,

$$n_{\mathrm{s}}^{\mathrm{total}} = n_{\mathrm{s}}^{\mathrm{free}} + n_{\mathrm{s}}^{\mathrm{solv}}, \qquad n_{\mathrm{s}}^{\mathrm{solv}} = (\gamma_{\mathrm{c}} + \gamma_{\mathrm{a}}) n_i, \tag{72}$$

where $n_{\mathrm{s}}^{\mathrm{total}}$ is the total number density of solvent molecules.

The number density of solvent molecules that can effectively shield the electric field is the sum of that of free solvent molecules and those trapped in the solvation shell beyond the first layer,

$$n_{\mathrm{s}}^{\mathrm{eff}} = n_{\mathrm{s}}^{\mathrm{free}} + \left(\gamma_{\mathrm{c}} - \gamma_{\mathrm{c}}^{\mathrm{in}}\right) n_{\mathrm{c}}, \tag{73}$$

where $\gamma_{\mathrm{c}}^{\mathrm{in}} = \left(\frac{2r_{\mathrm{c}}^{\mathrm{in}}}{R_{\mathrm{s}}}\right)^3$ is the relative size of cations only with the first solvation layer with a radius of $r_{\mathrm{c}}^{\mathrm{in}}$, which is estimated based on a combination of literature data[107,125].

f_{int} accounts for the specific short-range interactions between solution particles and metal electrons, written as,

$$f_{\mathrm{int}} = \sum_{\mathrm{i=a,c,s}} n_{\mathrm{i}} w_{\mathrm{i}}. \tag{74}$$

Following our recent work[76], we employ the repulsive part of the Morse potential to prevent ions and solvent molecules from penetrating into the metal phase. This interaction is written as,

$$w_{\mathrm{i}}(\vec{r}) = D_{\mathrm{mi}} \cdot \exp\left(-2\beta_{\mathrm{i}}(d(\vec{r}) - d_{\mathrm{mi}})\right), \tag{75}$$

where D_{mi} is the well depth, β_{i} is the coefficient controlling the well width, $d(\vec{r})$ is the distance from $\vec{r}$ to the metal surface edge, and d_{mi} denotes the equilibrium distance between the particle l and the metal surface. When $\vec{r}$ is within the metal, $d(\vec{r})$ is negative and $w_{\mathrm{i}}(\vec{r})$ becomes very positive, meaning that solution particles have a negligible probability there. The parameters in Eq.(75) can be determined from the Kohn-Sham DFT calculations[126]. For example, the DFT-calculated binding energy of water molecule on metal surface is approximately 0.25 eV, namely, $D_{\mathrm{ms}} = 0.25\ \mathrm{eV}$, and the typical equilibrium distance between the water molecules and the metal surface is about 1.0 Å, corresponding to $d_{\mathrm{ms}} = 1.89a_0$. This value appears smaller than the DFT-calculated bond length of 1.25 Å because the jellium edge is located approximately half a lattice constant beyond the outer surface of metal atoms[127–130].

The DPFT_sol model further considers the potential-dependent adsorption energy of solvent molecules. In the current framework, we allow the parameters of short-range metal-solvent interactions to vary with electrode potential. In a linear approximation, we assume,

$$D_{\mathrm{ms}} = D_{\mathrm{ms}}^0 + \alpha_{\mathrm{ms}}\big(E - E_{\mathrm{pzc}}\big)e_0, \tag{76}$$

$$d_{\mathrm{ms}} = d_{\mathrm{ms}}^0 - \beta_{\mathrm{ms}}\big(E - E_{\mathrm{pzc}}\big)e_0, \tag{77}$$

where D_{ms}^0 and d_{ms}^0 are the well depth and the equilibrium distance between the solvent molecule and the metal surface at the PZC, respectively. The adsorption energy of solvent becomes larger with increasing electrode potential[131–133], which means that the solvent molecules can approach the metal surface to a closer distance, as shown in Figure 12(c). The dimensionless slopes α_{ms} and β_{ms} are to be determined from fitting the experimental C_{dl}.

The DPFT_desol model improves over the DPFT_sol model by considering the partial desolvation of ion at highly charged surface, or in the GCS picture, the compression of the Stern layer[134]. In the current model framework, this means that γ_{i} depends on the local electric field and becomes spatially varying. Specifically, γ_{i} will decrease near the metal surface with a strong electric field that can 'liberate' trapped solvent molecules from the solvation shell, as shown in Figure 12(d). Without losing generality, we assume a linear relationship,

$$\frac{\gamma_{\mathrm{i}}}{\gamma_{\mathrm{i}}^0} = 1 - \zeta_{\mathrm{i}}(\bar{\nabla}\bar{\phi}), \tag{78}$$

where γ_{i}^{0} is the relative size of solvated ion in solution bulk, ζ_{i} is a relatively dimensionless coefficient indicating the degree of partial desolvation of ions. This parameter is to be estimated by fitting the DPFT_desol model with experimental C_{dl}.

3.3.1. Variational analysis

Variational analysis of $\mathscr{g}$ in terms of ϕ gives,

$$\frac{\partial \mathscr{g}}{\partial \phi} - \nabla \cdot \left(\frac{\partial \mathscr{g}}{\partial \nabla \phi} \right) = 0, \tag{79}$$

leading to,

$$-\nabla[\epsilon_{\mathrm{eff}} \nabla \phi] = e_0 (n_{\mathrm{cc}} - n_{\mathrm{e}}) + (n_{\mathrm{c}} - n_{\mathrm{a}}) e_0, \tag{80}$$

which is the Poisson equation with an effective dielectric function as in ref.[135–137]

$$\epsilon_{\mathrm{eff}} = \epsilon_{\mathrm{op}} + \frac{n_{\mathrm{s}} p_{\mathrm{s}}}{|\nabla \phi|} \mathcal{L}(\beta p_{\mathrm{s}} |\nabla \phi|), \tag{81}$$

with $\mathcal{L}(x) = \coth(x) - (x)^{-1}$ being the Langevin function.

Variational analysis of $\mathscr{g}$ in terms of particle number densities n_{i} should be divided into two cases. For the case of electrons, we obtain,

$$\nabla \cdot \left[\frac{\partial (t_{\mathrm{ni}} + u_{\mathrm{X}} + u_{\mathrm{C}})}{\partial \nabla n_{\mathrm{e}}} \right] = \frac{\partial (t_{\mathrm{ni}} + u_{\mathrm{X}} + u_{\mathrm{C}} + p_{\mathrm{cc}})}{\partial n_{\mathrm{e}}} - e_0 \phi - \tilde{\mu}_{\mathrm{e}}. \tag{82}$$

The electrochemical potential of electrons can be tuned by the electrode potential, E_{M},

$$\tilde{\mu}_{\mathrm{e}} = \mu_{\mathrm{e}} - e_0 E_{\mathrm{M}}, \tag{83}$$

with $\mu_{\mathrm{e}} = \frac{\partial t_{\mathrm{TF}}}{\partial \bar{n}_{\mathrm{e}}} + \frac{\partial u_{\mathrm{X}}^{0}}{\partial \bar{n}_{\mathrm{e}}} + \frac{\partial u_{\mathrm{C}}^{0}}{\partial \bar{n}_{\mathrm{e}}} + v_{\mathrm{cc}}$ being the chemical potential of a homogenous electron gas. Eq.(80) and (82) constitute the basic set of differential equations controlling the EDL. Next, we need to derive expressions of n_{i} as functions of ϕ. Variational analysis of $\mathscr{g}$ in terms of charged particles in solution gives the electrochemical potential of ions and solvent,

$$\tilde{\mu}_{\mathrm{a}} = \beta^{-1} \ln(n_{\mathrm{a}} \Lambda_{\mathrm{a}}^{3}) - e_0 \phi + w_{\mathrm{a}} + \mu_{\mathrm{a}}^{\mathrm{ex}},$$

$$\tilde{\mu}_{\mathrm{c}} = \beta^{-1}\ln(n_{\mathrm{c}}\Lambda_{\mathrm{c}}^{3}) + e_0\phi + w_{\mathrm{c}} + \mu_{\mathrm{c}}^{\mathrm{ex}},$$
$$\tilde{\mu}_{\mathrm{s}} = \beta^{-1}\ln(n_{\mathrm{s}}\Lambda_{\mathrm{s}}^{3}) - \beta^{-1}\ln\frac{\sinh(\beta p_{\mathrm{s}}|\nabla\phi|)}{\beta p_{\mathrm{s}}|\nabla\phi|} + w_{\mathrm{s}} + \mu_{\mathrm{s}}^{\mathrm{ex}}, \tag{84}$$

where $\mu_{\mathrm{i}}^{\mathrm{ex}}$ is the excess chemical potential given by,

$$\mu_{\mathrm{i}}^{\mathrm{ex}} = \frac{\delta\Phi_{\mathrm{ex}}}{\delta n_{\mathrm{i}}}. \tag{85}$$

The Bikerman theory gives,

$$\mu_{\mathrm{i}}^{\mathrm{ex}} = \beta^{-1}\ln\left(\frac{1}{1-\sum_{\mathrm{i=a,c,s}} n_{\mathrm{i}}\Lambda_{\mathrm{B}}^{3}}\right) \tag{86}$$

A more advanced description is the fundamental measure theory (FMT)[102,138,103,104,139], which has been compared with the Bikerman theory in a previous work[140].

From Eq.(84), n_{i} is given by,

$$\frac{n_{\mathrm{i}}\Lambda_{\mathrm{i}}^{3}}{1-\sum_{\mathrm{i=a,c,s}} n_{\mathrm{i}}\Lambda_{\mathrm{B}}^{3}} = \Theta_{\mathrm{i}}\exp(\beta\tilde{\mu}_{\mathrm{i}}), \tag{87}$$

where thermodynamic factors are given by,

$$\Theta_{\mathrm{a}} = \exp(\beta e_0\phi - \beta w_{\mathrm{a}}),$$
$$\Theta_{\mathrm{c}} = \exp(-\beta e_0\phi - \beta w_{\mathrm{c}}), \tag{88}$$
$$\Theta_{\mathrm{s}} = \exp\left(\ln\frac{\sinh(\beta p_{\mathrm{s}}|\nabla\phi|)}{\beta p_{\mathrm{s}}|\nabla\phi|} - \beta w_{\mathrm{s}}\right).$$

Eq.(88) shall be valid also in the solution bulk where $\Theta_{\mathrm{i}} = 1$, and $\tilde{\mu}_{\mathrm{i}}$ is uniform in the electrolyte solution. Combining these two conditions, we have the following equality,

$$\frac{n_{\mathrm{i}}\Lambda_{\mathrm{i}}^{3}}{1-n_{\mathrm{a}}^{\mathrm{b}}\Lambda_{\mathrm{B}}^{3}-n_{\mathrm{c}}^{\mathrm{b}}\Lambda_{\mathrm{B}}^{3}-n_{\mathrm{s}}^{\mathrm{b}}\Lambda_{\mathrm{B}}^{3}} = \Theta_{\mathrm{i}}\frac{n_{\mathrm{i}}^{\mathrm{b}}\Lambda_{\mathrm{i}}^{3}}{1-n_{\mathrm{a}}^{\mathrm{b}}\Lambda_{\mathrm{B}}^{3}-n_{\mathrm{c}}^{\mathrm{b}}\Lambda_{\mathrm{B}}^{3}-n_{\mathrm{s}}^{\mathrm{b}}\Lambda_{\mathrm{B}}^{3}}. \tag{89}$$

We have,

$$n_{\mathrm{i}} = n_{\max}\frac{\chi_{\mathrm{i}}\Theta_{\mathrm{i}}}{1+\chi_{\mathrm{a}}(\Theta_{\mathrm{a}}-1)+\chi_{\mathrm{c}}(\Theta_{\mathrm{c}}-1)+\chi_{\mathrm{s}}(\Theta_{\mathrm{s}}-1)}. \tag{90}$$

with dimensionless bulk number densities $\chi_{\mathrm{i}} = n_{\mathrm{i}}^{\mathrm{b}}/n_{\max}$.

Eq.(90) can be extended, in a phenomenological manner, to scenarios of unequal sizes,

$$n_{\mathrm{i}} = n_{\max}\frac{\chi_{\mathrm{i}}\Theta_{\mathrm{i}}}{\Omega}. \tag{91}$$

where $\Omega = 1+\gamma_{\mathrm{a}}\chi_{\mathrm{a}}(\Theta_{\mathrm{a}}-1)+\gamma_{\mathrm{c}}\chi_{\mathrm{c}}(\Theta_{\mathrm{c}}-1)+\gamma_{\mathrm{s}}\chi_{\mathrm{s}}(\Theta_{\mathrm{s}}-1)$ is the normalization factor, and γ_{i} is the relative size of particles of the type i referenced to Λ_{B}.

3.3.2. Numerical implementation

In this section, we further process the governing equations in Eq.(80) and (82) to facilitate numerical computations. We define dimensionless variables, marked with overlines, as follows:

$$\bar{n}_{\mathrm{i}} = n_{\mathrm{i}}(a_0)^3, \bar{x} = \frac{x}{a_0}, \bar{\phi} = \frac{e_0\phi}{k_{\mathrm{B}}T}, \bar{p_{\mathrm{s}}} = \frac{p_{\mathrm{s}}}{e_0 a}, \bar{q}_{\mathrm{i}} = \frac{q_{\mathrm{i}}}{e_0}, \bar{\epsilon}_{\mathrm{op}} = \frac{\epsilon_{\mathrm{op}}}{\epsilon_0}$$

where ϵ_0 is the dielectric permittivity of vacuum. Then we rewrite Eq.(80) in a nondimensional form,

$$-\bar{\nabla}\cdot\left(\bar{\epsilon}_{\mathrm{op}}\bar{\nabla}\bar{\phi}+\bar{n}_{\mathrm{s}}^{\mathrm{eff}}\bar{p_{\mathrm{s}}}\kappa\mathcal{L}\right) = \kappa\left((\bar{n}_{\mathrm{cc}}-\bar{n}_{\mathrm{e}})+(\bar{n}_{\mathrm{c}}-\bar{n}_{a})\right), \tag{92}$$

where $\kappa = \frac{e_0^2}{k_{\mathrm{B}}T\epsilon_0 a_0}$ is a number derived from fundamental constants.

We can rewrite Eq.(82) in terms of the dimensionless electron density, $\bar{n}_{\mathrm{e}} = n_{\mathrm{e}}a_0^3$,

$$\bar{\nabla}\cdot\left[\frac{\partial(t_{\mathrm{ni}}+u_{\mathrm{X}}+u_{\mathrm{C}})}{\partial\bar{\nabla}\bar{n}_{\mathrm{e}}}\right] = \frac{\partial(t_{\mathrm{ni}}+u_{\mathrm{X}}+u_{\mathrm{C}}+p_{\mathrm{cc}})}{\partial\bar{n}_{\mathrm{e}}} - a_0^{-3}(e_0\phi+\tilde{\mu}_{\mathrm{e}}), \tag{93}$$

where the terms are obtained as,

$$\begin{aligned}\frac{\partial(t_{\mathrm{ni}}+u_{\mathrm{X}}+u_{\mathrm{C}})}{\partial\bar{\nabla}\bar{n}_{\mathrm{e}}} &= \frac{\partial(t_{\mathrm{ni}}+u_{\mathrm{X}}+u_{\mathrm{C}})}{\partial s^2}\frac{\partial s^2}{\partial\bar{\nabla}\bar{n}_{\mathrm{e}}}\\ &= \frac{e_{\mathrm{au}}a_0^{-3}\left(\left(\frac{\partial F_s(s)}{\partial s^2}+\theta_{\mathrm{T}}\right)t_{\mathrm{TF}}+\theta_{\mathrm{XC}}u_{\mathrm{X}}^0\right)}{2(3\pi^2)^{\frac{2}{3}}(\bar{n}_{\mathrm{e}})^{\frac{8}{3}}}\bar{\nabla}\bar{n}_{\mathrm{e}},\end{aligned} \tag{94}$$

with $\theta_{\mathrm{XC}} = \theta_{\mathrm{X}} - \frac{\pi^2}{3}\theta_{\mathrm{C}}$, and

$$\frac{\partial(t_{\mathrm{ni}} + u_{\mathrm{X}} + u_{\mathrm{C}} + p_{\mathrm{cc}})}{\partial \bar{n}_{\mathrm{e}}}$$

$$= e_{\mathrm{au}} a_0^{-3}[(F_s(s) + \theta_{\mathrm{T}} s^2)\frac{\partial t_{\mathrm{TF}}}{\partial \bar{n}_{\mathrm{e}}} + (1 + \theta_{\mathrm{XC}} s^2)\frac{\partial u_{\mathrm{X}}^0}{\partial \bar{n}_{\mathrm{e}}} + \frac{\partial u_{\mathrm{C}}^0}{\partial \bar{n}_{\mathrm{e}}} + \left(\left(\frac{\partial F_s(s)}{\partial s^2} + \theta_{\mathrm{T}}\right)t_{\mathrm{TF}} + \theta'_{\mathrm{X}} u_{\mathrm{X}}^0\right)\frac{\partial s^2}{\partial \bar{n}_{\mathrm{e}}} + v_{\mathrm{cc}}], \tag{95}$$

with,

$$\frac{\partial t_{\mathrm{TF}}}{\partial \bar{n}_{\mathrm{e}}} = \frac{1}{2}(3\pi^2)^{\frac{2}{3}}(\bar{n}_{\mathrm{e}})^{\frac{2}{3}} \tag{96}$$

$$\frac{\partial s^2}{\partial \bar{n}_{\mathrm{e}}} = -\frac{8}{3}\frac{(\overline{\nabla}\bar{n}_e)^2}{4(3\pi^2)^{\frac{2}{3}}(\bar{n}_{\mathrm{e}})^{\frac{11}{3}}} = \frac{-8}{3\bar{n}_{\mathrm{e}}}s^2 \tag{97}$$

$$\frac{\partial u_{\mathrm{X}}^0}{\partial \bar{n}_{\mathrm{e}}} = -\left(\frac{3}{\pi}\right)^{\frac{1}{3}}(\bar{n}_{\mathrm{e}})^{\frac{1}{3}} \tag{98}$$

$$\frac{\partial u_{\mathrm{C}}^0}{\partial \bar{n}_{\mathrm{e}}} = -2\alpha_1(1 + \alpha_2 r_s)\ln\left(1 + \frac{1}{\xi}\right) - 2\alpha_1 \bar{n}_e\left(-\frac{1}{3}\left(\frac{3}{4\pi}\right)^{\frac{1}{3}}(\bar{n}_{\mathrm{e}})^{-\frac{4}{3}}\right)\cdot$$

$$\left(\alpha_2 \ln\left(1 + \frac{1}{\xi}\right) - \frac{(1 + \alpha_2 r_s)}{\xi(1 + \xi)}\alpha_1\left(\alpha_3 r_s^{-\frac{1}{2}} + 2\alpha_4 + 3\alpha_5 r_s^{\frac{1}{2}} + 4\alpha_6 r_s\right)\right) \tag{99}$$

$$= -2\alpha_1(1 + \alpha_2 r_s)\ln\left(1 + \frac{1}{\xi}\right)$$

$$+ \frac{2\alpha_1 r_s}{3}\left(\alpha_2 \ln\left(1 + \frac{1}{\xi}\right) - \frac{\alpha_1(1 + \alpha_2 r_s)}{\xi(1 + \xi)}\left(\alpha_3 r_s^{-\frac{1}{2}} + 2\alpha_4 + 3\alpha_5 r_s^{\frac{1}{2}} + 4\alpha_6 r_s\right)\right).$$

We expand the term on the right most side of Eq.(94),

$$\overline{\nabla}\cdot\left[\frac{\left(\left(\frac{\partial F_s(s)}{\partial s^2}+\theta_{\mathrm{T}}\right)t_{\mathrm{TF}}+\theta_{\mathrm{XC}}u_{\mathrm{X}}^0\right)}{(\bar{n}_{\mathrm{e}})^{\frac{8}{3}}}\overline{\nabla}\bar{n}_{\mathrm{e}}\right]=\frac{\left(\left(\frac{\partial F_s(s)}{\partial s^2}+\theta_{\mathrm{T}}\right)t_{\mathrm{TF}}+\theta_{\mathrm{XC}}u_{\mathrm{X}}^0\right)}{(\bar{n}_{\mathrm{e}})^{\frac{8}{3}}}\overline{\nabla}^2\bar{n}_{\mathrm{e}}$$

$$-\overline{\nabla}\cdot\left[\frac{\left(\left(\frac{\partial F_s(s)}{\partial s^2}+\theta_{\mathrm{T}}\right)t_{\mathrm{TF}}+\theta_{\mathrm{XC}}u_{\mathrm{X}}^0\right)}{(\bar{n}_{\mathrm{e}})^{\frac{8}{3}}}\right]\overline{\nabla}\bar{n}_{\mathrm{e}}$$

$$=\frac{\left(\left(\frac{\partial F_s(s)}{\partial s^2}+\theta_{\mathrm{T}}\right)t_{\mathrm{TF}}+\theta_{\mathrm{XC}}u_{\mathrm{X}}^0\right)}{(\bar{n}_{\mathrm{e}})^{\frac{8}{3}}}\overline{\nabla}^2\bar{n}_{\mathrm{e}} \tag{100}$$

$$+\frac{\left(\frac{\partial F_s(s)}{\partial s^2\partial\bar{n}_{\mathrm{e}}}t_{\mathrm{TF}}+\left(\frac{\partial F_s(s)}{\partial s^2}+\theta_{\mathrm{T}}\right)\frac{\partial t_{\mathrm{TF}}}{\partial\bar{n}_{\mathrm{e}}}+\theta_{\mathrm{XC}}\frac{\partial u_{\mathrm{X}}^0}{\partial\bar{n}_{\mathrm{e}}}\right)}{(\bar{n}_{\mathrm{e}})^{\frac{8}{3}}}(\overline{\nabla}\bar{n}_{\mathrm{e}})^2$$

$$-\frac{8}{3}\frac{\left(\left(\frac{\partial F_s(s)}{\partial s^2}+\theta_{\mathrm{T}}\right)t_{\mathrm{TF}}+\theta_{\mathrm{XC}}u_{\mathrm{X}}^0\right)}{(\bar{n}_{\mathrm{e}})^{\frac{11}{3}}}(\overline{\nabla}\bar{n}_{\mathrm{e}})^2.$$

Combining Eq.(93), (94) and (95), we get,

$$\overline{\nabla}^2\bar{n}_{\mathrm{e}}=\frac{2(3\pi^2)^{\frac{2}{3}}(\bar{n}_{\mathrm{e}})^{\frac{8}{3}}}{\left(\frac{\partial F_s(s)}{\partial s^2}+\theta_{\mathrm{T}}\right)t_{\mathrm{TF}}+\theta_{\mathrm{XC}}u_{\mathrm{X}}^0}[(F_s(s)+\theta_{\mathrm{T}}s^2)\frac{\partial t_{\mathrm{TF}}}{\partial\bar{n}_{\mathrm{e}}}+(1+\theta_{\mathrm{XC}}s^2)\frac{\partial u_{\mathrm{X}}^0}{\partial\bar{n}_{\mathrm{e}}}+\frac{\partial u_{\mathrm{C}}^0}{\partial\bar{n}_{\mathrm{e}}}$$

$$+\left(\left(\frac{\partial F_s(s)}{\partial s^2}+\theta_{\mathrm{T}}\right)t_{\mathrm{TF}}+\theta_{\mathrm{XC}}u_{\mathrm{X}}^0\right)\frac{\partial s^2}{\partial\bar{n}_{\mathrm{e}}}+v_{\mathrm{cc}}-\frac{(e_0\phi+\tilde{\mu}_{\mathrm{e}})}{e_{\mathrm{au}}}] \tag{101}$$

$$+\frac{8}{3}(\bar{n}_{\mathrm{e}})^{-1}(\overline{\nabla}\bar{n}_{\mathrm{e}})^2-\frac{\frac{\partial F_s(s)}{\partial s^2\partial\bar{n}_{\mathrm{e}}}t_{\mathrm{TF}}+\left(\frac{\partial F_s(s)}{\partial s^2}+\theta_{\mathrm{T}}\right)\frac{\partial t_{\mathrm{TF}}}{\partial\bar{n}_{\mathrm{e}}}+\theta_{\mathrm{XC}}\frac{\partial u_{\mathrm{X}}^0}{\partial\bar{n}_{\mathrm{e}}}}{\left(\frac{\partial F_s(s)}{\partial s^2}+\theta_{\mathrm{T}}\right)t_{\mathrm{TF}}+\theta_{\mathrm{XC}}u_{\mathrm{X}}^0}(\overline{\nabla}\bar{n}_{\mathrm{e}})^2.$$

Substituting Eq.(97) into Eq.(101), and using $s=|\overline{\nabla}\bar{n}_{\mathrm{e}}|/\left(2(3\pi^2)^{\frac{1}{3}}(\bar{n}_{\mathrm{e}})^{\frac{4}{3}}\right)$, we get,

$$\overline{\nabla}^2\bar{n}_{\mathrm{e}}=\frac{2(3\pi^2)^{\frac{2}{3}}(\bar{n}_{\mathrm{e}})^{\frac{8}{3}}}{\left(\frac{\partial F_s(s)}{\partial s^2}+\theta_{\mathrm{T}}\right)t_{\mathrm{TF}}+\theta_{\mathrm{XC}}u_{\mathrm{X}}^0}\left(F_s(s)\frac{\partial t_{\mathrm{TF}}}{\partial\bar{n}_{\mathrm{e}}}+\frac{\partial u_{\mathrm{X}}^0}{\partial\bar{n}_{\mathrm{e}}}+\frac{\partial u_{\mathrm{C}}^0}{\partial\bar{n}_{\mathrm{e}}}+v_{\mathrm{cc}}-\frac{(e_0\phi+\tilde{\mu}_{\mathrm{e}})}{e_{\mathrm{au}}}\right) \tag{102}$$

$$+\left(\frac{4}{3}(\bar{n}_{\mathrm{e}})^{-1}-\frac{2\frac{\partial F_s(s)}{\partial s^2\partial\bar{n}_{\mathrm{e}}}t_{\mathrm{TF}}+\left(2\frac{\partial F_s(s)}{\partial s^2}+\theta_{\mathrm{T}}\right)\frac{\partial t_{\mathrm{TF}}}{\partial\bar{n}_{\mathrm{e}}}+\theta_{\mathrm{XC}}\frac{\partial u_{\mathrm{X}}^0}{\partial\bar{n}_{\mathrm{e}}}}{2\left(\left(\frac{\partial F_s(s)}{\partial s^2}+\theta_{\mathrm{T}}\right)t_{\mathrm{TF}}+\theta_{\mathrm{XC}}u_{\mathrm{X}}^0\right)}\right)(\bar{\nabla}\bar{n}_{\mathrm{e}})^2.$$

Since, $\frac{\partial t_{\mathrm{TF}}}{\partial\bar{n}_{\mathrm{e}}}=\frac{5t_{\mathrm{TF}}}{3\bar{n}_{\mathrm{e}}}$, $\frac{\partial u_{\mathrm{X}}^0}{\partial\bar{n}_{\mathrm{e}}}=\frac{4u_{\mathrm{X}}^0}{3\bar{n}_{\mathrm{e}}}$, we obtain,

$$\begin{aligned}&\frac{4}{3}(\bar{n}_{\mathrm{e}})^{-1}-\frac{2\frac{\partial F_s(s)}{\partial s^2\partial\bar{n}_{\mathrm{e}}}t_{\mathrm{TF}}+\left(2\frac{\partial F_s(s)}{\partial s^2}+\theta_{\mathrm{T}}\right)\frac{\partial t_{\mathrm{TF}}}{\partial\bar{n}_{\mathrm{e}}}+\theta_{\mathrm{XC}}\frac{\partial u_{\mathrm{X}}^0}{\partial\bar{n}_{\mathrm{e}}}}{2\left(\left(\frac{\partial F_s(s)}{\partial s^2}+\theta_{\mathrm{T}}\right)t_{\mathrm{TF}}+\theta_{\mathrm{XC}}u_{\mathrm{X}}^0\right)}\\&=\frac{\left(\theta_{\mathrm{T}}t_{\mathrm{TF}}+\frac{4}{3}\theta_{\mathrm{XC}}u_{\mathrm{X}}^0\right)-2\bar{n}_{\mathrm{e}}\frac{\partial F_s(s)}{\partial s^2\partial\bar{n}_{\mathrm{e}}}t_{\mathrm{TF}}-\frac{2}{3}\frac{\partial F_s(s)}{\partial s^2}t_{\mathrm{TF}}}{2\bar{n}_{\mathrm{e}}\left(\left(\frac{\partial F_s(s)}{\partial s^2}+\theta_{\mathrm{T}}\right)t_{\mathrm{TF}}+\theta_{\mathrm{XC}}u_{\mathrm{X}}^0\right)}.\end{aligned}\tag{103}$$

In the end, we reformulate Eq.(102) as,

$$\begin{aligned}&\bar{\nabla}^2\bar{n}_{\mathrm{e}}=\frac{20}{3}\bar{n}_{\mathrm{e}}\frac{\omega}{\left(\frac{\partial F_s(s)}{\partial s^2}+\theta_{\mathrm{T}}\right)\omega-\theta_{\mathrm{XC}}}\left(F_s(s)\frac{\partial t_{\mathrm{TF}}}{\partial\bar{n}_{\mathrm{e}}}+\frac{\partial u_{\mathrm{X}}^0}{\partial\bar{n}_{\mathrm{e}}}+\frac{\partial u_{\mathrm{C}}^0}{\partial\bar{n}_{\mathrm{e}}}+v_{\mathrm{cc}}-\frac{(e_0\phi+\tilde{\mu}_{\mathrm{e}})}{e_{\mathrm{au}}}\right)\\&+\frac{\theta_{\mathrm{T}}\omega-\frac{4}{3}\theta_{\mathrm{XC}}-2\bar{n}_{\mathrm{e}}\frac{\partial F_s(s)}{\partial s^2\partial\bar{n}_{\mathrm{e}}}\omega-\frac{2}{3}\frac{\partial F_s(s)}{\partial s^2}\omega}{2\bar{n}_{\mathrm{e}}\left(\left(\frac{\partial F_s(s)}{\partial s^2}+\theta_{\mathrm{T}}\right)\omega-\theta_{\mathrm{XC}}\right)}(\bar{\nabla}\bar{n}_{\mathrm{e}})^2.\end{aligned}\tag{104}$$

with $\omega=\frac{2}{5}\pi^{\frac{5}{3}}3^{\frac{1}{3}}(\bar{n}_{\mathrm{e}})^{\frac{1}{3}}$, which is the general form of the controlling equation for the electron density. Specifically, the Eq.(104) can be reduced to,

$$\begin{aligned}&\bar{\nabla}^2\bar{n}_{\mathrm{e}}=\frac{20}{3}\bar{n}_{\mathrm{e}}\frac{\omega}{\theta_{\mathrm{T}}\omega-\theta_{\mathrm{XC}}}\left(\frac{\partial t_{\mathrm{TF}}}{\partial\bar{n}_{\mathrm{e}}}+\frac{\partial u_{\mathrm{X}}^0}{\partial\bar{n}_{\mathrm{e}}}+\frac{\partial u_{\mathrm{C}}^0}{\partial\bar{n}_{\mathrm{e}}}+v_{\mathrm{cc}}-\frac{(e_0\phi+\tilde{\mu}_{\mathrm{e}})}{e_{\mathrm{au}}}\right)\\&+\frac{\theta_{\mathrm{T}}\omega-\frac{4}{3}\theta_{\mathrm{XC}}}{2\bar{n}_{\mathrm{e}}(\theta_{\mathrm{T}}\omega-\theta_{\mathrm{XC}})}(\bar{\nabla}\bar{n}_{\mathrm{e}})^2,\end{aligned}\tag{105}$$

for the TFvW functional,

$$\bar{\nabla}^2\bar{n}_{\mathrm{e}} = \frac{20}{3}\bar{n}_{\mathrm{e}}\frac{\omega}{\left(\theta_{\mathrm{T}} - \mu e^{-\mu s^2} + 3\mu^2 s^2 e^{-\mu s^2}\right)\omega - \theta_{\mathrm{XC}}}\left(e^{-\mu s^2}\frac{\partial t_{\mathrm{TF}}}{\partial \bar{n}_{\mathrm{e}}} + \frac{\partial u_{\mathrm{X}}^0}{\partial \bar{n}_{\mathrm{e}}} + \frac{\partial u_{\mathrm{C}}^0}{\partial \bar{n}_{\mathrm{e}}} + v_{\mathrm{cc}} - \frac{(e_0\phi + \tilde{\mu}_{\mathrm{e}})}{e_{\mathrm{au}}}\right) + \frac{\left(\theta_{\mathrm{T}} + \frac{2}{3}\mu e^{-\mu s^2} + \frac{20}{3}\mu^2 s^2 e^{-\mu s^2}\right)\omega - \frac{4}{3}\theta_{\mathrm{XC}}}{2\bar{n}_{\mathrm{e}}\left(\left(\theta_{\mathrm{T}} - \mu e^{-\mu s^2} + 3\mu^2 s^2 e^{-\mu s^2}\right)\omega - \theta_{\mathrm{XC}}\right)}(\bar{\nabla}\bar{n}_{\mathrm{e}})^2. \tag{106}$$

3.3.3. Calculation of thermodynamic properties

C_{dl} is calculated by differentiating the surface free charge density σ_{free} with respect to electrode potential E_{M},

$$C_{\mathrm{dl}} = \frac{\partial \sigma_{\mathrm{free}}}{\partial E_{\mathrm{M}}}. \tag{107}$$

$\tilde{\mu}_{\mathrm{e}}$ is related to the E_{M}, referenced to the standard hydrogen electrode (SHE) scale[141,142], as follows,

$$-\tilde{\mu}_{\mathrm{e}} = e_0(E_{\mathrm{M}} + 4.44\ \mathrm{V}) - e_0\chi_{\mathrm{s}}^{\mathrm{v}}, \tag{108}$$

where $\chi_{\mathrm{s}}^{\mathrm{v}}$ is the surface potential at the solution-vacuum interface[143]. By applying this relationship, we can rewrite Eq.(107),

$$C_{\mathrm{dl}} = -e_0\frac{\partial \sigma_{\mathrm{free}}}{\partial \tilde{\mu}_{\mathrm{e}}} = \frac{e_0^2}{a_0^2}\frac{\partial}{\partial \tilde{\mu}_{\mathrm{e}}}\int d\bar{x}(\bar{n}_{\mathrm{c}} - \bar{n}_{\mathrm{a}}), \tag{109}$$

with $\sigma_{\mathrm{free}} = -\frac{e_0}{a_0^2}\int d\bar{x}(\bar{n}_{\mathrm{c}} - \bar{n}_{\mathrm{a}})$, where $\bar{n}_{\mathrm{c}}$ and $\bar{n}_{\mathrm{a}}$ represent the dimensionless number densities of cation and anion, respectively.

The surface tension γ can be obtained using the Lippmann equation, which is, up to a constant, the integral of σ_{free} over the electrode potential[37]. In this work, we examine the relative surface tension, $\Delta\gamma$, referenced to their values at the PZFC,

$$\Delta\gamma = \left[-\int_{E_{\mathrm{pzfc}}}^{E_{\mathrm{M}}}\sigma_{\mathrm{free}}dE\right]_{T,\mu_i}. \tag{110}$$

The excess grand-canonical potential density, G_{exe}, is derived from the integration of the volumetric grand-canonical potential of interfaces over space as defined in Eq.(67), written as,

$$\Delta G_{\mathrm{exe}} = G_{\mathrm{exe}}(E_{\mathrm{M}}) - G_{\mathrm{exe}}\left(E_{\mathrm{pzfc}}\right),$$
$$G_{\mathrm{exe}}(E_{\mathrm{M}}) = \int_0^L g(E_{\mathrm{M}})dx - \left(\int_0^{L_{\mathrm{M}}} g_{\mathrm{m}}dx + \int_{L_{\mathrm{M}}}^L g_{\mathrm{sol}}dx\right), \quad (111)$$

where the last two terms in the bracket are the grand-canonical potential of the bulk metal and the bulk solution, respectively.

The surface stress g of the solid metal-solution interfaces in one-dimension is calculated using the Shuttleworth equation[52,41,43,12,46],

$$g = \gamma + \left(\frac{\partial \gamma}{\partial \epsilon}\right)_{T,\mu_i,E}, \quad (112)$$

where ϵ denotes the elastic strain, defined as $d\epsilon = \frac{d\mathrm{A}}{\mathrm{A}_0}$, indicating the relative change in surface area. In the one-dimensional case, $\mathcal{E}$ is changed by tuning the metal lattice constant $a_{\mathrm{cc}}^{\mathrm{metal}}$, written as,

$$d\epsilon = da_{\mathrm{cc}}^{\mathrm{metal}}. \quad (113)$$

And then, $\bar{n}_{\mathrm{cc}}^{\mathrm{metal}} = 4N_{\mathrm{metal}}^{\mathrm{ve}}\left(\frac{a_0}{a_{\mathrm{cc}}^{\mathrm{metal}}}\right)^2 \cdot \frac{a_0}{a_{\mathrm{cc}}^{\mathrm{metal}}+d\epsilon}$ is changed correspondingly.

Following numerical implementation, we evaluate the surface tension γ and surface stress g of metal-solution interfaces under constant potential conditions. The workflow begins with calibration of the pseudopotential coefficient v_{cc}^0 using experimental C_{dl} data for Au and Ag electrodes in aqueous solution. Thermodynamic consistency is then verified by comparing $\Delta\gamma$ and ΔG_{exe}. After validation, an elastic strain is introduced to the model to calculate the potential-dependent surface stress, g.

3.4. Summary

In this chapter, the theoretical models used to describe electrical double layers at metal–solution interfaces were introduced and critically examined. The classical GCS framework, together with its finite-ion-size extensions such as the BPB formulation, was presented in detail, including the derivation of governing equations, boundary conditions, and expressions for the differential double-layer capacitance. Through systematic comparison with experimental C_{dl} data for mercury electrodes across a wide range of electrolyte compositions and electrode potentials, the strengths and limitations of the classical GCS-based models were clearly identified.

While the GCS framework captures essential electrostatic features near the potential of zero charge, it fails to reproduce key experimental observations at highly charged states, including asymmetric capacitance profiles, electrolyte-specific effects, and deviations arising under far-from-zero-charge conditions. These deficiencies stem from the inherent assumptions of classical EDL theory, such as point-like ions, fixed dielectric properties, and the neglect of the electron spillover.

To overcome these limitations, the semiclassical DPFT framework was introduced as a more physically grounded and thermodynamically consistent alternative. By coupling an orbital-free quantum mechanical description of the metal with a statistical field representation of the electrolyte under constant-potential conditions, DPFT provides the foundation for the advanced modeling of EDL structure, interfacial thermodynamics, and mechanical response developed in the following chapters. Chapters 4–6 build directly on this framework to address highly charged interfaces, surface stress at solid-liquid interfaces, and morphology evolution at stepped electrodes.

Chapter 4. Microstructure of EDL at highly charged states

*Reproduced with minor changes from '**Zhang Z**, Huang J*, Microstructure of Electrical Double Layers at Highly Charged States[J]. JACS Au, 2025, 5 (7), 3453-3467'.*

4.1. Introduction

Electrochemical reactions of technological relevance often occur at electrode potentials far from the PZC, where the EDL is highly charged and strongly perturbed. In this regime, classical descriptions of the EDL become increasingly unreliable, yet a quantitative understanding of interfacial structure and thermodynamics is essential for interpreting electrolyte effects in electrocatalysis. Mercury electrodes provide an ideal model system for investigating EDL behavior under such conditions, as they exhibit negligible specific adsorption and possess exceptionally well-characterized C_{dl} data over a wide potential range and across diverse electrolyte compositions.

Building on the theoretical foundations established in **Chapter 3**, the central aim of this chapter is to identify the key physical mechanisms governing EDL behavior at highly charged interfaces. Particular emphasis is placed on the role of interfacial permittivity, short-range metal-solvent interactions, and ion solvation structure. By systematically refining the DPFT framework and validating it against experimental capacitance data, this chapter establishes a physically grounded description of EDL structure under far-from-zero-charge conditions.

4.2. Improved agreement with experiments from DPFT to DPFT_desol

The improvement of the DPFT_desol model over the DPFT model is examined using the experimental C_{dl} in Hg-NaF aqueous solution[105]. Figure 13 shows the comparison between experiments and the DPFT model. On the solution side, the ion radius r_i, solvent diameter R_{s}, and the bulk permittivity $\epsilon_{\mathrm{s}}^{\mathrm{b}}$, are the same as those determined using the GCS model, as shown in **Table 1**. The fitting parameters are $\theta_{\mathrm{T}} = 1.53$, $\bar{\epsilon}_{\mathrm{op}} = 3.70$, $\beta_{\mathrm{l}} = 1$, $D_{\mathrm{ma(c)}} = D_{\mathrm{ms}}/6$, and $d_{\mathrm{ma(c)}} = 7.56a_0 = 4$ Å. Herein, the fitted θ_{T} has a large influence on the PZC and reflects the overall quantum mechanical interactions of all mercury electrons, so it is different from the commonly used value of $5/3$ for single-electron systems[122]. The fitted optical permittivity $\bar{\epsilon}_{\mathrm{op}}$ is within the common range between 3 and 6[106]. The value of β_{l}, which corresponds to 0.53 $\mathrm{Å}^{-1}$, is close to the typical range of 0.4 and 1.1 $\mathrm{Å}^{-1}$ for this kind of system[144]. $D_{\mathrm{ma(c)}}$ is smaller than D_{ms} because ions are

nonspecifically adsorbed here. $d_{\mathrm{ma(c)}}$ is larger than d_{ms}, meaning that the solvent can approach the metal surface to a closer distance than the ions[131].

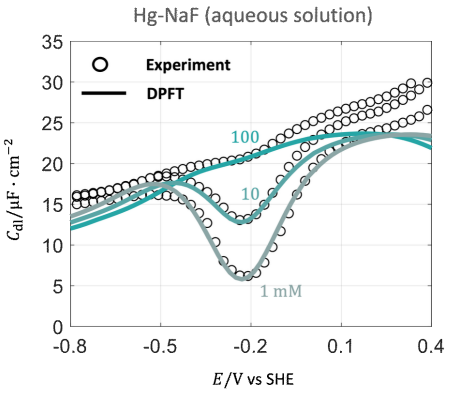

Figure 13. Comparison of C_{dl} between experimental results (circle) and DPFT model results (solid line) in Hg-NaF aqueous solution at varying ion concentrations. Calibrated parameters are $\theta_{\mathrm{T}} = 1.53$, $\bar{\epsilon}_{\mathrm{op}} = 3.70$, $\beta_{\mathrm{l}} = 1$, $D_{\mathrm{ma(c)}} = D_{\mathrm{ms}}/6$, and $d_{\mathrm{ma(c)}} = 7.56a_0$. Other parameters are given in SI. Experimental data are obtained from Grahame et al[105]. The electrode potential is transformed to the SHE scale.

Focusing on C_{dl} in this section, we defer a discussion on detailed distributions of interfacial properties calculated by the DPFT model to the following section. The DPFT model can well reproduce the experimental C_{dl} profiles in the vicinity of the PZC at the three ion concentrations. However, beyond the vicinity of the PZC, the model results deviate noticeably from the experimental data. We show the deviation between the DPFT model and experimental data of 100 mM NaF in Figure 14.

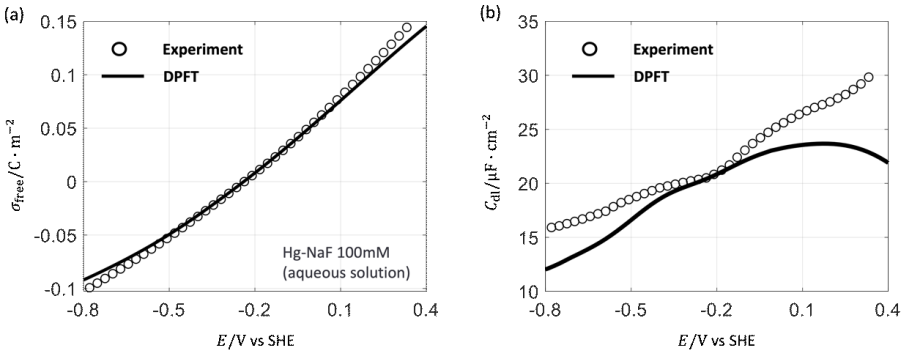

Figure 14. Comparison of (a) σ_{free} and (b) C_{dl} profiles between experimental results (circle) and the DPFT model results (solid line) for the Hg-NaF aqueous solution interface at 100mM.

The improvement of DPFT_sol and DPFT_desol models over the DPFT model is shown in terms of the surface charging relationship, namely, σ_{free} versus E relationship, in Figure 15(a, b). The corresponding C_{dl} profiles are shown in Figure 15(c) and Figure 17(a). As shown in Figure 15(a, c), the DPFT_sol model, introducing the potential-dependent short-range metal-solvent interactions, improves the agreement with the experimental data in the positively charged potential range of $-0.2 < E < 0.1$ V vs. SHE. While the variation of D_{ms} and d_{ms} is small within the given electrode potential regions, as shown in Figure 17(c), but the improvement of C_{dl} in Figure 15(c) is significant. The potential-dependent short-range metal-solvent interactions influence the free solvent density and the effective permittivity in the diffuse layer ($4 - 10$ Å), as depicted in Figure 22(a) and (b), leading to the observed improvement. These changes alter the electrostatic potential and ion density. A more detailed analysis will be provided in the following section.

However, the divergence between experimental data and the DPFT_sol model is still significant in highly positive and negative potential ranges. The DPFT_desol model, further introducing the partial desolvation of ions at highly charged surfaces, well reproduces the experimental σ_{free} and C_{dl} profiles in whole potential range, as shown in Figure 15(b), (c) and Figure 17(a). Figure 17(b) shows an improved agreement between the DPFT_desol model and experimental results at varying ion concentrations, *c.f.* Figure 13 for the DPFT model. The fitted coefficients are $\alpha_{\mathrm{ms}} = 0.05, \beta_{\mathrm{ms}} = 0.40, \zeta_{\mathrm{Na^+}} = 0.71, \zeta_{\mathrm{F^-}} = 1.11$. The key element of the improvement of the DPFT_desol model over the DPFT_sol model is the partial desolvation of electrolyte ions, leading to changes in the effective ion size with the electrode potential.

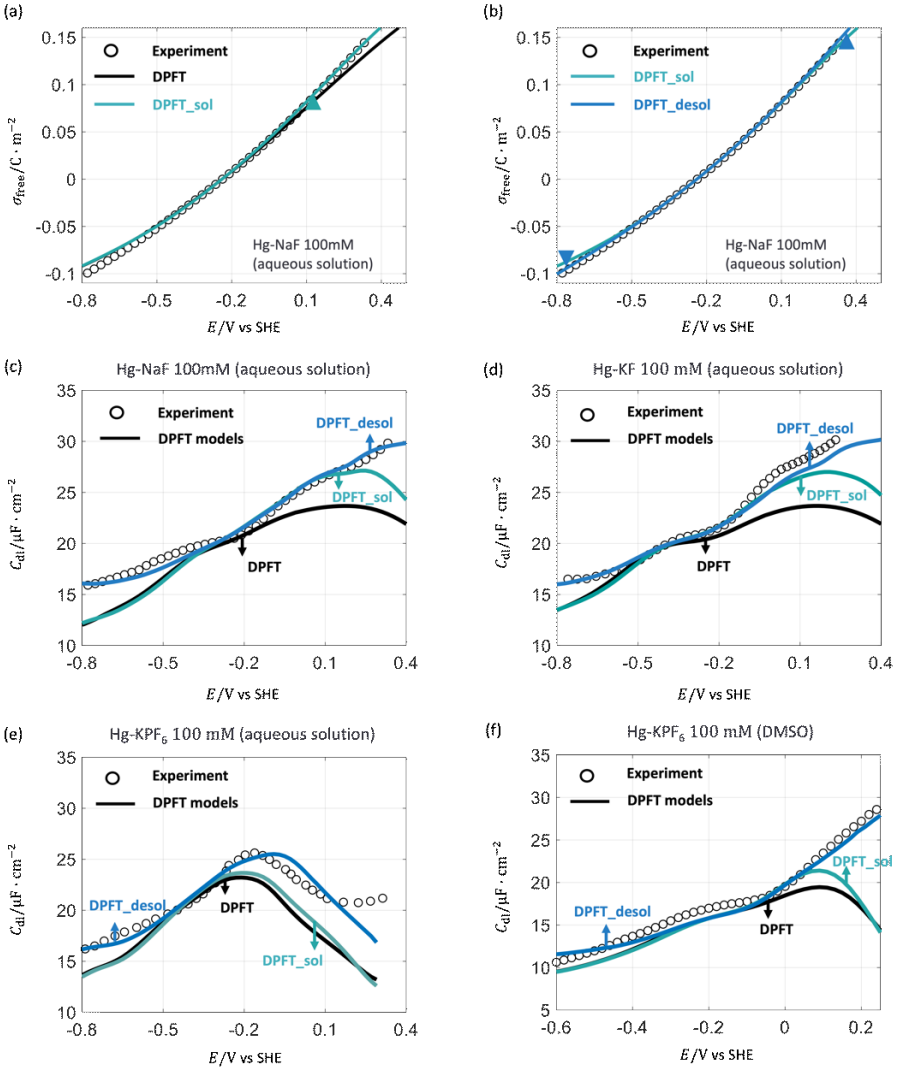

Figure 15. Comparison of σ_{free} (a, b) between experiment and DPFT models for the Hg-NaF aqueous solution interface at 100mM. Comparison of C_{dl} between the DPFT models and experimental results for (c) Hg-KF aqueous solution reported by Grahame et al[105], (d) Hg-KF aqueous solution reported by Schiffrin[115], (e) for Hg-KPF_6 aqueous solution reported by Parsons et al.[112], and (f) for Hg-KPF_6 DMSO solution reported by Payne et al.[116].

A two-dimensional diagram of the radius of the solvated ions, Na^+ and F^- at different locations in the EDL under different electrode potentials is provided in Figure 16.

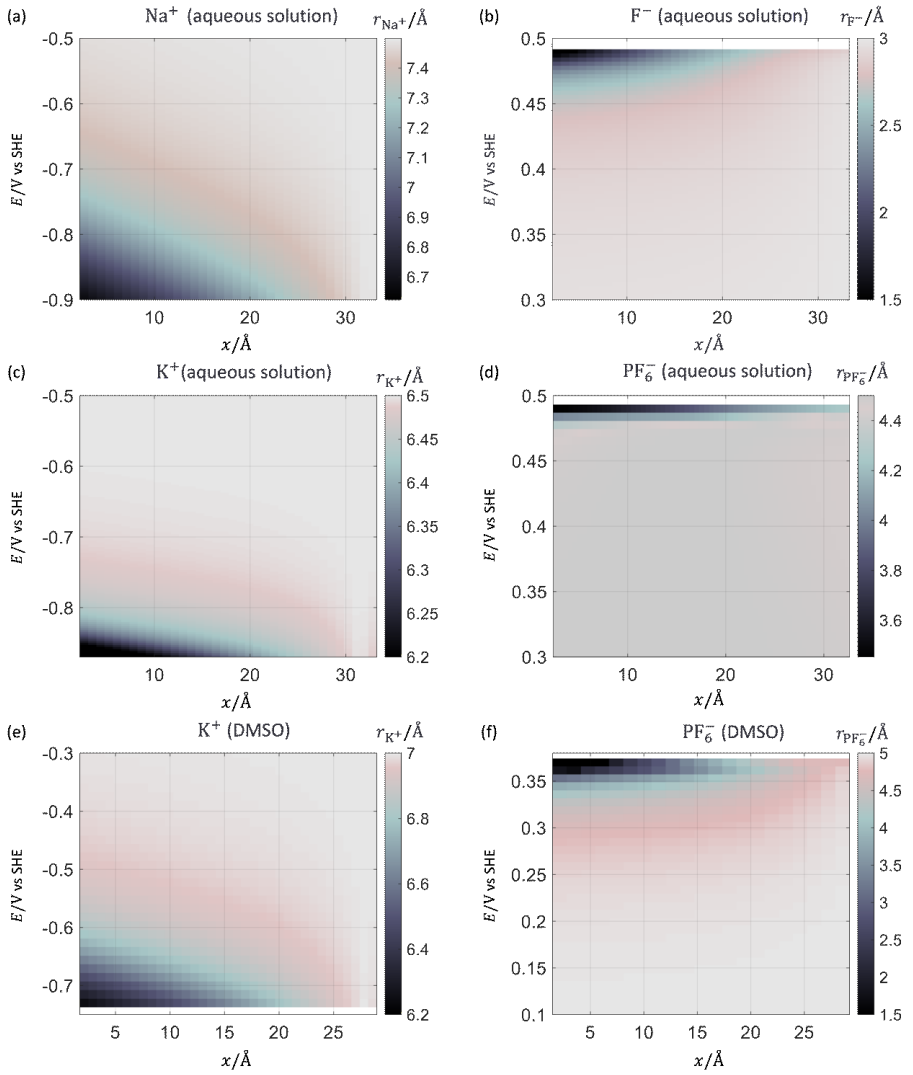

Figure 16. Ion desolvation as function of electrode potential in the DPFT_desol model. The distribution of the radii of solvated ion (a) $Na^+(H_2O)$, (b) $F^-(H_2O)$, (c) $K^+(H_2O)$, (d) $PF_6^-(H_2O)$, (e)

$K^+(DMSO)$, and (f) $PF_6^-(DMSO)$ from the metal surface to the solution bulk are as function of electrode potential. The electrode potential is referenced to the SHE scale.

Figure 17(d) plots the radii of solvated ions closest to the metal surface, namely, $r_{Na^+}^{1st}$ and $r_{F^-}^{1st}$, as a function of electrode potential. $r_{Na^+}^{1st}$ decreases at more negative electrode potentials relative to the PZC because of partial desolvation, as described in Eq.(78), while $r_{Na^+}^{1st}$ is equal to its value in the bulk solution above the PZC. We note that the change in $r_{Na^+}^{1st}$ above the PZC has little influence on C_{dl} because cations are repelled from the positively charged surface. Similarly, $r_{F^-}^{1st}$ decreases at more positive electrode potentials relative to the PZC and equals its bulk value at potentials negative of the PZC. Partial desolvation effects increase the density of counterions in the EDL, as shown in Figure 22(e, f), leading to an increase in C_{dl}. These insights are important to our understanding of the physical origins of the electrolyte effects on electrocatalytic reactions[134,145,146]. For example, Li *et al.* employed *in situ* surface-enhanced infrared adsorption spectroscopy to probe the local electric field, revealing that cation dehydration amplifies the local electric field and facilitates the HER at Pt electrodes[134]. A detailed analysis of electrolyte effects on the C_{dl} and their correlation with electrocatalytic reactions will be discussed in the final subsection.

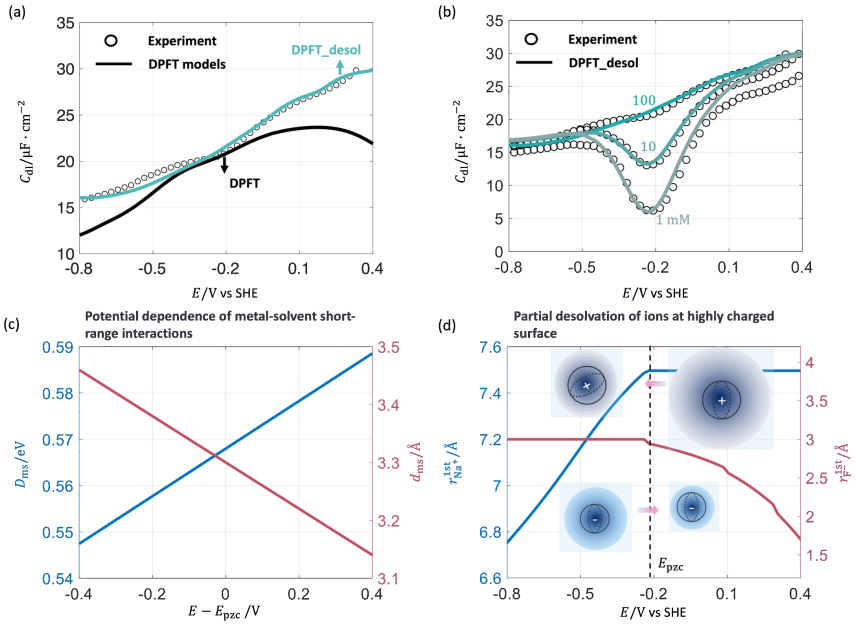

Figure 17. Improvement of the DPFT model by considering the potential-dependent short-range metal-solvent correlations in the DPFT_sol model and further considering the partial desolvation of ions in the DPFT_desol model. (a) Comparison of C_{dl} between experiment and the DPFT models at 100mM. (b) Comparison of C_{dl} between experiment and the DPFT_desol model at varying ion concentrations . The electrode potential is referenced to the SHE. (c) D_{ms}, d_{ms} change linearly with the electrode potentials with the fitting parameters $\alpha_{\mathrm{ms}} = 0.05, \beta_{\mathrm{ms}} = 0.40$. The electrode potentials are referenced to the PZC. (d) Radii of solvated ion Na^{+} and F^{-}, near the metal surface are as a function of the electrode potentials with fitting parameters $\zeta_{\mathrm{Na}^{+}} = 0.71, \zeta_{\mathrm{F}^{-}} = 1.11$.

Moreover, we conducted an additional analysis by testing an alternative model, DPFT_desol_only, where the potential-dependent solvent-metal interactions were omitted while retaining the potential-dependent partial desolvation of ions effect, with parameters refitted accordingly. The comparison of the DPFT_desol_only model with experimental data across varying ion concentrations is shown in Figure 18.

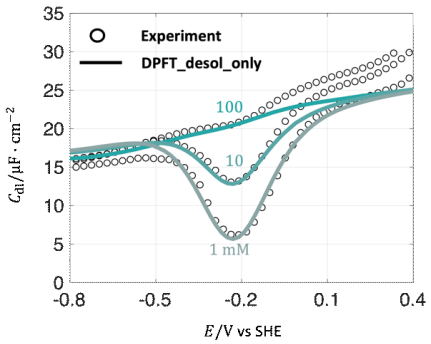

Figure 18. Comparison of $\mathrm{C_{dl}}$ between experimental results (circle) and DPFT_desol_only model results (solid line) in Hg-NaF aqueous solution at varying ion concentrations. The accordingly fitting parameter are $\alpha_{\mathrm{ms}} = 0, \beta_{\mathrm{ms}} = 0$ and $\zeta_{\mathrm{Na}^{+}} = 0.71, \zeta_{\mathrm{F}^{-}} = 11.1$. Other model parameters are the same with the DPFT_desol model.

The results indicate that while the DPFT_desol_only model captures the general trends, it exhibits a notably worse agreement in the positive potential region compared to the full DPFT_desol model. Therefore, we conclude that including the potential dependence of short-range metal-solvent interactions

is important for achieving quantitative agreement with experimental data, particularly at the positive potential region.

4.3. Refined microscopic pictures of the EDL from DPFT to DPFT_desol

The whole point of improving the fitting of C_{dl} lies in the rationale that a greater agreement with experimental C_{dl} – a lumped parameter – would lead us to a more accurate spatially resolved, microscopic picture of the EDL. Like all inverse interference of higher-dimensional unknowns from lower-dimensional knowns, errors may slip into the process. The so-inferred higher-dimensional unknowns require independent validations; in the present case, the deduced EDL structure needs to be ultimately validated by *operando* measurements of the spatially resolved properties of the EDL, like the electrostatic potential distribution[134,147,148], which is beyond the scope of this work.

To set a baseline, we first look at the spatial distribution of interfacial properties calculated by the DPFT model at different electrode potentials. As the key improvement in the DPFT model compared to the DPFT_pre lies in the description of solvent molecules, we first examine the densities of various types of solvent and permittivity distribution in Figure 20. When the electrode potential deviates from the PZC, the density of free solvent decays from the bulk to the metal surface due to the steric repulsion of counterions. In contrast, the change in the effective solvent density is smaller due to the compensation of solvent molecules in the solvation shell of cations as expressed in Eq.(73). The effective permittivity, $\epsilon_{\mathrm{s}}^{\mathrm{eff}}$, changes almost accordingly with the effective solvent density, as shown in Figure 20(c).

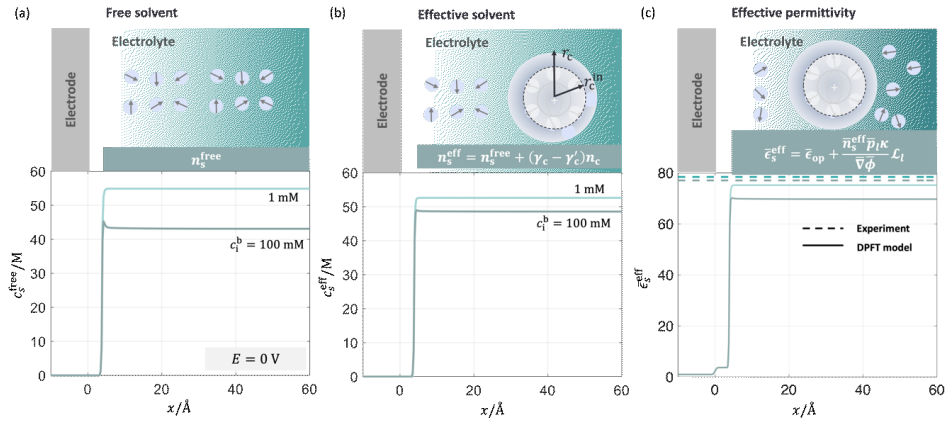

Figure 19. DPFT model results for the Hg-NaF aqueous interface at PZC. Concentration effect on the distribution of (a) free solvent density c_s^{free}, (b) effective solvent density c_s^{eff}, and (c) effective interfacial permittivity $\bar{\epsilon}_s^{eff}$ and experimental results are plotted in dashed line as the reference value[108], the value for 1mM and 100mM are 78.48 and 77.07, respectively. The position $x = 0$ denotes the metal edge.

A high ion concentration decreases n_s^{eff} and, accordingly, the permittivity. The effect of ion concentration on the solvent density and permittivity at the PZC is shown in Figure 19 and compared with the experimental results[108]. Additionally, n_s^{eff} near the metal electrode is significantly higher than the bulk value, which agrees with AIMD simulations reported in the literature[149].

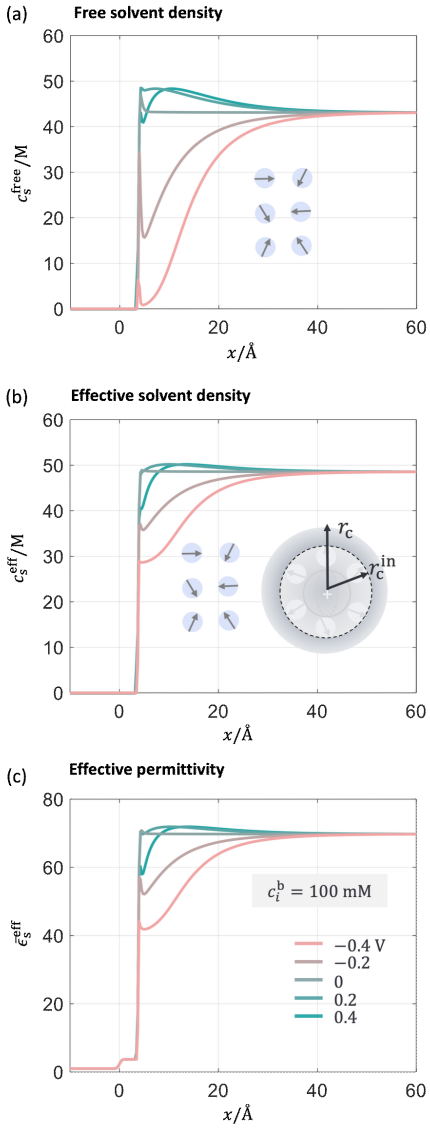

Figure 20. DPFT model results for Hg-NaF aqueous interface at 100mM at five electrode potentials. Distribution of (a) free solvent density and (b) effective solvent density. (c)

Distribution of the effective permittivity from the metal bulk to the solution bulk. The position $x = 0$ represents the metal edge and electrode potential is referenced to the PZC.

Other interfacial properties, including distribution of cation and anion density $n_{\mathrm{a(c)}}$, electron density n_{e}, and electrostatic potential ϕ are shown in Figure 21. As expected, when the metal electrode is negatively charged, cations are attracted to and anions repealed from the metal surface due to the long-range electrostatic interactions. The opposite occurs at a positively charged surface, as shown in Figure 21(a, b). These phenomena are already known from the classical GCS model[101,150,151]. The electron tail stretches out more at more negative electrode potentials, as shown in the inset of Figure 21(c, d), which are consistent with the calculation from the jellium model[152,153]. The electron density distribution, which is potential dependent and mediated by solvent properties, is important for understanding the electrolyte effects on PZC[154,155], as discussed in reference[77].

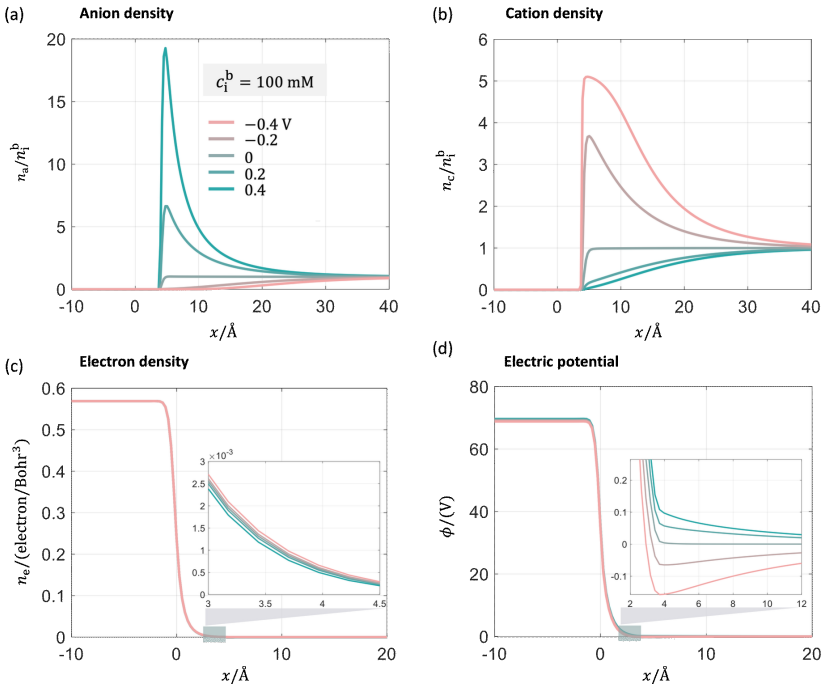

Figure 21. DPFT model results at 100mM at five electrode potentials. The distribution of (a) anion and (b) cation density normalized to their values in the solution bulk. The distribution

of (c) electron density n_e, (d) electrostatic potential ϕ. The position $x = 0$ represents the metal edge and the electrode potential is referenced to the PZC.

Figure 22(a) and (b) illustrate that the potential-dependent short-range metal-solvent interactions introduced in the DPFT_sol model make the free solvent density and effective permittivity in the diffuse layer (4-10 Å) smaller at the positive potentials. These interactions have a minimal effect in the negative potential region. As a result, the electrostatic potential curve on the solution side rises, as shown in the insert of Figure 22(c), attracting more anions toward the metal surface, as depicted in Figure 22(d). This increased anion density leads to an increase in σ_{free} and C_{dl} in the positive potential region. Further improvements are seen in the DPFT_desol model, which incorporates the partial desolvation of ions at a highly charged surface. This model accounts for the increased density of interfacial cations and anions due to the reducing size effects, as shown in Figure 22(e, f), leading to a pronounced increase of σ_{free} and C_{dl}.

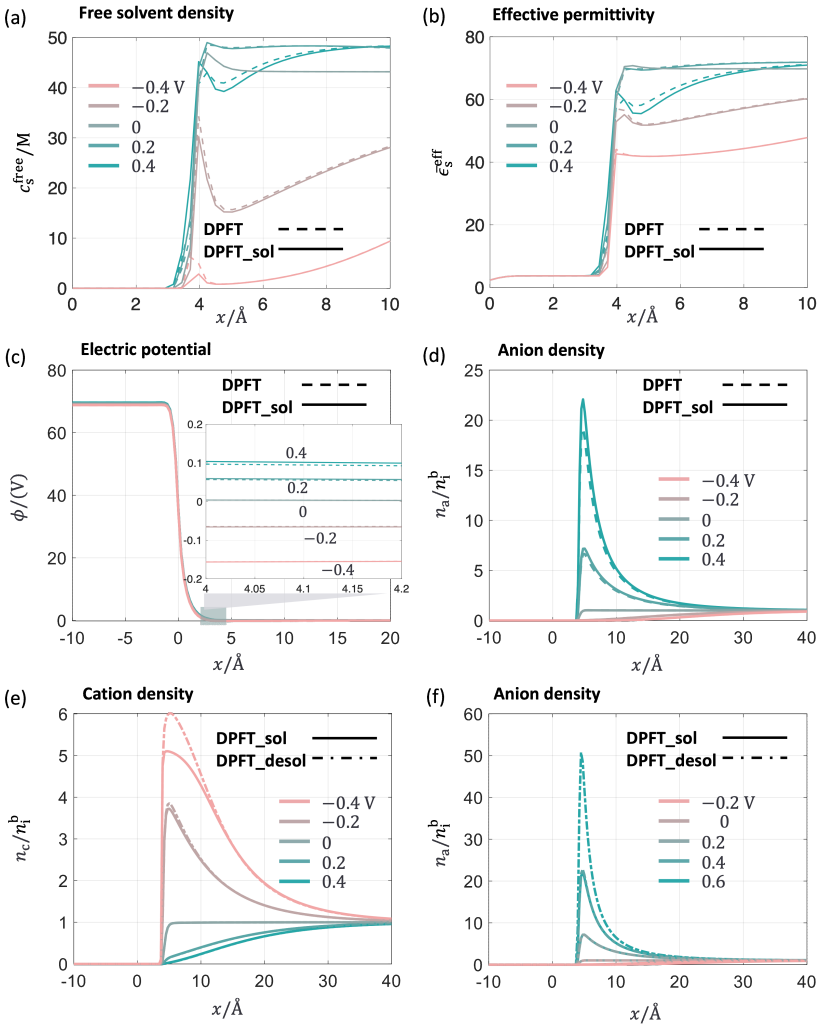

Figure 22. Interfacial structure of Mercury's EDL at a concentration of 100mM at five electrode potentials referenced to the PZC. Comparison of distribution of (a) free solvent density, (b) the effective permittivity, (c) electric potential ϕ and (d) anion density between the DPFT (dashed lines) and the DPFT_sol (solid lines) models. Comparison of distribution of (e) cation density and (f) anion density between the DPFT_sol (solid lines) and the DPFT_desol (solid-dot lines) model. The position $x = 0$ represents the metal edge.

4.4. Electrolyte effects on the EDL

In this section, we extend the modified DPFT model to various electrolyte compositions. Specifically, we compare the DPFT, DPFT_sol and DPFT_desol models with experimental C_{dl} curves for different electrolyte solutions containing various cations, anions, and solvent molecules. The model parameters are listed in **Table 3** and **Table 4**. When changing from one electrolyte to another, only a small set of parameters related to the electrolyte are varied, while other parameters remain unchanged. For instance, parameters describing the partial desolvation of ions are the same for the same ion in the same solvent.

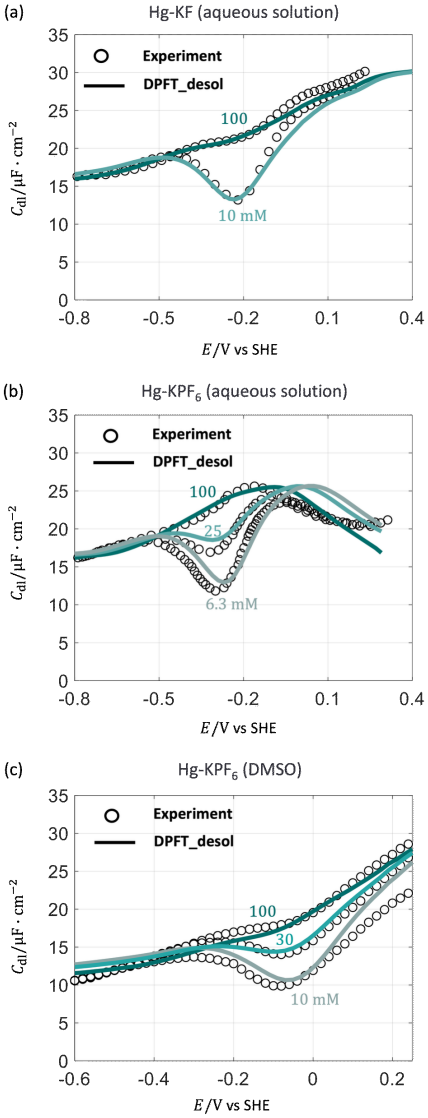

Figure 23. Extension of the improved DPFT model to different electrolyte compositions. Comparison of C_{dl} between the refined DPFT_desol model and experimental results for (a) Hg-KF aqueous solution reported by Schiffrin[115], (b) for Hg-KPF_6 aqueous solution reported by Parsons et al.[112], and (c) for Hg-KPF_6 DMSO solution reported by Payne et al.[116] at different ion

concentrations, respectively. Model parameters are provided in **Table 4**. The electrode potential is on the SHE scale.

As shown in Figure 15(d, e, f), the DPFT_desol model significantly improves the agreement with experimental data of C_{dl} for KF aqueous solution, KPF_6 aqueous solution, and KPF_6 in DMSO, respectively. For each of the three electrolyte solutions, a comparison between the DPFT_desol model and experimental data at different ion concentration effects is shown in Figure 23(a), (b), and (c), respectively. The decent agreement between the DPFT_desol model and experimental C_{dl} profiles across different electrolyte compositions lend credence to its effectiveness in describing the influence of electrolyte composition on the EDL of Mercury, which are detailed in the following.

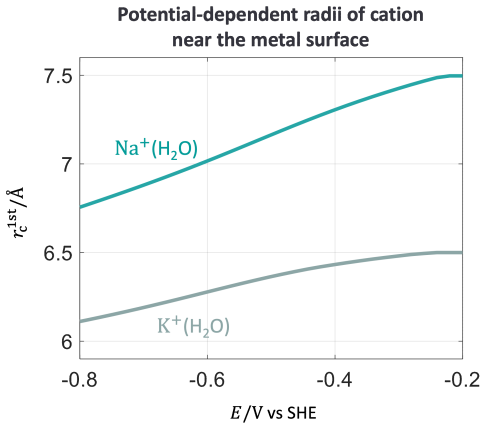

Figure 24. Effects of cations, Na^+ and K^+, on C_{dl}. Radii of solvated ions, $\mathrm{Na}^+(\mathrm{H_2O})$ and $\mathrm{K}^+(\mathrm{H_2O})$, near the metal surface as a function of electrode potentials. The calibrated parameters are $\zeta_{\mathrm{Na}^+} = 0.71$ and $\zeta_{\mathrm{K}^+} = 0.34$. Other parameters are provided in the SI. The solid point represents the PZC. The electrode potential is on the SHE scale.

The experimental C_{dl} curves for different cations, Na^+ and K^+, are compared with the DPFT_desol model at a concentration of 100mM in Figure 25(a). Though Na^+ has a larger solvated size than K^+[117], the C_{dl} curves in the negative potential region nearly overlap. This anomalous cation effect is captured by the DPFT_desol model, which accounts for cations undergoing different degrees of partial desolvation. Figure 24 shows the radii of solvated cations, Na^+ and K^+, near the metal surface as a function of the electrode potential, described by Eq. (78) with fitting parameters $\zeta_{\mathrm{Na}^+} = 0.71$ and $\zeta_{\mathrm{K}^+} = 0.34$. In comparison,

solvated Na^+ undergoes a greater degree of desolvation than K^+ near the metal surface which could be attributed to the stronger polarization effect of Na^+ towards water molecules of the solvation shell of a neighboring Na^+. This phenomenon can be validated using *in-situ* surface-enhanced infrared adsorption spectroscopy[134].

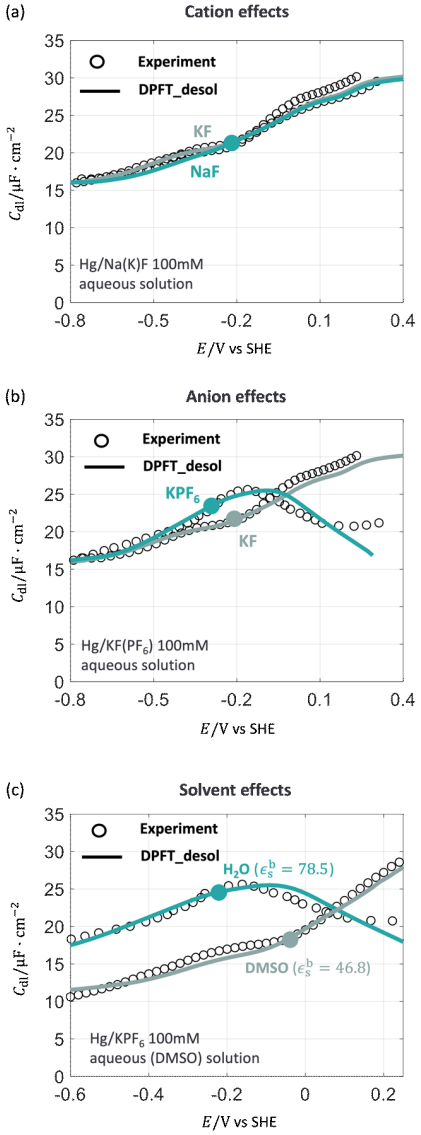

Figure 25. Comparison of C_{dl} between experimental results and the DPFT_desol model at a concentration of 100mM. (a) Effects of cations, Na^+ and K^+, on C_{dl}, (b) Effects of anions, PF_6^- and F^-, on C_{dl}, (c) Effects of solvent molecules, water and DMSO, on C_{dl}.

Next, we analyze the experimental C_{dl} curves for different anions, F^- and PF_6^-, which are fitted with the DPFT_desol model in Figure 25(b). The effect of anions on the PZC is already captured in the DPFT model, as shown in Figure 26(a), with fitting parameters $d_{\mathrm{mF}^-} = 4$ Å and $d_{\mathrm{mPF}_6^-} = 3.2$ Å, respectively. These parameters suggest that the short-range metal-anion interactions may be stronger for PF_6^- than F^-, potentially causing the PZC to shift to a more negative value[74,77]($E_{\mathrm{pzc}} = -0.30\ \mathrm{V_{SHE}}$). Sundararaman *et al.*[144] have calculated the metal-anion interactions for F^- on Ag (111), while a comparative calculation of PF_6^- and F^- on mercury electrodes is missing.

The influence of anions on the shape of C_{dl} can be understood through the variable radii of solvated anions. As depicted in Figure 26(b), the radii of solvated anions, F^- and PF_6^-, near the metal surface change with the electrode potential, described by Eq. (78) with fitting parameters $\zeta_{\mathrm{F}^-} = 1.11$ and $\zeta_{\mathrm{PF}_6^-} = 0.05$, respectively. The DPFT_desol model analysis suggests that F^- undergoes a greater degree of desolvation than PF_6^- at positive potentials. Nevertheless, r_{F^-} remains smaller than $r_{\mathrm{PF}_6^-}$, resulting in an earlier capacitance peak for PF_6^-.

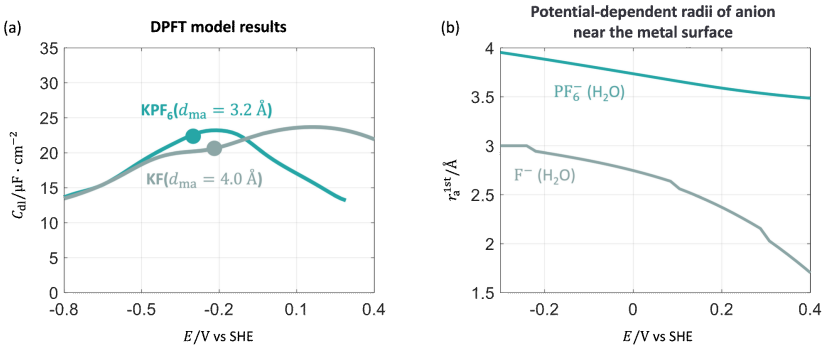

Figure 26. Effects of anions, PF_6^- and F^-, on C_{dl}. (a) C_{dl} results obtained from the DPFT model. (b) Radii of solvated ions, $\mathrm{F}^-(\mathrm{H_2O})$ and $\mathrm{PF}_6^-(\mathrm{H_2O})$, near the metal surface as a function of electrode potentials. The calibration parameters are $d_{\mathrm{mF}^-} = 4$ Å, $d_{\mathrm{mPF}_6^-} = 3.2$ Å, $\zeta_{\mathrm{F}^-} = 1.11$ and $\zeta_{\mathrm{PF}_6^-} = 0.05$. Other parameters are provided in the SI. The solid point represents the PZC. The electrode potential is on the SHE scale.

Finally, we study the solvent effects on the experimental C_{dl} curves, specifically, by comparing water and DMSO. In both solvents, $\mathrm{KPF_6}$ is used as the salt. The results calculated with the DPFT_desol model are presented in Figure 25(c). As regards DMSO, its lower bulk and optical permittivity, along with a smaller

metal-solvent equilibrium distance, shift the PZC positively ($E_{\mathrm{pzc}} = -0.05\ \mathrm{V_{SHE}}$), as shown in the DPFT model in Figure 27(a). The fitting parameters are $\bar{\epsilon}_{\mathrm{op}}^{\mathrm{H_2O}} = 3.70$, $d_{\mathrm{mH_2O}}^{0} = 3.3\ \text{Å}$ and $\bar{\epsilon}_{\mathrm{op}}^{\mathrm{DMSO}} = 2.74$, $d_{\mathrm{mDMSO}}^{0} = 2.8\ \text{Å}$, respectively. The solvent effects on the PZC have been discussed in detail in a previous study[77].

The effects of solvent molecules on the shape of C_{dl} are analyzed by examining the intefacial radii of solvated ions, as shown in Figure 27(b) and (c). Figure 27(b) presents the interfacial radii of solvated $\mathrm{K^+}$ in water and DMSO as a function of electrode potential. These radii are described by Eq. (78) with fitting parameters $\zeta_{\mathrm{K^+}}^{\mathrm{H_2O}} = 0.34$ and $\zeta_{\mathrm{K^+}}^{\mathrm{DMSO}} = 0.35$, respectively, indicating that solvated $\mathrm{K^+}$ undergoes a greater degree of desolvation in DMSO at negative potentials compared to water. Furthermore, $r_{\mathrm{K^+}}^{\mathrm{H_2O}}$ remains smaller than $r_{\mathrm{K^+}}^{\mathrm{DMSO}}$, resulting in a higher C_{dl} profile for water compared to DMSO at negative potentials. Similarly, Figure 27 (c) shows the interfacail radii of solvated $\mathrm{PF_6^-}$ in water and DMSO as a function of electrode potential. These radii are described by Eq. (78) with $\zeta_{\mathrm{PF_6^-}}^{\mathrm{H_2O}} = 0.05$ and $\zeta_{\mathrm{PF_6^-}}^{\mathrm{DMSO}} = 2.35$, respectively, showing that solvated $\mathrm{PF_6^-}$ undergoes greater desolvation in DMSO at positive potentials compared to water. Initially, $r_{\mathrm{PF_6^-}}^{\mathrm{H_2O}}$ is smaller than $r_{\mathrm{PF_6^-}}^{\mathrm{DMSO}}$; however, as the potential increases, this trend reverses, causing C_{dl} profile in water to be higher initially but lower than that in DMSO at higher potentials. These desolvation behaviors may be attributed to the higher solvation energy of ions in aqueous solution compared to organic solvent, as discussed in prior studies[154,155].

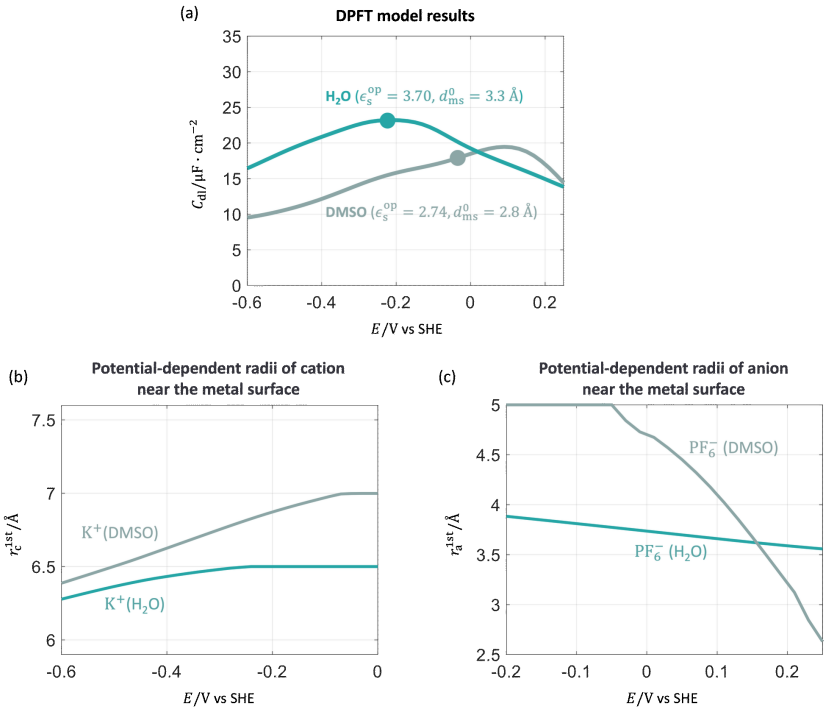

Figure 27. Effects of solvent molecules, water and DMSO, on C_{dl}. (a) C_{dl} results obtained from the DPFT model. (b) Radii of solvated cations, $\mathrm{K^+(H_2O)}$ and $\mathrm{K^+(DMSO)}$, near the metal surface as a function of electrode potentials. (c) Radii of solvated anions, $\mathrm{PF_6^-(H_2O)}$ and $\mathrm{PF_6^-(DMSO)}$, near the metal surface as a function of electrode potentials. The calibration parameters are $\bar{\epsilon}_{\mathrm{op}}^{\mathrm{DMSO}} = 2.74$, $d_{\mathrm{mDMSO}}^0 = 2.8$ Å, $\alpha_{\mathrm{mDMSO}} = 0.05$, $\beta_{\mathrm{mDMSO}} = 0.15$, $\zeta_{\mathrm{K^+}}^{\mathrm{H_2O}} = 0.34$, $\zeta_{\mathrm{K^+}}^{\mathrm{DMSO}} = 0.35$, $\zeta_{\mathrm{PF_6^-}}^{\mathrm{H_2O}} = 0.05$ and $\zeta_{\mathrm{PF_6^-}}^{\mathrm{DMSO}} = 2.35$. Other parameters are provided in the SI. The solid point represents the PZC. The electrode potential is on the SHE scale.

4.5. Summary

In this chapter, the EDL at mercury-solution interfaces is systematically investigated under highly charged conditions, with a focus on identifying the physical mechanisms required to reproduce experimentally observed C_{dl} profiles.

Comparisons between the DPFT_desol model and experimental C_{dl} profiles reveal the importance of potential-dependent short-range metal-water interactions in accurately predicting the upward-tilted C_{dl} profiles observed experimentally. Additionally, accounting for the partial desolvation of ions significantly improves the model's alignment with experimental data, particularly at highly charged states.

The DPFT_desol model is further extended to various electrolyte compositions, successfully reproducing experimental C_{dl} profiles for different cations, anions, and solvent molecules. This highlights the robustness and generality of the DPFT approach. Detailed analysis of electrolyte effects on C_{dl} provides valuable insights that could be informative to understand the EDL at copper and other highly charged electrodes used in critical electrocatalytic reactions, such as CO_2 reduction reactions.

Chapter 5. Potential of zero stress of solid-liquid interfaces

*Reproduced with minor changes from '**Zhang Z**, Chen H*, Huang J*, Potential of Zero Stress of Solid-Liquid Interfaces. In preparation'.*

5.1. Introduction

The mechanical response of electrified solid-liquid interfaces plays a critical role in surface stability, reconstruction, and long-term durability of electrochemical systems. Unlike liquid metal electrodes, whose interfacial behavior is governed by surface tension[33–37], solid electrodes exhibit elastic resistance to deformation, making surface stress the fundamental thermodynamic quantity. Under electrochemical conditions, surface stress is strongly coupled to electronic structure and EDL formation, yet its potential dependence and sensitivity to electrolyte composition remain poorly understood due to the lack of thermodynamically consistent constant-potential models[41–44,12,8].

Building on the theoretical framework established in **Chapter 3**, this chapter investigates surface stress at electrified solid metal-solution interfaces using a semiclassical DPFT approach. Key interfacial thermodynamic quantities—including the C_{dl}, surface tension γ_{st}, interfacial free energy, F_{int}, elastic strain ϵ and surface stress g_{ss} —have been defined previously and are applied here to establish a consistent description of electro-mechanical coupling under constant-potential conditions.

The surface stress g has been measured under electrochemical conditions using the Gokhshtein method by Valincius[100], the cantilever bending method by Ibach et al.[11], and the dilatometry method by Weissmuller et al.[156] Kramer summarized the potential dependence of g reported on various polycrystalline electrodes, most of them gold and platinum[99]. Both parabolic and monotonic $g(E)$ curves have been reported, even at the same electrode. The discrepancy in literature signals a limited understanding of interfacial parameters determining $g(E)$. Kramer presented a conceptual analysis of $g(E)$, considering both specific adsorption of ions described with a parameter k and strain dependence of the potential of zero charge (PZC) described with a parameter η. The parabolic and monotonic $g(E)$ curves then can be rationalized with varying k and η. However, fundamental microscopic origins of these parameters are unknown. Specifically, it remains largely elusive how the spillout of metal electrons and short-range interactions between metal, ions and water influence Kramer's parameters, as depicted in Figure 32(a). Schmickler and Levia[12] investigated the influence of electron spillout using the jellium model.

Their analysis highlighted the importance of electronic structure effects at the metal surface but did not explicitly address the constant potential conditions required to evaluate g from the strain dependence of γ, using Eq.(39).

In this Chapter, we employ a *constant-potential*, density-potential functional theory (DPFT) approach to calculate the potential dependence of the surface stress on ideally polarizable electrodes, namely without specific adsorption of ions. The DPFT approach is suitable for correlating the $g(E)$ behavior with electron spillout phenomenon and short-range interactions at the interface, for it integrates an orbital-free density functional theory (DFT) of metal electrons and a statistical field theory of the electrolyte solution into a grand-canonical framework[74,157]. Water adsorption at metal surface is revealed to determine the $g(E)$ behavior; monotonically increasing, monotonically decreasing, and nonmonotonic behaviors can be obtained with different dependencies of water adsorption on the electrostatic strain. Potential of zero stress (PZS), if exists, is defined as a characteristic potential of the $g(E)$ relation. The relationship between PZS and PZC is discussed.

5.2. Surface tension, surface stress and potential of zero stress

5.2.1. Calibrating the models using experimental $C_{\mathbf{dl}}$

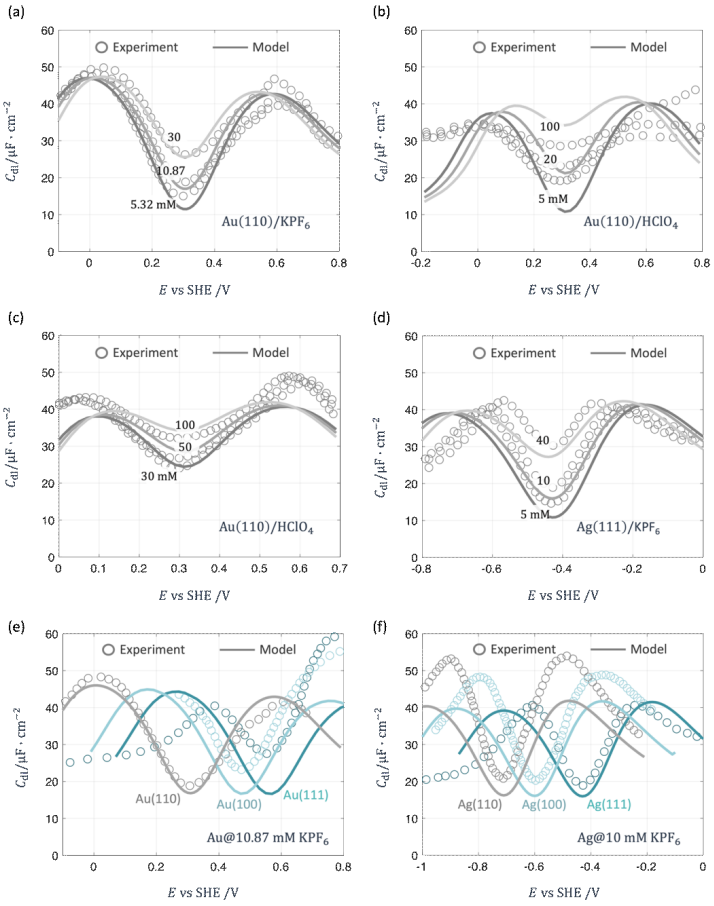

Figure 28. Calibration of the DPFT model (solid lines) with experimental C_{dl} data (circles). Comparison of C_{dl} between the model and experiment in (a) $\mathrm{Au(110)/KPF_6}$ measured by Hamelin et. al.,[80] (b, c) $\mathrm{Au(110)/HClO_4}$ measured by Samec, et. al.,[81] and Hamelin et. al.,[158] respectively, and (d) $\mathrm{Ag(111)/KPF_6}$ measured by Valette, et. al.,[85]. (e) $\mathrm{Au(111,100,110)/KPF_6}$ measured by Hamelin et. al.,[80] and (f) (e) $\mathrm{Ag(111,100,110)/KPF_6}$ measured by Valette, et. al.[83–85]. Calibrated parameters are $v_{\mathrm{cc}}^{0,\mathrm{Au(110)}} = -0.549$ eV, $d_{\mathrm{mK^+(PF_6^-)}}^{\mathrm{Au}} = 1.8$ Å, $d_{\mathrm{mH^+(ClO_4^-)}}^{\mathrm{Au}} = 2.8$ Å , and $v_{\mathrm{cc}}^{0,\mathrm{Ag(111)}} = -0.394$ eV, $d_{\mathrm{mK^+}}^{\mathrm{Ag}} = 4.8$ Å, $d_{\mathrm{mPF_6^-}}^{\mathrm{Ag}} = 1.8$ Å . $v_{\mathrm{cc}}^{0,\mathrm{Au(111)}} = -0.572$ eV , $v_{\mathrm{cc}}^{0,\mathrm{Au(100)}} = -0.564$ eV and $v_{\mathrm{cc}}^{0,\mathrm{Ag(100)}} = -0.363$ eV, $v_{\mathrm{cc}}^{0,\mathrm{Ag(110)}} = -0.343$ eV. The electrode potential is on the SHE scales.

We begin by calibrating the DPFT model using experimental C_{dl} data. A comparison of C_{dl} between model and experiment is plotted in Figure 28. Experimental data of $\mathrm{Au/KPF_6}$ are measured by Hamelin et. al.,[80] $\mathrm{Au(110)/HClO_4}$ by Samec, et. al.,[81] and Hamelin et. al.,[158] and $\mathrm{Ag/KPF_6}$ by Valette, et. al.,[83–85]. The calibrated parameters for $\mathrm{Au(110)}$ include $v_{\mathrm{cc}}^{0,\mathrm{Au(110)}} = -0.549$ eV, $d_{\mathrm{mK^+(PF_6^-)}}^{\mathrm{Au}} = 1.8$ Å, $d_{\mathrm{mH^+(ClO_4^-)}}^{\mathrm{Au}} = 2.8$ Å. For $\mathrm{Ag(111)/KPF_6}$ system, the calibrated parameters are $v_{\mathrm{cc}}^{0,\mathrm{Ag(111)}} = -0.394$ eV, $d_{\mathrm{mK^+}}^{\mathrm{Ag}} = 4.8$ Å, $d_{\mathrm{mPF_6^-}}^{\mathrm{Ag}} = 1.8$ Å. A full list of model parameters is provided in **Table 1-3**.

The model-based C_{dl} agrees reasonably well with experiments across different electrolyte compositions and electrodes. For the $\mathrm{Au(110)}$ electrode, the use of $\mathrm{HClO_4}$ solution, which exhibits weaker metal-ion short-range interactions than $\mathrm{KPF_6}$, reduces the peak of C_{dl} on both the cathodic and anodic sides, consistent with trends reported in our recent works[76,77]. Furthermore, for the same electrolyte solution, $\mathrm{KPF_6}$, the metal-cation short-range interactions are weaker on $\mathrm{Ag(111)}$ than on $\mathrm{Au(110)}$. This may be attributed to the fact that $\mathrm{Ag(111)}$ exhibits stronger hydrophilicity[159,160], attracting more water molecules to the metal surface and weakening metal-cation interactions. In addition, different crystal facets of the metal electrode exhibit different potential of zero free charges (PZFCs), as shown in Figure 28(e) for Au and Figure 28(f) for Ag electrodes. According to experimental data by Hamelin et. al.[80], the measured E_{pzfc} for Au(111), Au(100) and Au(110) in $10.87\mathrm{mM}$ $\mathrm{KPF_6}$ aqueous solution are 0.55 $\mathrm{V_{SHE}}$, 0.46 $\mathrm{V_{SHE}}$, 0.30 $\mathrm{V_{SHE}}$, respectively. In experiments by Valette, et. al.[83–85], the measured E_{pzfc} for Ag(111), Ag(100) and Ag(110) in $10\mathrm{mM}$ $\mathrm{KPF_6}$ aqueous solution are -0.43 $\mathrm{V_{SHE}}$, -0.60 $\mathrm{V_{SHE}}$, -0.71 $\mathrm{V_{SHE}}$, respectively. To align our model with these observations, we adjust the pseudopotential parameter, v_{cc}^0, while keeping other parameters the same. The calibrated parameters for another two crystal Au and Ag facets are $v_{\mathrm{cc}}^{0,\mathrm{Au(111)}} = -0.572$ eV, $v_{\mathrm{cc}}^{0,\mathrm{Au(100)}} = -0.564$ eV and $v_{\mathrm{cc}}^{0,\mathrm{Ag(100)}} = -0.363$ eV, $v_{\mathrm{cc}}^{0,\mathrm{Ag(110)}} = -0.343$ eV, respectively. The more positive PZFC for the (111) facet correlates with its higher work function, which is captured in this model using a more negative v_{cc}^0. The observed discrepancies between model-based and experimental C_{dl} may arise from the orientation-dependent adsorption free energy of water[24] or ion partial desolvation at highly charged surfaces[76], which are not explicitly accounted for in the current model. To the best of our knowledge, these experimental C_{dl} data are systematically analyzed within a single modeling framework for the first time. While the present DPFT framework successfully captures the C_{dl} behavior of noble metal electrodes, its current formulation is developed for metallic electrodes, where the electronic density of states (DOS) near the Fermi level is relatively smooth and leads to a monotonic dependence of electronic charge on electrode potential. In contrast, many carbon-based materials, such as graphene, exhibit a V-shaped DOS with a Dirac point, which can produce a non-monotonic charge

response and a qualitatively different quantum capacitance behavior[161–163]. Capturing such effects would require incorporating an explicit description of the material-specific DOS into the electronic free-energy functional. While this aspect is not included in the current model, the DPFT framework could be extended in this direction, which may enable its application to carbonaceous and other non-metallic electrodes.

5.2.2. Equivalence of surface tension and interfacial free energy

Secondly, the excess surface charge is the free surface charge, denoted σ_{free}, which is obtained from integrating the differential double-layer capacitance C_{dl} with respect to E. Figure 32(b) compares experimental and calculated σ_{free} for the case of Au(110) in contact with aqueous KPF_6 solution at different concentrations. The surface tension, γ_{st}, is then obtained by the integral of σ_{free} over the electrode potential up to a constant at the PZC, see Eq.(110). The excess volumetric grand-canonical potential density, G_{exe}, is independently calculated by spatial integration of grand-canonical potential in one dimension, as described in Eq.(111). Figure 29 shows excellent agreement is obtained between $\Delta\gamma_{\mathrm{st}}$ and ΔG_{exe} for both $\mathrm{Au}(110)$ and $\mathrm{Ag}(111)$ electrodes, confirming the thermodynamic consistency and numerical accuracy of the DPFT model. The small discrepancies are attributed to numerical processing techniques employed in the DPFT implementation to ensure stability and convergence, as discussed in the Supporting Information of ref.[74]. The surface tension profiles exhibit a parabolic shape with a maximum value at the PZC in the absence of specific adsorption. This behavior aligns well with classical electrocapillary experimental results[37].

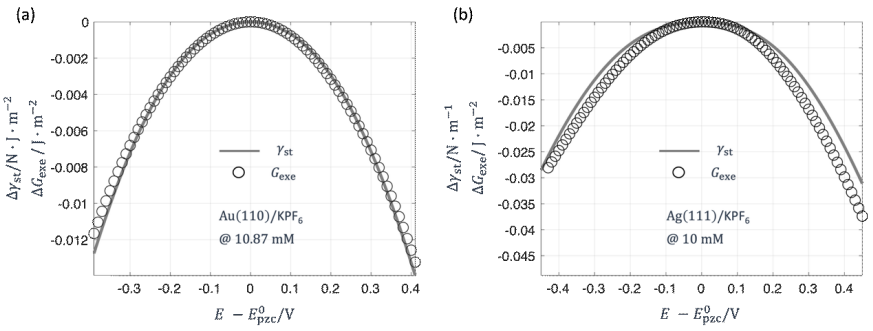

Figure 29. Comparison of two methods for calculating surface tension. Relative surface tension (solid line) and relative excess grand-canonical potential density (circle) of solid metal-solution interfaces

referred to the values at the PZC for (a) $\mathrm{Au}(110)$@$10.87\ \mathrm{mM\ KPF_6}$ and (b) $\mathrm{Ag}(111)$@$10\ \mathrm{mM\ KPF_6}$ aqueous solution. The electrode potential is referenced to the E^0_{pzc}.

5.2.3. Surface stress

Taking the $\mathrm{Au}(110)$@$10.87\ \mathrm{mM\ KPF_6}$ as a representative example, we examine the effect of elastic strain on the surface tension $\gamma(E)$ [see Figure 32(c)]. The applied strain, $\Delta\epsilon = \pm 0.01$, lies within the experimentally observed range[156,164]. The negative value of γ indicates that formation of the solid-liquid interface lowers the total free energy of the system. At $\Delta\epsilon = 0.01$, the parabolic $\gamma(E)$ profile shifts downward and toward more positive potentials. This shift originates from the strain-induced reduction of the charge density of metallic cores, which lowers the electronic chemical potential and consequently shifts the PZC to more positive values[74]. The corresponding shifts of the σ_{free} and C_{dl} curves are shown in Figure 30.

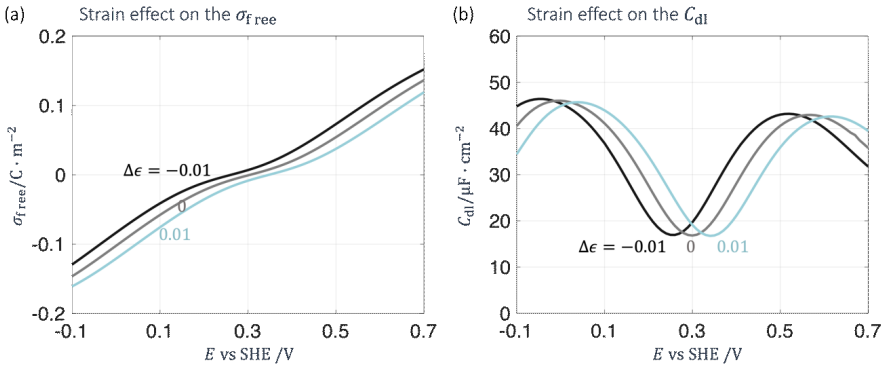

Figure 30. Strain effect on the (a) σ_{free} and (b) C_{dl} for $\mathrm{Au}(110)$@$10.87\ \mathrm{mM\ KPF_6}$.

The surface stress $g_{\mathrm{cp}}(E)$ is evaluated via the Eq.(39) where the subscript 'cp' represents the *constant potential* condition and the argument *E* refers to the potential dependence. As shown in Figure 32(d), the $g_{\mathrm{cp}}(E)$ monotonically increases with electrode potential, in contrasts to the parabolic electrocapillary behavior of the surface tension[37]. To emphasize the importance of *constant potential* condition in Eq.(39), we also calculate the surface stress under *constant charge* conditions, following the work of Schmickler and Levia[12], according to,

$$g_{\mathrm{cc}}(E) = \gamma + \left(\frac{\partial \gamma}{\partial \epsilon}\right)_{T,\mu_i,\sigma}. \tag{114}$$

with $\gamma(\epsilon)$ at given σ provided in Figure 33. In sharp contrast, g_{cc} exhibits parabolic-like potential dependence, as shown in Figure 32(d). It should be noted that Eq.(114) does not reconcile with the electrocapillarity of solid-liquid interfaces[98], while Eq.(39) does. This comparison highlights the importance of using the correct electrochemical ensemble in calculating the surface stress, which may explain the various behaviors of surface stress reported in the literature. Unless otherwise noted, g refers to g_{cp} in the remainder of this paper.

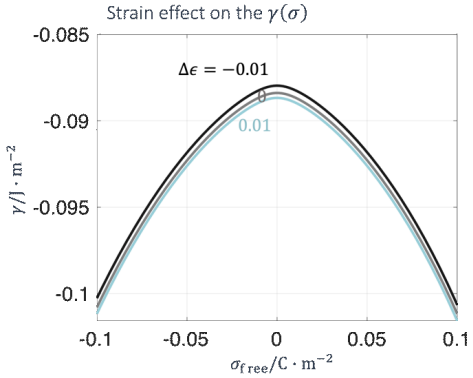

Figure 31. Strain effect on the $\gamma(\sigma)$ under *constant charge* conditions for $\mathrm{Au}(110)$@$10.87\ \mathrm{mM}\ \mathrm{KPF}_6$.

Following the convention, a positive value of g indicates tensile surface stress (surface intends to contract), while a negative value indicates compressive surface stress (surface intends to expand) [54,43,46]. A characteristic electrode potential at which the surface stress itself vanishes, referred to the potential of zero surface stress (PZS), E_{pzs}, is observed in Figure 32(d). Previous studies, notably the estance measurements of Valincius et al.[100] and the theoretical analysis of Kramer[99], primarily focused on potentials at which the derivative of the surface stress with respect to potential vanishes, $\frac{\partial g}{\partial E} = 0$, corresponding to the extrema of electrocapillary or estance curves. Such "zero-estance" potentials characterize changes in the slope of $g(E)$ and may occur at multiple values depending on the electrolyte composition, adsorption, and elastic contributions, but they do not imply mechanical neutrality of the interface. By contrast, the PZS, which is, to the best of our knowledge, defined here for the first time, identifies the potential at which the $g(E)$ changes sign, marking the transition between compressive and

tensile regimes. Interestingly, the PZS and the PZC are different. For the present case, we find $E_{\mathrm{pzs}} = 0.45\ \mathrm{V_{SHE}}$, which is more positive than the unstrained PZC ($E^{0}_{\mathrm{pzc}} = 0.3\ \mathrm{V_{SHE}}$), a point we shall return back to later.

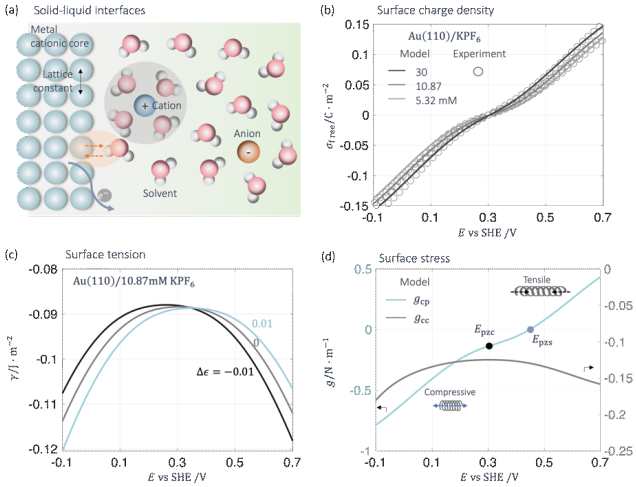

Figure 32. Surface stress of electrified solid metal-solution interfaces. (a) Schematic diagram of solid-liquid interfaces where the spillout of metal electrons and short-range interactions between metal and water are highlighted. (b) Comparison of σ_{free} between the DPFT model and experiment at different concentrations reported by Hamelin et. al.[80]. (c) Elastic strain effect on the surface tension $\gamma(E)$. (d) Comparison between $g_{\mathrm{cp}}(E)$ and $g_{\mathrm{cc}}(E)$. Results of (c-d) are shown for $\mathrm{Au(110)@10.87mM\ KPF_6}$ aqueous solution. The unstrained PZC is $E^{0}_{\mathrm{pzc}} = 0.3\ \mathrm{V_{SHE}}$.

5.5.4. Influence of water adsorption

As discussion in **Chapter 2**, the potential dependence of surface stress arises from two competing contributions: capacitive charging of the metal surface and the strain dependence of the PZC. Within this framework, the key quantity governing stress trends is therefore the strain derivative of the PZC, $\frac{\partial E_{\mathrm{pzc}}}{\partial \epsilon}$, which determines whether surface stress varies monotonically with potential or exhibits extrema (see Figure 7).

Previous studies have revealed that the PZC is highly sensitive to water adsorption on the metal surface [165,142,166–168]. In absence of chemisorption of water molecules which is largely the case for Au and Ag

electrodes considered here, the key parameter is the metal-water separation. In the DPFT model, the metal-water short-range interactions are described using a Morse potential. As a first approximation, we assume a linear relation between the equilibrium metal-water distance and surface strain,

$$d_{\mathrm{ms}} = d_{\mathrm{ms}}^{0} - \beta_{\mathrm{s}}\Delta\epsilon. \tag{115}$$

where d_{ms}^{0} denotes the equilibrium metal-water distance in the absence of strain, and β_{s} is a coefficient (in units of Bohr radius a_0) characterizing the strength of strain-dependence of d_{ms}. A more positive β_{s} means that interfacial water molecules approach closer to the metal surface under tensile strain.

Figure 33(a) shows that the differential capacitance C_{dl} profile shifts, almost horizontally, toward more negative potentials at more positive β_{s}, while the overall magnitude and shape of the C_{dl} remain largely unchanged. The corresponding strain-induced shifts of the PZC are presented in Figure 33(b). In the absence of strain-dependent MWSRI ($\beta_{\mathrm{s}} = 0$), the PZC exhibits the largest positive shift under tensile strain, with the derivative $\frac{\partial E_{\mathrm{pzc}}}{\partial \epsilon} \approx 4.30\ \mathrm{V}$, as discussed in Figure 32. As β_{s} becomes more positive, the strain-induced PZC shifts is progressively reduced: $\frac{\partial E_{\mathrm{pzc}}}{\partial \epsilon}$ decreases to $1.85\ \mathrm{V}$ at $\beta_{\mathrm{s}} = 5a_0$, and turns negative ($-0.96\ \mathrm{V}$) at $\beta_{\mathrm{s}} = 10a_0$, and further decreases to $-3.38\ \mathrm{V}$ at $\beta_{\mathrm{s}} = 15a_0$. This trend is rationalized with the enhanced dielectric response of interfacial water at shorter equilibrium metal-water distance, which drives the PZC toward more negative potentials[77].

The resulting changes of surfaces stress are shown in Figure 33(c). For the case of $\beta_{\mathrm{s}} = 0 \text{ and } 5a_0$, the surface stress increases monotonically with electrode potential, leading to a positive PZS relative to PZC. At intermediate strain-dependence of d_{ms} ($\beta_{\mathrm{s}} = 10a_0$), the surface stress exhibits a nonmonotonic, parabolic-like dependence on electrode potential. In contrast, for strong strain-dependence of d_{ms} ($\beta_{\mathrm{s}} = 15a_0$), the surface stress decreases monotonically with electrode potential and the PZS shifts to negative values. The model-based results point out that the strain-dependent metal-water interactions provide a microscopic mechanism for controlling both the sign and potential dependence of surface stress, thereby governing the emergence and location of the PZS. Based on this understanding, we set out to interpret the experimental measurements by Ibach et.al.[11] for Au electrodes in $100\mathrm{mM}\ \mathrm{HClO_4}$ aqueous solution, as shown in Figure 33(d). The monotonic decrease in relative surface stress [$g - g\left(E_{\mathrm{pzc}}^{0}\right)$] is at odds with the Parabolic shape of g_{cc} calculated by Schmickler and Levia[12]. Instead, g_{cp} calculated under *constant potential* conditions using the DPFT model reproduces both the magnitude and potential dependence of

the experimental data. The fitted parameters, $\beta_s = 15a_0$ for $\mathrm{Au}(111)$ and $13.5a_0$ $\mathrm{Au}(100)$, indicates that the MWSRI exhibits greater strain sensitivity on $\mathrm{Au}(111)$.

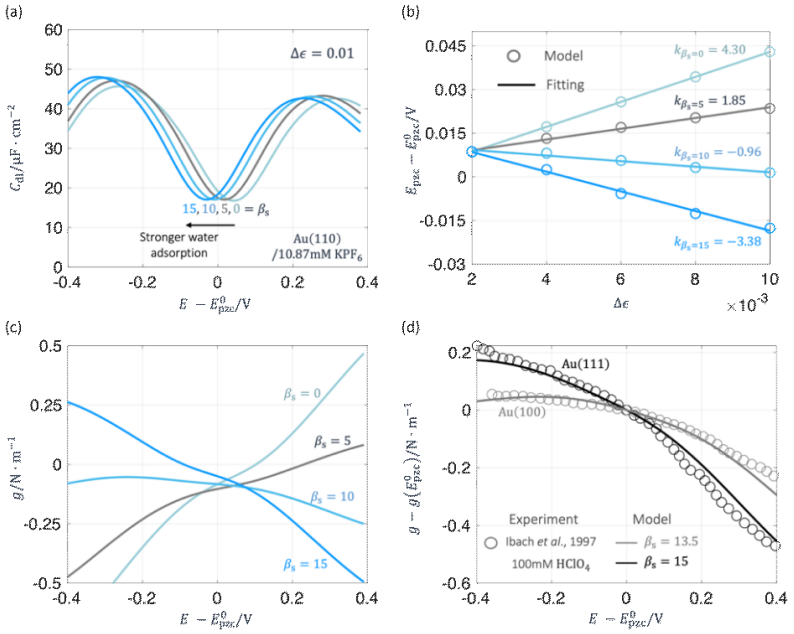

Figure 33. Effect of water adsorption on (a) the C_{dl}, (b) the strain-induced PZC relative to unstrained PZC, and (c) the surface tress g_{cp} and PZS. (d) Comparison of the relative surface stress $[g - g(E^0_{\mathrm{pzc}})]$ between experiment and model for $\mathrm{Au}(111)$ and $\mathrm{Au}(100)$ electrodes in $100\mathrm{mM}\ \mathrm{HClO_4}$ aqueous solution. The water adsorption is modeled by a linear relation between the equilibrium metal-water distance and surface strain, $d_{\mathrm{ms}} = d^0_{\mathrm{ms}} - \beta_s \Delta\epsilon$, where d^0_{ms} denotes the equilibrium distance at zero strain. The parameter β_s (in units of a_0) characterizing the strength of strain-dependence of d_{ms}, with smaller values corresponding to weaker water adsorption and larger values to stronger water adsorption. Results of (a-c) are shown for $\mathrm{Au}(110)$@$10.87\mathrm{mM}\ \mathrm{KPF_6}$ aqueous solution. Experimental surface stress data are measured by Ibach et.al.[11]. Calibrated parameter β_s in (d) are $15a_0$ for $\mathrm{Au}(111)$ and $13.5a_0$ for $\mathrm{Au}(100)$ electrodes.

5.3. Summary

In summary, we have revisited surface stress of solid-liquid interfaces under *constant potential* conditions using the semiclassical density-potential functional theory. Depending on the strain sensitivity of the potential of zero charge, the surface stress may vary monotonically or nonmonotonically with electrode potential. A potential of zero surface stress (PZS) that is generally distinct from the potential of zero charge is defined to characterize the strain-neutral state. By incorporating strain-dependent metal-water short-range interactions, we clarify how interfacial water controls the sign, magnitude, and tunability of surface stress. These findings establish surface stress as a fundamental thermodynamic descriptor of mechanical equilibrium at electrified solid surfaces.

Chapter 6. Semiclassical theory of stepped electrode and step bunching

*Reproduced with minor changes from '**Zhang Z**, Huang J*, Semiclassical Theory of Stepped Electrodes and Step Bunching, In preparation'.*

6.1. Introduction

Atomic steps are among the most catalytically active motifs on metal electrodes and play a decisive role in determining activity, selectivity, and stability in electrocatalysis reactions[57–59,46,169,170,60,61]. Experimental studies on stepped single-crystal electrodes (SSCEs) have shown that reaction rates for key processes, such as hydrogen evolution[169,171–173], oxygen reduction[174,13,175], and small-molecule oxidation[176–178], can vary by orders of magnitude with step density and step geometry. These observations establish step sites as dominant contributors to electrocatalytic performance.

SSCEs provide a controlled model system in which the step density, step orientation, and terrace width can be tuned independently while maintaining atomic precision. SSCE studies have revealed that step sites exhibit distinct adsorption energetics[179–183], altered local electronic structure[180,170], and characteristic work-function shifts relative to terrace atoms[184–186,70,187], leading to measurable changes in voltammetric features and differential double-layer capacitance, C_{dl}. Theoretical studies[188–192], including density functional theory and *ab initio* molecular dynamics simulations, have revealed step-induced charge redistribution, modified water structure, and dipole formation at step edges.

The structural stability of stepped electrodes under electrochemical conditions remains much less explored. Recent experiments have shown that the potential of zero free charge (PZFC) and the catalytic activity deviate from simple linear scaling relationships with the step density when terraces become sufficiently narrow, signaling the emergence of collective electrostatic and mechanical effects at high step densities[13,33]. These deviations have been associated with surface reconstruction and step bunching [193,46,86,87,71]. While step bunching is well understood for vicinal surfaces in vacuum as a consequence of surface free-energy minimization and facet formation[15,193–195], it remains unresolved whether analogous energetically driven processes operate at electrified metal-solution interfaces, where electrostatics, solvation, and ionic screening play central roles.

Herein, we study the EDLs at stepped electrodes and their structural stability by developing a thermodynamic description of stepped metal-solution interfaces under constant-potential conditions

using a semiclassical density-potential functional theoretical (DPFT) model. Following Refs.[74,157], the DPFT model is detailed in the Supplemental Material[196]. Coupling an orbital-free description of metal valence electrons with a statistical filed treatment of the electrolyte, the DPFT constitutes a viable approach to investigate EDLs at more realistic structures, like the EDL at supported nanoparticles[197] and rough surfaces[198]. Applying this approach to SSCEs of Au and Ag in weakly adsorbing electrolytes, we quantify how the step density modifies the EDL, the PZFC, and the surface tension. The surface tension decreases at high step densities and elevated electrode potentials, constituting the thermodynamic driving force for step bunching.

6.2. Parameterization of the DPFT model

We have calibrated the DPFT model against experimental C_{dl} data for flat single-crystal Au and Ag electrodes in weakly adsorbing electrolytes. An extended comparison between model and experiment is shown in Figure 28. The model captures experimental C_{dl} curves across different electrolyte compositions and concentrations for both electrodes, with reasonable parameterization as discussed in the **Chapter 5**.

The model parameterized at flat single-crystal electrodes is then extended to study the influence of steps. Figure 1(a) shows a schematic diagram of the SSCE, characterized by a terrace width l_t and a step height h_s. The step density is defined as $d_t = {l_t}^{-1}$. Periodic boundary conditions are used for the rotated geometry, as shown in the upper-middle panel of Figure 1(a). The flat electrode corresponds to the limiting case of an infinite terrace width ($l_t \to \infty$), as illustrated in Figure 1(b).

Without changing model parameters other than the electrode geometry, the model captures the step-induced negative shift of the PZFCs as observed experimentally on Au[86], Ag[87] and Pt electrodes[199], as shown in Figure 1(c) and (d) for the example of an Au SSCE. Originating from a physical description of metal electrons under constant potential conditions, the capability to capture PZFC changes constitutes an advantage of the DPFT model compared to classical EDL models, jellium models[127,128], and more recent constant-potential molecular dynamics simulations[23,200–203]. Discrepancies are observed in the magnitude of anodic C_{dl} peaks, which are primarily attributed to specific adsorption of fluoride ions. Previous experimental and theoretical studies have shown that weak but non-negligible specific adsorption of F^- ions even on Au surfaces[204–206], which are not considered in this model. Specific adsorption of ions contributes a pesudocapacitance to the measured "C_{dl}", elevating the anodic capacitance peaks[207,205,39].

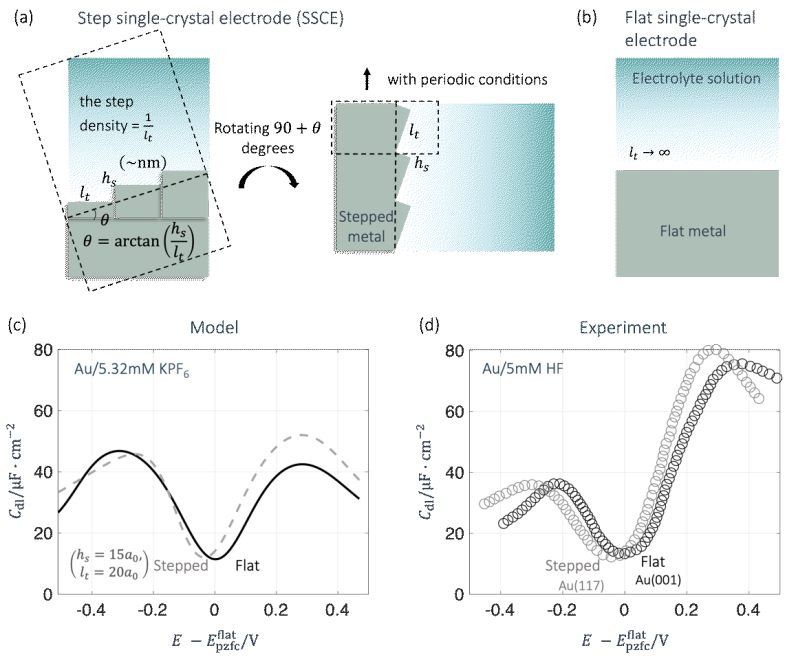

Figure 34. Electrical double layers at stepped single-crystal electrode (SSCE)-solution interfaces. (a) Schematic of a SSCE with terrace width l_t and step height h_s; the step density is defined as $d_t = {l_t}^{-1}$. The upper-middle panel shows the periodic modeling geometry used in this work. (b) Schematic of a flat single-crystal electrode, corresponding to the limiting case of $l_t \to \infty$. Comparison of C_{dl} between flat and stepped electrodes obtained from (c) the DPFT model and (d) experiment. Model results are shown for $h_s = 15a_0$ and $l_t = 20a_0$ with Bohr radius $a_0 = 0.529$ Å. Experimental data are taken from Beltramo et al.[86]. Electrode potentials are referenced to the PZFC of the flat electrode.

6.3. Step-density dependence of PZFC

Extending beyond the specific example shown in Figure 34, we systematically analyze the dependence of the PZFC on step density for stepped Au and Ag electrodes in different electrolytes. In literature, experimental E_{pzfc} was chosen usually as the potential of minimum capacitance (PMC), E_{pmc}, in dilute electrolyte solutions. The model reveals that E_{pzfc} differs from E_{pmc} at stepped electrodes by an amount of ~8 mV. This deviation is intrinsic to the heterogeneous microstructure of the EDL at stepped electrodes, as to be discussed in the next section. Therefore, model-based E_{pzfc} is taken, per definition, as the

potential at which the surface free charge density is zero. The step-density dependent shift in PZFC, relative to the corresponding flat single-crystal electrodes, is denoted as $\Delta E_{\mathrm{pzfc}}(d_t)$. $\Delta E_{\mathrm{pzfc}}(d_t)$ for various values of the step height h_s are presented in Figure 35.

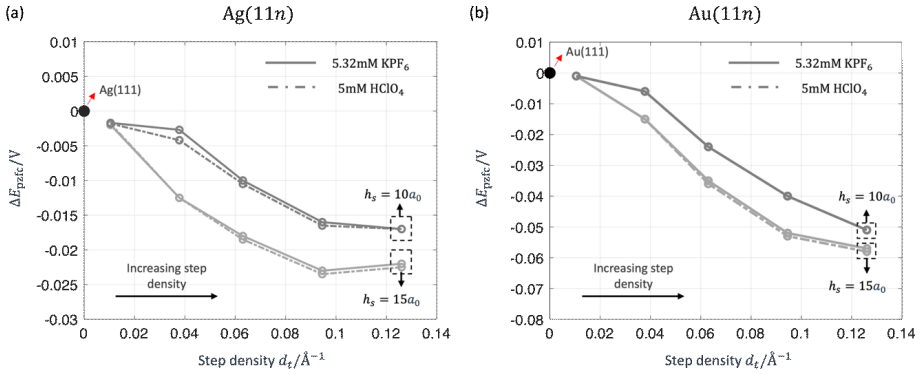

Figure 35. Step density and step height effects on the $\Delta E_{\mathrm{pzfc}}(1/l_t)$. (a) Stepped Ag-solution interfaces. (b) Stepped Au-solution interfaces.

In general, increasing the step density and the step height enhances the electron redistribution between the top and bottom of the step site, leading to larger shifts in ΔE_{pzfc}, as shown in Figure 36.

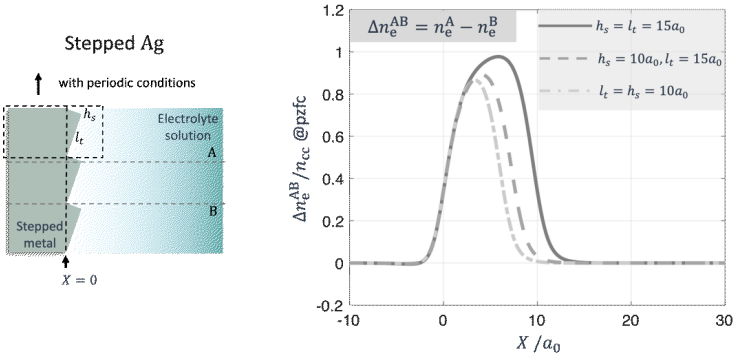

Figure 36. Stepped Ag-solution interface in $5.32\mathrm{mM}$ $\mathrm{KPF_6}$ aqueous solution. The difference of electron density between the position A and B (shown in the left figure) $\Delta n_{\mathrm{e}}^{\mathrm{AB}} = n_{\mathrm{e}}^{\mathrm{A}} - n_{\mathrm{e}}^{\mathrm{B}}$ at different terrace width l_t and step height h_s at the pzfc.

In Figure 37, we compare model predications, inheriting model parameters obtained at flat electrodes without any change, with experimental data using a fixed height of $h_s = 15a_0 = 7.9$ Å. Linear fits are used to quantify the trends.

The model neatly reproduces the experimental observed linear decreases of $\Delta E_{\mathrm{pzfc}}(d_t)$ with increasing step density for both stepped Au and Ag electrodes across different electrolytes[86,87]. From the fitted slopes, $k_{\mathrm{step}}^{\mathrm{Ag}} = -0.2\ \mathrm{V}\cdot\mathrm{Å}$ and $k_{\mathrm{step}}^{\mathrm{Ag}} = -0.44\ \mathrm{V}\cdot\mathrm{Å}$, the step-edge dipole moment p_{step} can be extracted using the linear relation[46],

$$\Delta E_{\mathrm{pzfc}} = -\frac{p_{\mathrm{step}}}{\epsilon_{\mathrm{op}} d_{\mathrm{atom}} l_t}, \tag{116}$$

where ϵ_{op} is the optical permittivity taken $6\epsilon_0$ [70] and $d_{\mathrm{atom}} = 2.89$ Å is the spacing between densely packed atomic rows along [110][86]. The resulting step dipole moments are $p_{\mathrm{step}}^{\mathrm{Ag}} \approx 1.92 \times 10^{-2}\ e_0\cdot\mathrm{Å}$ and $p_{\mathrm{step}}^{\mathrm{Au}} \approx 4.22 \times 10^{-2}\ e_0\cdot\mathrm{Å}$. These values are larger than with previous estimations, $p_{\mathrm{step}}^{\mathrm{Ag}} \approx (3.5 \pm 0.5) \times 10^{-3}\ e_0\cdot\mathrm{Å}$ for Ag in perchlorate electrolytes[87] and $p_{\mathrm{step}}^{\mathrm{Au}} \approx (5-7) \times 10^{-3}\ e_0\cdot\mathrm{Å}$ for Au depending on electrolyte composition[86] because they used vacuum dielectric permittivity in Eq.(116) while we use a more realistic higher value. The results indicate that the step-induced PZFC shifts at Ag and Au SSCEs is mainly caused by the intrinsic redistribution of valence electrons at step edges, which can adequately be captured by the DPFT model. When Au(110) is treated as the limiting high-step-density member of a stepped $(111)\times(111)$-type series, its geometric step density is $d_t \approx 0.30\ \mathrm{Å}^{-1}$. The linear trend between ΔE_{pzfc} and d_t yields $E_{\mathrm{pzfc}} \approx 0.42\ \mathrm{V_{SHE}}$, whereas the measured value is $0.30\ \mathrm{V_{SHE}}$, indicating that Au(110) is beyond the dilute-vicinal regime and that reconstruction or strong step-step interactions contribute to the additional PZFC shift.

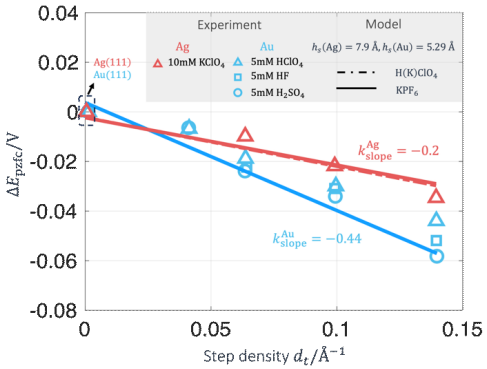

Figure 37. Step-density dependence of the PZFC at stepped electrodes relative to that at flat single-crystal electrodes, $\Delta E_{\mathrm{pzfc}}(d_t)$, in aqueous electrolytes. The model predictions obtained with model parameters calibrated at flat electrodes (solid lines) are compared with experimental data (symbols) taken from ref.[86,87]. The experimental data were obtained on vicinal Au(001) and Ag(001) single-crystal electrodes with controlled step densities, where capacitance-potential curves were measured by impedance spectroscopy and the PZFC values were extracted from the capacitance minima. Model results are shown for a step height $h_s = 7.9$ Å for stepped Ag and $h_s = 5.29$ Å for stepped Au.

We further examined stepped Pt electrodes in Figure 38. In the initial DPFT formulation, the model qualitatively reproduces the decrease of the potential of zero total charge (PZTC) with step density but significantly underestimates its magnitude. Experiments show larger negative shifts that emerge in the hydrogen adsorption region, where faradaic charge and adsorption pseudocapacitance dominate the interfacial response[179–181,183]. As demonstrated by Gómez et al., the measured PZTC of stepped Pt electrodes reflects a convolution of intrinsic step dipoles and step-specific chemisorption, rather than purely electrostatic effects[186]. To account for this contribution, we extended the DPFT framework by incorporating chemisorption effects[97,208]. With this extension, the model reproduces the experimentally observed step-density dependence of the PZTC more accurately, yielding significantly improved agreement with measurements (see Figure 38). These results highlight the important role of adsorption processes in determining the electrochemical response of Pt step edges and demonstrate that their inclusion is essential for quantitatively describing Pt electrodes within the DPFT framework.

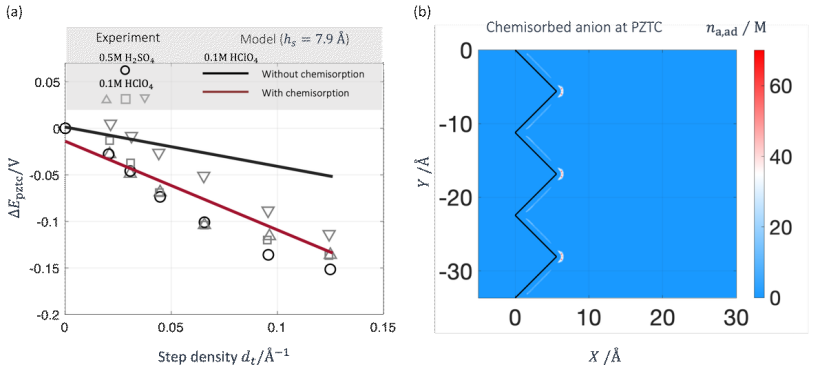

Figure 38. (a) Step-density dependence of the PZTC referenced to the PZTC of flat single crystal electrodes for stepped Pt ($l_t = h_s = 15a_0 = 7.9$ Å) electrodes in $100\text{mM}\ HClO_4$ solution for the case of without and with chemisorption. (b) the chemisorbed anion distribution at the PZTC. The model predictions obtained with model parameters listed in **Table 1-Table 5**(solid line) are compared with experimental data (symbols) taken from ref.[186,199,209]. Model results are shown for a step height $h_s = 7.9$ Å.

6.4. Heterogeneous EDL and its characteristic potentials

The deviation between the PZFC and the PMC points to the heterogeneities of the EDL at stepped metal-solution interfaces which require local PZFCs to properly characterize the heterogenous surface charging conditions.

Figure 39(a-d) shows the EDL microstructure at the PZFC for a representative symmetric stepped Au electrode with $l_t = h_s = 10a_0 = 5.29$ Å in KPF_6 aqueous solution. Electron spills preferentially into the step valleys from the step peaks, known as the Smoluchowski effect[210,211]. Therefore, the electric potential is more positive near the step peaks [Figure 39(a, b)]. This electronic redistribution produces a heterogeneous ionic environment in the EDL at the PZFC, with excess cations in step valleys and excess anions near step peaks [Figure 39(c, d)].

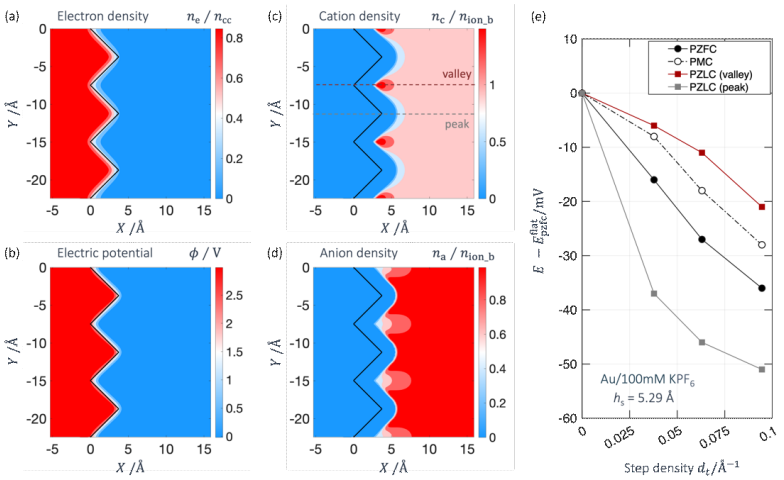

Figure 39. Heterogeneities of the EDL at stepped Au ($l_t = h_s = 10a_0 = 5.29$ Å) in aqueous KPF_6 solution at the PZFC. Spatial distribution of (a) dimensionless electron density $\bar{n}_e$ relative to the metal atomic-core charges n_{cc}, (b) electric potential ϕ, (c) dimensionless cation density $\bar{n}_c$, and (d) dimensionless anion density $\bar{n}_a$, normalized by the bulk ion concentration n_{ion_b}. (e) Step-density dependence of the global PZFC, the potential of minimum capacitance (PMC), and the local potential of zero charge at step valley [PZLC(valley)] and peak [PZLC(peak)], all referenced to the PZFC of the flat single-crystal electrode. Black lines indicate the metallic surface profile in (a)-(d).

The heterogeneous EDL implies that different surface regions reach local charge neutrality at different electrode potentials, similar to the EDL at supported nanoparticles as studied by Zhang et al[197]. Figure 39(e) compares the step-density dependence of the global PZFC, the PMC, and the local PZFCs (PZLC) at the step valley and peak, defined as the potentials at which the net ionic charge integrated along the horizontal direction across the respective valley or peak region vanishes [see dashed lines in Figure 39(c)]. All characteristic potentials decrease monotonically with the step density d_t. However, the PMC is approximately 8 mV more positive than the global PZFC. The PZLC at the step valley is relatively more positive to repel excess cations, whereas the PZLC at the step peak is relatively more negative to repel excess anions. The global PZFC corresponds to a vanishing net surface free charge, whereas the PMC reflects the minimum of the differential electrostatic response. Because the stepped interface exhibits spatially varying electric fields and screening environments, the capacitance minimum is governed by the balance of local valley and peak responses rather than by global charge neutrality. Hence, the PZFC differs

from the PMC, which has been also observed for rough electrodes[198], polycrystalline electrodes[212] and EDLs at supported nanoparticles[197]. This separation is relevant for interpreting structure-sensitive electrochemical behavior because the PMC cannot generally be used as a direct proxy for zero surface charge on stepped electrodes. Even at the global PZFC, valley and peak regions can remain locally polarized, creating distinct local electric fields experienced by adsorbates and reacting species. Thus, the step-density-dependent shifts of PZFC, PMC, and PZLC connect microscopic EDL heterogeneity with capacitance, surface free energy, adsorption energetics, and structural stability.

6.5. Conceptual analysis of step bunching

Inspired by the specific model calculations, we present a conceptual analysis of step density dependence of the surface tension, which is thermodynamically equivalent to excess grand-canonical potential density (see Figure 29). According to electrocapillarity, the surface tension can be expressed, up to a constant, as the integral of surface charge density σ_{free} over the electrode potential, as described by the Lippmann equation[37,95,41]. In this letter, we consider the relative surface tension, $\Delta\gamma_{\mathrm{st}}$, referenced to the PZFC, written as,

$$\Delta\gamma_{\mathrm{st}} = \gamma_{\mathrm{st}} - \gamma_{\mathrm{st}}^{0} = -\int_{E_{\mathrm{pzfc}}}^{E_{\mathrm{M}}} \sigma_{\mathrm{free}} dE, \tag{117}$$

where γ_{st}^{0} denotes the surface tension at the PZFC. Differentiation of $\Delta\gamma_{\mathrm{st}}$ with respect to the step density d_{t} at fixed electrode potential yields,

$$\begin{aligned} \left(\frac{\partial \Delta\gamma_{\mathrm{st}}}{\partial d_t}\right)_E &= -\frac{\partial}{\partial d_t}\int_{E_{\mathrm{pzfc}}}^{E_{\mathrm{M}}} \sigma_{\mathrm{free}} dE \\ &= \sigma_{\mathrm{free}} \frac{\partial E_{\mathrm{pzfc}}}{\partial d_t} - \int_{E_{\mathrm{pzfc}}}^{E_{\mathrm{M}}} \frac{\partial \sigma_{\mathrm{free}}}{\partial d_t} dE. \end{aligned} \tag{118}$$

As shown in Figure 40, the explicit dependence of the surface charge density on the step density is weak over the range considered here, consistent with experimental observations for weakly adsorbing electrolytes[86,87].

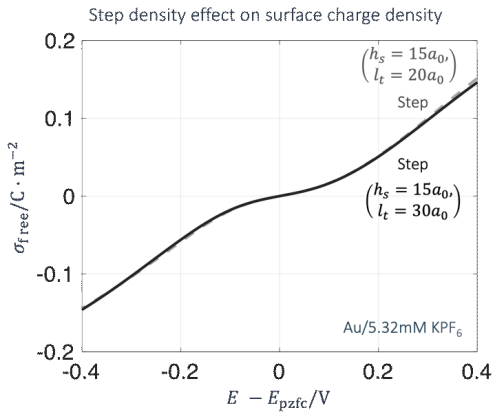

Figure 40. Effect of step density on surface charge density for stepped Ag in $5.32\mathrm{mM}$ $\mathrm{KPF_6}$ solution.

A quantitative evaluation of Eq.(118) using the model yields $\sigma_{\mathrm{free}}\frac{\partial E_{\mathrm{pzfc}}}{\partial d_t}\sim 10^{-1}$, whereas $\int_{E_{\mathrm{pzfc}}}^{E_{\mathrm{M}}}\frac{\partial \sigma_{\mathrm{free}}}{\partial d_t}dE\sim 10^{-3}$. The latter is therefore negligible to leading order, and Eq.(118) is well approximated by,

$$\left(\frac{\partial \Delta\gamma_{\mathrm{st}}}{\partial d_t}\right)_E \approx \sigma_{\mathrm{free}}\frac{\partial E_{\mathrm{pzfc}}}{\partial d_t}. \tag{119}$$

Eq.(119) reveals that the step density dependence of the surface tension is governed by two physically distinct contributions: the surface charge density σ_{free}, which is controlled by the electrode potential and electrolyte properties (e.g., ionic concentration and composition), and the step density dependence of the PZFC, $\frac{\partial E_{\mathrm{pzfc}}}{\partial d_t}$, which is an electrode-specific property. As demonstrated in Figure 37, E_{pzfc} decreases approximately linearly with increasing step density, such that $\frac{\partial E_{\mathrm{pzfc}}}{\partial d_t}$ is negative and nearly constant for a given metal surface. As a result, the relative surface tension $\Delta\gamma_{\mathrm{st}}$ varies approximately linearly with step density, as illustrated schematically in Figure 41(a). Stepped Au electrodes exhibit a larger magnitude of this slope due to their greater sensitivity of the PZFC to step density. A change of $\Delta\gamma_{\mathrm{st}}$ with varying step density implies that configurations with redistributed step density can lower the total interfacial free energy, which constitutes the thermodynamic driving force of step bunching.

As a concrete example, we consider stepped Au electrodes in $10.87\ \mathrm{mM}$ KPF_6 aqueous solution. Figure 41(b) presents a phase diagram of the change in relative surface tension,

$$\Delta\Delta\gamma_{\mathrm{st}} = \Delta\gamma_{\mathrm{st}}^{\mathrm{B}} - \Delta\gamma_{\mathrm{st}}^{\mathrm{A}}, \tag{120}$$

between double-step (B) and single-step (A) configurations, as schematically shown in the inset. A pronounced region with $\Delta\Delta\gamma_{\mathrm{st}} < 0$ emerges at high step density and positive electrode potential, indicating that step bunching is thermodynamically favorable under these conditions.

Ibach and Schmickler developed a phenomenological theory of step instability[193], revealing that the variation of PZFC with step density can drive phase separation of stepped electrodes into step-rich and flat regions. More recently, EC-STM measurements by Koper and co-workers[71] demonstrated that Pt vicinals with high step density spontaneously form bunched structures. Our analysis provides a self-consistent microscopic description of the EDL at stepped electrodes under constant-potential conditions, enabling direct computation of the surface tension as a function of electrode potential and step density. Improving over the phenomenological theory of Ibach and Schmickler[193], the present framework captures spatially resolved charge redistribution and capacitance variations, thereby quantifying the thermodynamic competition between electrostatic driving forces and step-step interactions. The resulting phase diagram identifies the potential window and electrolyte conditions under which step bunching becomes favorable, establishing a direct link between EDL microstructure and morphological instability.

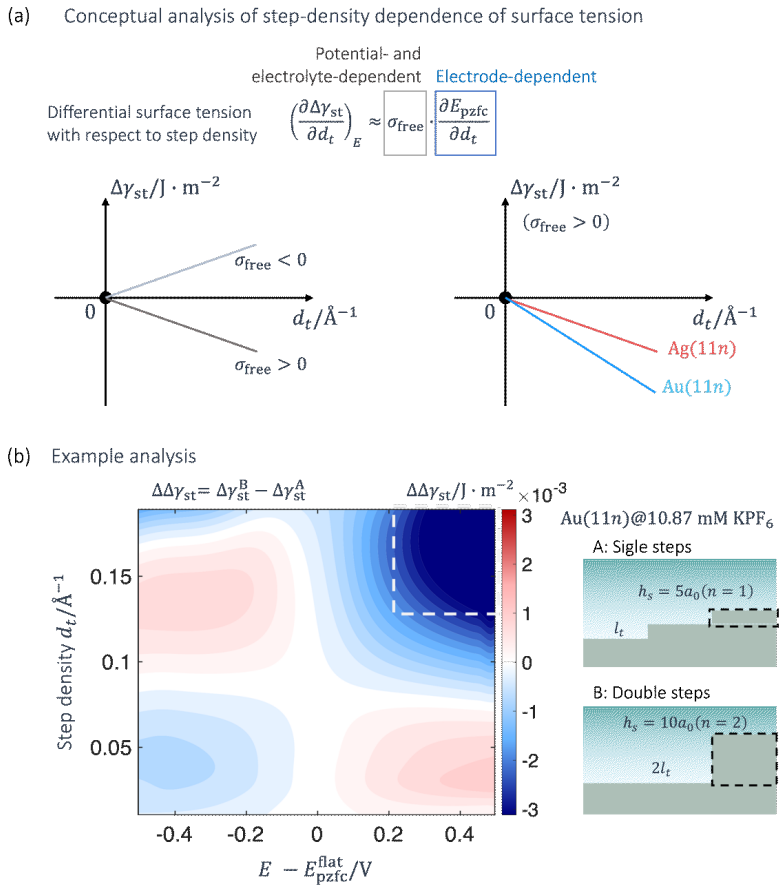

Figure 41. (a) Conceptual illustration of the step density dependence of the relative surface tension $\Delta\gamma_{st}(d_t)$, highlighting its separation into a potential- and electrolyte-dependent surface charge contribution σ_{free} and an electrode-dependent PZFC shift, $\frac{\partial E_{pzfc}}{\partial d_t}$. (b) Phase map of the change in relative surface tension, $\Delta\Delta\gamma_{st} = \Delta\gamma_{st}^B - \Delta\gamma_{st}^A$, between double step (B) and single-step (A) configurations for stepped Au in 10.87mM KPF_6 solution, as a function of step density d_t and electrode potential relative to the PZFC of the flat surface. Negative values indicate a thermodynamic driving force for step bunching. Insets schematically illustrate the single- and double-step geometries.

6.4. Summary

In summary, we employ a semiclassical, hybrid density-potential functional theory (DPFT) to model the EDL at stepped metal-solution interfaces under constant-potential conditions. The theory reproduces and provides microscopic insights into experimental trends in differential capacitance and the nearly linear decrease of the potential of zero free charge (PZFC) with step density for Au and Ag electrodes. Beyond global quantities like PZFC, local potentials of zero charge are defined to describe the essential heterogeneities of the EDL at stepped electrodes. Furthermore, by connecting step-induced shifts in the PZFC to changes in surface tension, we demonstrate that step bunching at high step densities is thermodynamically driven at more positive electrode potentials and modulated by electrolyte composition. In future, chemisorption effects need to be augmented into the DPFT model to provide an adequate description of stepped Platinum electrodes.

Chapter 7. Conclusion and outlook

7.1 Overall conclusions

This PhD project set out to advance the fundamental understanding of electrified metal-electrolyte interfaces by focusing on two closely connected descriptors: the microstructure of electrical double layer (EDL), quantified through the differential double-layer capacitance, C_{dl}, and the mechanical response of the interface, quantified through surface stress, g_{ss}, and interfacial free energy, f_{int}. Motivated by the limitations of classical EDL theories and by the lack of a consistent thermodynamic framework for solid-liquid interfaces under constant-potential conditions, this work developed and applied a semiclassical density-potential functional theory (DPFT) to study interfacial structure, thermodynamics, and morphology over a wide range of electrode potentials and electrolyte compositions.

A central conclusion of this thesis is that classical continuum descriptions, exemplified by the Gouy–Chapman–Stern (GCS) model, are intrinsically limited to a narrow potential window around the potential of zero charge (PZC). While GCS-type models can reproduce experimental capacitance data close to the PZC with suitable fitting parameters, they fail to capture key features observed at highly charged states, including the electrolyte-dependent shifts in PZC, the asymmetric evolution of capacitance at anodic and cathodic potentials, and the pronounced influence of solvent identity. These deficiencies become particularly critical in the potential regimes where technologically relevant electrocatalytic reactions occur.

By contrast, the DPFT framework developed and refined in this work provides a physically grounded and computationally efficient description of electrified interfaces that bridges electronic structure and electrolyte thermodynamics. Through systematic comparison with experimental data, this thesis demonstrates that an accurate description of EDL properties over an extended potential range requires explicit consideration of (i) the metal electrons spillover, (ii) a refined treatment of interfacial permittivity distinguishing free and ion-bound solvent molecules, (iii) potential-dependent short-range metal-solvent interactions, and (iv) partial desolvation of ions at highly charged surfaces. Incorporating these effects enables the DPFT model to reproduce experimental C_{dl} profiles across different cations, anions, solvents, and concentrations with a level of consistency unattainable by classical models.

Beyond EDL structure, this thesis establishes a consistent thermodynamic framework for solid–liquid interfaces based on surface stress rather than surface tension. By explicitly accounting for elastic strain and applying the Shuttleworth equation within the DPFT framework, surface stress can be evaluated under constant-potential conditions in a thermodynamically consistent manner. The results reveal that the potential dependence of surface stress is governed by the strain sensitivity of the potential of zero

charge, leading to either monotonic or nonmonotonic behavior with electrode potential. A new descriptor, the potential of zero surface stress (PZS), is introduced to characterize the strain-neutral state of the interface, and is shown to be generally distinct from the PZC. Furthermore, by incorporating strain-dependent metal-water short-range interactions, this work clarifies the central role of interfacial water in controlling the sign, magnitude, and tunability of surface stress. These findings establish surface stress as a fundamental thermodynamic descriptor of mechanical equilibrium at electrified solid surfaces.

Finally, the DPFT framework is extended to stepped metal-solution interfaces to address the thermodynamic origins of morphology evolution at electrified surfaces. The model successfully reproduces experimental trends in differential capacitance and the nearly linear decrease of the potential of zero free charge (PZFC) with increasing step density for Au and Ag electrodes. Beyond global descriptors, local potentials of zero charge are introduced to capture the intrinsic heterogeneity of the EDL at stepped surfaces. By quantitatively linking step-induced shifts in PZFC to changes in interfacial free energy, this work demonstrates that step bunching at high step densities is thermodynamically driven at more positive electrode potentials and strongly modulated by electrolyte composition. These results highlight the interplay between electronic structure, interfacial thermodynamics, and surface morphology, and establish interfacial free energy as a key descriptor governing stability and structural evolution at stepped electrodes.

Collectively, the results of this thesis provide a coherent picture of electrified metal-solution interfaces in which electrostatic, mechanical, and structural effects are intrinsically coupled. The DPFT framework developed here offers a versatile and physically consistent platform for exploring this coupling under realistic electrochemical conditions.

7.2 Implications for electrocatalysis and interface design

The insights gained in this work have direct implications for electrocatalysis and electrochemical energy technologies. The demonstrated sensitivity of EDL structure and surface stress to electrolyte composition underscores that electrolyte effects cannot be treated as secondary or purely empirical parameters. Instead, ion identity, solvent properties, and concentration actively reshape the interfacial potential landscape, mechanical response, and, ultimately, catalytic performance.

In particular, the ability of the DPFT model to capture EDL behavior at highly charged states is highly relevant for reactions such as the hydrogen evolution reaction and CO_2 reduction, which occur far from the PZC. The observed roles of potential-dependent metal-solvent interactions and ion desolvation suggest that tuning solvent and electrolyte composition provides a powerful lever to control reaction

environments, stabilize reactive intermediates, and mitigate adverse mechanical effects such as stress-induced reconstruction or degradation.

Moreover, the thermodynamic description of stepped surfaces highlights that surface morphology is not static under operating conditions. Instead, it evolves in response to electrochemical driving forces encoded in interfacial free energy. This finding suggests that catalyst design strategies should account not only for the initial surface structure but also for its potential-dependent stability in a given electrolyte environment.

7.3 Limitations of the present work

Despite its advances, the present work has several limitations. First, the DPFT framework relies on a semiclassical description of the electrolyte and an orbital-free treatment of metal electrons. While this enables efficient exploration of large parameter spaces, it necessarily averages over atomistic details. As a result, systems involving strong specific adsorption, exemplified by Pt electrodes, are only qualitatively captured.

Second, the treatment of potential-dependent metal-solvent interactions and ion desolvation is phenomenological, with parameters extracted from fitting experimental capacitance data. Although this approach is physically motivated and yields excellent agreement with experiments, a more direct connection to atomistic simulations or spectroscopic measurements would further strengthen the predictive power of the model.

Finally, the present study focuses on ideally polarizable interfaces and equilibrium thermodynamics. Dynamic effects, such as ion transport, solvent reorganization kinetics, and non-equilibrium surface reconstruction under reaction conditions, are beyond the current scope.

7.4 Outlook and future directions

Several promising directions emerge from this work. A first and natural extension is the incorporation of explicit ion-specific adsorption into the DPFT framework. This development is essential for describing highly active transition-metal electrodes, such as Pt and Cu, and for directly linking EDL structure to catalytic reaction energetics.

Second, coupling the DPFT model with atomistic simulations, such as *ab* initio molecular dynamics or constant-potential DFT, would enable systematic parameterization of short-range interaction terms and desolvation effects. Such multiscale approaches could combine the efficiency of DPFT with the chemical accuracy of first-principles methods.

Third, extending the present equilibrium framework to include kinetic and non-equilibrium phenomena represents an important challenge. Incorporating time-dependent effects, transport, and reaction-induced changes in surface morphology would open the door to modeling realistic operating conditions in electrochemical devices.

Finally, the concepts developed here—particularly the central role of surface stress and interfacial free energy—may be extended beyond electrocatalysis to other solid–liquid systems, including corrosion, electrochemical deposition, and energy storage interfaces. In this broader context, the DPFT framework provides a foundation for a unified thermodynamic description of electrified interfaces that connects microscopic structure to macroscopic function.

In conclusion, this thesis advances both the theoretical methodology and physical understanding of electrified metal-electrolyte interfaces. By bridging EDL structure, interfacial mechanics, and surface morphology within a single consistent framework, it lays the groundwork for rational design and control of electrochemical interfaces in future energy and catalytic technologies.

Table 1. Basic model parameters

Category	Symbol	Item	Value	Note
General constants	R	Ideal gas constant	$8.314\ \mathrm{JK^{-1}mol^{-1}}$	
	k_B	Boltzmann constant	$1.38 \cdot 10^{-23}\ \mathrm{J/K}$	
	T	Temperature	298 K	
	e_0	Elementary charge	$1.6 \times 10^{-19}\mathrm{C}$	
	e_au	Energy constant from arb. units to SI	27.2 eV	
	N_A	Avogadro's number	$6.02 \times 10^{23}/\mathrm{mol}$	
	ϵ_0	Vacuum permittivity	$8.85 \times 10^{-12}\ \mathrm{F/m}$	
	a_0	Bohr radius	5.29×10^{-11} m	
	n_ref	Reference number density	$(a_0)^{-3}$	
	κ	Dimensionless constant	$e_0^2/(k_\mathrm{B}T\epsilon_0 a_0)$	
Electrolyte	v	Bulk volume fraction of solvated ions	$2{a_0}^3 n_0^\mathrm{b}$	
	$\bar{n}_\mathrm{s,total}^{\mathrm{H_2O}}$	Dimensionless total water number density	$5.5 \times 10^4 N_\mathrm{A}(a_0)^3$	Ref[213]
	$\bar{n}_\mathrm{s,total}^{\mathrm{DMSO}}$	Dimensionless total DMSO number density	$1.41 \times 10^4 N_\mathrm{A}(a_0)^3$	Ref[77]

R_{sol}	Diameter of solvent molecule	$1\times10^{10}a_0\left(1/\bar{n}_{\mathrm{s,total}}\right)^{1/3}$ Å	
$r_{\mathrm{Na^+}}^{\mathrm{H_2O}}$	Radius of solvated $\mathrm{Na^+}$ in $\mathrm{H_2O}$	7.5 Å	Fitted from experimental data using the GCS_pm model
$r_{\mathrm{F^-}}^{\mathrm{H_2O}}$	Radius of solvated $\mathrm{F^-}$ in $\mathrm{H_2O}$	3 Å	
$r_{\mathrm{K^+}}^{\mathrm{H_2O}}$	Radius of solvated $\mathrm{K^+}$ in $\mathrm{H_2O}$	6.5 Å	Estimated
$r_{\mathrm{PF_6^-}}^{\mathrm{H_2O}}$	Radius of solvated $\mathrm{PF_6^-}$ in $\mathrm{H_2O}$	4.5 Å	
$r_{\mathrm{K^+}}^{\mathrm{DMSO}}$	Radius of solvated $\mathrm{K^+}$ in DMSO	7 Å	
$r_{\mathrm{PF_6^-}}^{\mathrm{DMSO}}$	Radius of solvated $\mathrm{PF_6^-}$ in DMSO	5 Å	
$r_{\mathrm{Na^+}}^{\mathrm{in,H_2O}}$	Inner-layer radius of solvated $\mathrm{Na^+}$ in $\mathrm{H_2O}$	6.0 Å	Estimated[107,125]
$r_{\mathrm{K^+}}^{\mathrm{in,H_2O}}$	Inner-layer radius of solvated $\mathrm{K^+}$ in $\mathrm{H_2O}$	5.5 Å	
$r_{\mathrm{K^+}}^{\mathrm{in,DMSO}}$	Inner-layer radius of solvated $\mathrm{K^+}$ in DMSO	6.0 Å	
$\gamma_{\mathrm{c/s}}$	Relative size of solvated cations	$(2r_{\mathrm{c}}/R_{\mathrm{s}})^3$	Ref[88]
$\gamma_{\mathrm{a/s}}$	Relative size of solvated anions	$(2r_{\mathrm{a}}/R_{\mathrm{s}})^3$	
$\epsilon_{\mathrm{s}}^{\mathrm{H_2O}}$	Bulk relative permittivity of $\mathrm{H_2O}$	78.5	
$\epsilon_{\mathrm{s}}^{\mathrm{DMSO}}$	Bulk relative permittivity of DMSO	46.8	

	$\chi^{v}_{H_2O}$	Surface potential of H_2O-vacuum interface	0.13 V	Ref[143]
	χ^{v}_{DMSO}	Surface potential of DMSO-vacuum interface	-0.29 V	

Table 2. Parameters in the GCS model

Category	Symbol	Item	Value	Note
Electrolyte	ϵ_H	the relative permittivity within the space between HP and metal surface	6	Ref[214]
	δ_H	The effective distance between HP and metal surface	0.91 Å	Fitted from experimental data using the GCS_pm model

Table 3. Parameters in the DPFT model

Category	Symbol	Item	Value	Note
Electrolyte	$\bar{\epsilon}^{int,H_2O}_{op}$	Optical permittivity of the Hg-aqueous solution interface	3.70	Calibrated with exp. data
	$\bar{\epsilon}^{int,DMSO}_{op}$	Optical permittivity of the Hg-DMSO solution interface	2.74	
	p_s	Solvent dipole moment	$\left[\frac{3(\varepsilon_r-\epsilon^{int}_{op})\epsilon_0 k_B T}{n_{s,total}N_A}\right]$ D	Ref[88]
	χ_v	Volume fraction of vacancy in the bulk solution	0.05	

Metal	$\bar{n}_{\mathrm{cc}}^{0}$	Dimensionless metal electron density of Hg	0.57	
	$\bar{\epsilon}_{\mathrm{op}}^{\mathrm{M}}$	Optical dielectric constant of metal	1	
	θ_{T}	The gradient coefficients tuning the contribution of the semi-local term in kinetic energy	1.53	Calibrated with exp. data

Metal-electrolyte interactions	β_{l}	Coefficient in Morse potential	1	
	D_{ms}^{0}	Force constant of metal-solvent interactions at the PZC	$0.57e_0/k_{\mathrm{B}}T$	Ref[214,215]
	$d_{\mathrm{mH_2O}}^{0}$	Metal-water equilibrium distance at the PZC	3.3 Å	
	$D_{\mathrm{ma(c)}}$	Force constant of metal-ion interactions	$D_{\mathrm{ms}}^{0}/6$	Calibrated with exp. data
	$d_{\mathrm{mNa^+}}$	Metal-$\mathrm{Na^+}$ equilibrium distance in water	4 Å	
	$d_{\mathrm{mK^+}}$	Metal-$\mathrm{K^+}$ equilibrium distance in water	4 Å	
	$d_{\mathrm{mF^-}}$	Metal-$\mathrm{F^-}$ equilibrium distance in water	4 Å	
	$d_{\mathrm{mPF_6^-}}$	Metal-$\mathrm{PF_6^-}$ equilibrium distance in water	3.2 Å	

d^{0}_{mDMSO}	Metal-DMSO equilibrium distance at the PZC	2.8 Å
$d^{\mathrm{DMSO}}_{\mathrm{mK^+}}$	Metal-$\mathrm{K^+}$ equilibrium distance in DMSO	4 Å
$d^{\mathrm{DMSO}}_{\mathrm{mPF_6^-}}$	Metal-$\mathrm{PF_6^-}$ equilibrium distance at PZC in DMSO	4 Å

Table 4. Parameters in the DPFT_sol and DPFT_desol model

Systems	α_{ms}	β_{ms}	ζ_{c}	ζ_{a}
Hg/NaF $\mathrm{H_2O}$	0.05	0.40	0.71	1.11
Hg/KF $\mathrm{H_2O}$			0.34	
Hg/$\mathrm{KPF_6}$ $\mathrm{H_2O}$				0.05
Hg/$\mathrm{KPF_6}$ DMSO	0.05	0.15	0.35	2.35

Some important formulates in the DPFT_sol and DPFT_desol model:

DPFT_sol:

$$D_{\mathrm{ms}} = D^{0}_{\mathrm{ms}} + \alpha_{\mathrm{ms}}\left(E - E_{\mathrm{pzc}}\right)e_0,$$

$$d_{\mathrm{ms}} = d^{0}_{\mathrm{ms}} - \beta_{\mathrm{ms}}\left(E - E_{\mathrm{pzc}}\right)e_0,$$

where D^{0}_{ms} and d^{0}_{ms} are the well depth and the equilibrium distance between the solvent molecule and the metal surface at the PZC, respectively.

DPFT_desol:

$$\frac{\gamma_{\mathrm{i}}}{\gamma^{0}_{\mathrm{i}}} = 1 - \zeta_{\mathrm{i}}(\overline{\nabla}\bar{\phi}),$$

where γ^{0}_{i} is the relative size of solvated ion in solution bulk, ζ_{i} is a relatively dimensionless coefficient indicating the degree of partial desolvation of ion.

Table 5. Parameters in the DPFT_chem model[97,208]

Symbol	Meaning	Value
D_{ca}^{0}	Intercept of the binding strength relation in Eq.**Error! Reference source not found.** of ref[97] at $\tilde{\mu}_e = 0$ eV.	-1.08 eV
α_{ca}	Linear coefficient of the binding strength relation in Eq.**Error! Reference source not found.** of ref[97]	-0.35
β_{ca}	Coefficient in the Morse potential of chemisorbing anions in Eq.**Error! Reference source not found.** of ref[97]	$0.8/a_0$
b_{ca}	Location of the minimum of the Morse potential of chemisorbing anions in Eq.**Error! Reference source not found.** of ref[97]	2.8 Å
Δ^0	Strength of electronic interactions between the metal and chemisorbing anions	2 eV
κ_{Δ}	Coefficient determining the exponential decay of electronic interactions	$1/a_0$
d_{cut}	Cutoff distance of the exponential decays	$5a_0$
$\epsilon_{\mathrm{ca}}^{0}$	Reference energy of the valence orbital of chemisorbing anions	-3.2 eV
Δ_{ϵ}	Overall change of the valence orbital of chemisorbing anions	3 eV
κ_{ϵ}	Coefficient determining the change rate of the valence orbital of chemisorbing anion	$1/a_0$

References

(1) Ganser, M.; Hildebrand, F. E.; Kamlah, M.; McMeeking, R. M. A Finite Strain Electro-Chemo-Mechanical Theory for Ion Transport with Application to Binary Solid Electrolytes. *J. Mech. Phys. Solids* **2019**, *125*, 681–713. https://doi.org/10.1016/j.jmps.2019.01.004.

(2) Gebbie, M. A.; Liu, B.; Guo, W.; Anderson, S. R.; Johnstone, S. G. Linking Electric Double Layer Formation to Electrocatalytic Activity. *ACS Catal.* **2023**, *13* (24), 16222–16239. https://doi.org/10.1021/acscatal.3c04255.

(3) Stewart, E. M.; Narayan, S.; Anand, L. An Electro-Chemo-Mechanical Theory for Hydrogel Ionotronics: Application to Modeling a Capacitive Strain Sensor and a Dynamic Large Strain Actuator. *J. Mech. Phys. Solids* **2023**, *173*, 105196. https://doi.org/10.1016/j.jmps.2022.105196.

(4) Eskandari-Ghadi, M.; Nakagawa, S.; Deng, H.; Pride, S.; Gilbert, B.; Zhang, Y. The Role of Surface Forces in Environment-Enhanced Cracking of Brittle Solids. *J. Mech. Phys. Solids* **2023**, *172*, 105162. https://doi.org/10.1016/j.jmps.2022.105162.

(5) Schott, C. M.; Schneider, P. M.; Song, K.-T.; Yu, H.; Götz, R.; Haimerl, F.; Gubanova, E.; Zhou, J.; Schmidt, T. O.; Zhang, Q.; Alexandrov, V.; Bandarenka, A. S. How to Assess and Predict Electrical Double Layer Properties. Implications for Electrocatalysis. *Chem. Rev.* **2024**. https://doi.org/10.1021/acs.chemrev.3c00806.

(6) Nauman, J. A.; Suvlu, D.; Willard, A. P. Electric Fields at Solid-Liquid Interfaces: Insights from Molecular Dynamics Simulation. *Annu. Rev. Phys. Chem.* **2025**, *76* (Volume 76, 2025), 181–202. https://doi.org/10.1146/annurev-physchem-082820-112101.

(7) Peng, M.; Li, C.; Wang, Z.; Wang, M.; Zhang, Q.; Xu, B.; Li, M.; Ma, D. Interfacial Catalysis at Atomic Level. *Chem. Rev.* **2025**, *125* (4), 2371–2439. https://doi.org/10.1021/acs.chemrev.4c00618.

(8) Di Pasquale, N.; Algaba, J.; Montero De Hijes, P.; Sanchez-Burgos, I.; Tejedor, A. R.; Yeandel, S. R.; Blas, F. J.; Davidchack, R. L.; Espinosa, J. R.; Freeman, C. L.; Harding, J. H.; Laird, B. B.; Sanz, E.; Vega, C.; Rovigatti, L. Solid–Liquid Interfacial Free Energy from Computer Simulations: Challenges and Recent Advances. *Chem. Rev.* **2025**, *125* (10), 5003–5053. https://doi.org/10.1021/acs.chemrev.4c00833.

(9) Wu, J. Understanding the Electric Double-Layer Structure, Capacitance, and Charging Dynamics. *Chem. Rev.* **2022**, *122* (12), 10821–10859. https://doi.org/10.1021/acs.chemrev.2c00097.

(10) Monteiro, M. C. O.; Goyal, A.; Moerland, P.; Koper, M. T. M. Understanding Cation Trends for Hydrogen Evolution on Platinum and Gold Electrodes in Alkaline Media. *ACS Catal.* **2021**, *11* (23), 14328–14335. https://doi.org/10.1021/acscatal.1c04268.

(11) Ibach, H.; Bach, C. E.; Giesen, M.; Grossmann, A. Potential-Induced Stress in the Solid-Liquid Interface: Au(111) and Au(100) in an HClO4 Electrolyte. *Surf. Sci.* **1997**, *375* (1), 107–119. https://doi.org/10.1016/S0039-6028(96)01252-6.

(12) Schmickler, W.; Leiva, E. A Note on the Surface Stress and Tension of Solid Metal Electrodes. *J. Electroanal. Chem.* **1998**, *453* (1–2), 61–67. https://doi.org/10.1016/S0022-0728(98)00133-8.

(13) Kuzume, A.; Herrero, E.; Feliu, J. M. Oxygen Reduction on Stepped Platinum Surfaces in Acidic Media. *J. Electroanal. Chem.* **2007**, *599* (2), 333–343. https://doi.org/10.1016/j.jelechem.2006.05.006.
(14) Gómez-Marín, A. M.; Feliu, J. M. Oxygen Reduction on Nanostructured Platinum Surfaces in Acidic Media: Promoting Effect of Surface Steps and Ideal Response of Pt(111). *Catal. Today* **2015**, *244*, 172–176. https://doi.org/10.1016/j.cattod.2014.05.009.
(15) Baier, S.; Ibach, H.; Giesen, M. The Instability of Vicinal Electrode Surfaces against Step Bunching I: Experiment. *Surf. Sci.* **2004**, *573* (1), 17–23. https://doi.org/10.1016/j.susc.2004.03.075.
(16) Goyal, A.; Koper, M. T. M. The Interrelated Effect of Cations and Electrolyte pH on the Hydrogen Evolution Reaction on Gold Electrodes in Alkaline Media. *Angew. Chem. Int. Ed.* **2021**, *60* (24), 13452–13462. https://doi.org/10.1002/anie.202102803.
(17) Waegele, M. M.; Gunathunge, C. M.; Li, J.; Li, X. How Cations Affect the Electric Double Layer and the Rates and Selectivity of Electrocatalytic Processes. *J. Chem. Phys.* **2019**, *151* (16), 160902. https://doi.org/10.1063/1.5124878.
(18) Zou, A.; Tang, Y.; Wu, C.; Li, J.; Meng, H.; Wang, Z.; Ma, Y.; An, H.; Zhong, H.; Zhang, Q.; Zhang, X.; Xue, J.; Wang, X.; Wu, J. Understanding the Origin of Reconstruction in Transition Metal Oxide Oxygen Evolution Reaction Electrocatalysts. *ChemSusChem* **2024**, *17* (2), e202301195. https://doi.org/10.1002/cssc.202301195.
(19) Ringe, S. Cation Effects on Electrocatalytic Reduction Processes at the Example of the Hydrogen Evolution Reaction. *Curr. Opin. Electrochem.* **2023**, *39*, 101268. https://doi.org/10.1016/j.coelec.2023.101268.
(20) Huang, J.; Chen, Y. Editorial Overview Surface Electrochemistry (2022) The Double Layer: A Persisting Issue with Emerging Trends. *Curr. Opin. Electrochem.* **2022**, *35*, 101099. https://doi.org/10.1016/j.coelec.2022.101099.
(21) Trasatti, S.; Lust, E. The Potential of Zero Charge. In *Modern Aspects of Electrochemistry*; 1999; pp 1–215.
(22) Wang, X.; Kuang, Y.; Le, J.-B. Recent Advances in Calculating Potential of Zero Charge and Helmholtz Capacitance of Metal/Aqueous Solution Interfaces from Ab Initio Molecular Dynamics. *Curr. Opin. Electrochem.* **2023**, *40*, 101341. https://doi.org/10.1016/j.coelec.2023.101341.
(23) Kornyshev, A. A. Double-Layer in Ionic Liquids: Paradigm Change? *J. Phys. Chem. B* **2007**, *111* (20), 5545–5557. https://doi.org/10.1021/jp067857o.
(24) Zhen, E.; Chen, Y.; Huang, J. Double-Layer Capacitance Peaks: Origins, Ion Dependence, and Temperature Effects. *J. Chem. Phys.* **2025**, *162* (14), 144702. https://doi.org/10.1063/5.0251548.
(25) Schwarz, K.; Sundararaman, R. The Electrochemical Interface in First-Principles Calculations. *Surf. Sci. Rep.* **2020**, *75* (2), 100492. https://doi.org/10.1016/j.surfrep.2020.100492.
(26) Doblhoff-Dier, K.; Koper, M. T. M. Electric Double Layer of Pt(111): Known Unknowns and Unknown Knowns. *Curr. Opin. Electrochem.* **2023**, *39*, 101258. https://doi.org/10.1016/j.coelec.2023.101258.
(27) Ojha, K.; Arulmozhi, N.; Aranzales, D.; Koper, M. T. M. Double Layer at the Pt(111)–Aqueous Electrolyte Interface: Potential of Zero Charge and Anomalous Gouy–Chapman

Screening. *Angew. Chem. Int. Ed.* **2020**, *59* (2), 711–715. https://doi.org/10.1002/anie.201911929.
(28) Bender, J. T.; Petersen, A. S.; Østergaard, F. C.; Wood, M. A.; Heffernan, S. M. J.; Milliron, D. J.; Rossmeisl, J.; Resasco, J. Understanding Cation Effects on the Hydrogen Evolution Reaction. *ACS Energy Lett.* **2023**, *8* (1), 657–665. https://doi.org/10.1021/acsenergylett.2c02500.
(29) Le, J.; Iannuzzi, M.; Cuesta, A.; Cheng, J. Determining Potentials of Zero Charge of Metal Electrodes versus the Standard Hydrogen Electrode from Density-Functional-Theory-Based Molecular Dynamics. *Phys. Rev. Lett.* **2017**, *119* (1), 16801. https://doi.org/10.1103/PhysRevLett.119.016801.
(30) Zhang, Z.-M.; Wang, T.; Cai, Y.-C.; Li, X.-Y.; Ye, J.-Y.; Zhou, Y.; Tian, N.; Zhou, Z.-Y.; Sun, S.-G. Probing Electrolyte Effects on Cation-Enhanced CO2 Reduction on Copper in Acidic Media. *Nat. Catal.* **2024**, *7* (7), 807–817. https://doi.org/10.1038/s41929-024-01179-4.
(31) Łukomska, A.; Sobkowski, J. Potential of Zero Charge of Monocrystalline Copper Electrodes in Perchlorate Solutions. *J. Electroanal. Chem.* **2004**, *567* (1), 95–102. https://doi.org/10.1016/j.jelechem.2003.11.063.
(32) Monteiro, M. C. O.; Dattila, F.; López, N.; Koper, M. T. M. The Role of Cation Acidity on the Competition between Hydrogen Evolution and CO2 Reduction on Gold Electrodes. *J. Am. Chem. Soc.* **2022**, *144* (4), 1589–1602. https://doi.org/10.1021/jacs.1c10171.
(33) Helmholtz, H. Ueber Einige Gesetze Der Vertheilung Elektrischer Ströme in Körperlichen Leitern Mit Anwendung Auf Die Thierisch-Elektrischen Versuche. *Ann. Phys.* **1853**, *165* (6), 211–233. https://doi.org/10.1002/andp.18531650603.
(34) Gouy, M. Sur La Constitution de La Charge Électrique à La Surface d'un Électrolyte. *J. Phys. Théorique Appliquée* **1910**, *9* (1), 457–468. https://doi.org/10.1051/jphystap:019100090045700.
(35) Chapman, D. L. LI. A Contribution to the Theory of Electrocapillarity. *Lond. Edinb. Dublin Philos. Mag. J. Sci.* **1913**, *25* (148), 475–481. https://doi.org/10.1080/14786440408634187.
(36) Stern, O. Zur Theorie Der Elektrolytischen Doppelschicht. *Z. Für Elektrochem. Angew. Phys. Chem.* **1924**, *30* (21–22), 508–516. https://doi.org/10.1002/bbpc.192400182.
(37) Grahame, D. C. The Electrical Double Layer and the Theory of Electrocapillarity. *Chem. Rev.* **1947**, *41* (3), 441–501. https://doi.org/10.1021/cr60130a002.
(38) Kornyshev, A. A.; Spohr, E.; Vorotyntsev, M. A. Electrochemical Interfaces: At the Border Line. In *Encyclopedia of Electrochemistry*; John Wiley & Sons, Ltd, 2007. https://doi.org/10.1002/9783527610426.bard010201.
(39) Wang, X.; Liu, K.; Wu, J. Demystifying the Stern Layer at a Metal–Electrolyte Interface: Local Dielectric Constant, Specific Ion Adsorption, and Partial Charge Transfer. *J. Chem. Phys.* **2021**, *154* (12), 124701. https://doi.org/10.1063/5.0043963.
(40) Huang, J. Zooming into the Inner Helmholtz Plane of Pt(111)–Aqueous Solution Interfaces: Chemisorbed Water and Partially Charged Ions. *JACS Au* **2023**, *3* (2), 550–564. https://doi.org/10.1021/jacsau.2c00650.
(41) Linford, R. G. The Derivation of Thermodynamic Equations for Solid Surfaces. *Chem. Rev.* **1978**, *78* (2), 81–95. https://doi.org/10.1021/cr60312a001.

(42) Láng, G.; Heusler, K. E. Problems Related to the Specific Surface Energy of Solid Electrodes. *J. Electroanal. Chem.* **1994**, *377* (1), 1–7. https://doi.org/10.1016/0022-0728(94)03422-2.
(43) Ibach, H. The Role of Surface Stress in Reconstruction, Epitaxial Growth and Stabilization of Mesoscopic Structures. *Surf. Sci. Rep.* **1997**, *29* (5), 195–263. https://doi.org/10.1016/S0167-5729(97)00010-1.
(44) Lipkowski, J.; Schmickler, W.; Kolb, D. M.; Parsons, R. Comments on the Thermodynamics of Solid Electrodes. *J. Electroanal. Chem.* **1998**, *452* (2), 193–197. https://doi.org/10.1016/S0022-0728(98)00136-3.
(45) Kirkwood, J. G.; Buff, F. P. The Statistical Mechanical Theory of Surface Tension. *J. Chem. Phys.* **1949**, *17* (3), 338–343. https://doi.org/10.1063/1.1747248.
(46) *Physics of Surfaces and Interfaces*; Ibach, H., Ed.; SpringerLink Bücher; Springer Berlin Heidelberg: Berlin, Heidelberg, 2006. https://doi.org/10.1007/3-540-34710-0.
(47) Ibach, H.; Schmickler, W. Step Line Tension on a Metal Electrode. *Phys. Rev. Lett.* **2003**, *91* (1), 16106. https://doi.org/10.1103/PhysRevLett.91.016106.
(48) Martinez, R. E.; Augustyniak, W. M.; Golovchenko, J. A. Direct Measurement of Crystal Surface Stress. *Phys. Rev. Lett.* **1990**, *64* (9), 1035–1038. https://doi.org/10.1103/PhysRevLett.64.1035.
(49) Schell-Sorokin, A. J.; Tromp, R. M. Mechanical Stresses in (Sub)Monolayer Epitaxial Films. *Phys. Rev. Lett.* **1990**, *64* (9), 1039–1042. https://doi.org/10.1103/PhysRevLett.64.1039.
(50) Sander, D.; Ibach, H. Experimental Determination of Adsorbate-Induced Surface Stress: Oxygen on Si(111) and Si(100). *Phys. Rev. B* **1991**, *43* (5), 4263–4267. https://doi.org/10.1103/PhysRevB.43.4263.
(51) Láng, G. G.; Sas, N. S.; Vesztergom, S. Experimental Determination of Surface Stress Changes in Electrochemical Systems – Possibilities and Pitfalls. *Chem Biochem Eng Q* **2008**.
(52) Shuttleworth, R. The Surface Tension of Solids. *Proc. Phys. Soc. Sect. A* **1950**, *63* (5), 444. https://doi.org/10.1088/0370-1298/63/5/302.
(53) Mohilner, D. M.; Beck, T. R. Thermodynamic Theory of Electrocapillarity for Solid Metal Electrodes. *J. Phys. Chem.* **1979**, *83* (9), 1160–1166. https://doi.org/10.1021/j100472a011.
(54) Needs, R. J. Calculations of the Surface Stress Tensor at Aluminum (111) and (110) Surfaces. *Phys. Rev. Lett.* **1987**, *58* (1), 53–56. https://doi.org/10.1103/PhysRevLett.58.53.
(55) Fiorentini, V.; Methfessel, M.; Scheffler, M. Reconstruction Mechanism of Fcc Transition Metal (001) Surfaces. *Phys. Rev. Lett.* **1993**, *71* (7), 1051–1054. https://doi.org/10.1103/PhysRevLett.71.1051.
(56) Ibach, H.; Giesen, M.; Ibach, H.; Einstein, T. L. Stress Relief in Reconstruction. *Phys. Rev. Lett.* **1997**, *78* (22), 4225–4228. https://doi.org/10.1103/PhysRevLett.78.4225.
(57) Bartelt, N. C.; Einstein, T. L.; Williams, E. D. The Influence of Step-Step Interactions on Step Wandering. *Surf. Sci.* **1990**, *240* (1), L591–L598. https://doi.org/10.1016/0039-6028(90)90722-K.
(58) Zambelli, T.; Wintterlin, J.; Trost, J.; Ertl, G. Identification of the “Active Sites” of a Surface-Catalyzed Reaction. *Science* **1996**, *273* (5282), 1688–1690. https://doi.org/10.1126/science.273.5282.1688.

(59) Kolb, D. M. Electrochemical Surface Science. *Angew. Chem. Int. Ed.* **2001**, *40* (7), 1162–1181. https://doi.org/10.1002/1521-3773(20010401)40:7%3C1162::AID-ANIE1162%3E3.0.CO;2-F.
(60) Pfisterer, J. H. K.; Liang, Y.; Schneider, O.; Bandarenka, A. S. Direct Instrumental Identification of Catalytically Active Surface Sites. *Nature* **2017**, *549* (7670), 74–77. https://doi.org/10.1038/nature23661.
(61) Gogate, M. R. New Perspectives on the Nature and Imaging of Active Site in Small Metallic Particles: I. Geometric Effects. *Chem. Eng. Commun.* **2021**, *208* (1), 89–109. https://doi.org/10.1080/00986445.2019.1692002.
(62) Kajiwara, R.; Asaumi, Y.; Nakamura, M.; Hoshi, N. Active Sites for the Hydrogen Oxidation and the Hydrogen Evolution Reactions on the High Index Planes of Pt. *J. Electroanal. Chem.* **2011**, *657* (1), 61–65. https://doi.org/10.1016/j.jelechem.2011.03.011.
(63) Calle-Vallejo, F.; Tymoczko, J.; Colic, V.; Vu, Q. H.; Pohl, M. D.; Morgenstern, K.; Loffreda, D.; Sautet, P.; Schuhmann, W.; Bandarenka, A. S. Finding Optimal Surface Sites on Heterogeneous Catalysts by Counting Nearest Neighbors. *Science* **2015**, *350* (6257), 185–189. https://doi.org/10.1126/science.aab3501.
(64) Ha, Y.; Oberst, J. L.; Zeng, Z.; Hoang, T. T. H.; Cohen, Y.; Wetzel, D. J.; Nuzzo, R. G.; Greeley, J.; Gewirth, A. A. In Situ Surface Stress Measurement and Computational Analysis Examining the Oxygen Reduction Reaction on Pt and Pd. *Electrochimica Acta* **2018**, *260*, 400–406. https://doi.org/10.1016/j.electacta.2017.12.039.
(65) Liang, Y.; McLaughlin, D.; Csoklich, C.; Schneider, O.; S. Bandarenka, A. The Nature of Active Centers Catalyzing Oxygen Electro-Reduction at Platinum Surfaces in Alkaline Media. *Energy Environ. Sci.* **2019**, *12* (1), 351–357. https://doi.org/10.1039/C8EE03228A.
(66) Quan, Z.; Wang, Y.; Fang, J. High-Index Faceted Noble Metal Nanocrystals. *Acc. Chem. Res.* **2013**, *46* (2), 191–202. https://doi.org/10.1021/ar200293n.
(67) Back, S.; Yeom, M. S.; Jung, Y. Active Sites of Au and Ag Nanoparticle Catalysts for CO2 Electroreduction to CO. *ACS Catal.* **2015**, *5* (9), 5089–5096. https://doi.org/10.1021/acscatal.5b00462.
(68) Ni, B.; Wang, X. Face the Edges: Catalytic Active Sites of Nanomaterials. *Adv. Sci.* **2015**, *2* (7), 1500085. https://doi.org/10.1002/advs.201500085.
(69) Hamelin, A.; Stoicoviciu, L.; Doubova, L.; Trasatti, S. Influence of the Crystallographic Orientation of the Surface on the Potential of Zero Charge of Silver Electrodes. *Surf. Sci.* **1988**, *201* (3), L498–L506. https://doi.org/10.1016/0039-6028(88)90488-8.
(70) Juárez, M. F.; Santos, E. Electronic Anisotropy at Vicinal Ag(11n) Surfaces: Work Function Changes Induced by Steps and Hydrogen Adsorption. *J. Phys. Chem. C* **2013**, *117* (9), 4606–4618. https://doi.org/10.1021/jp311531u.
(71) Valls Mascaró, F.; Koper, M. T. M.; Rost, M. J. Step Bunching Instability and Its Effects in Electrocatalysis on Platinum Surfaces. *Nat. Catal.* **2024**, *7* (11), 1165–1172. https://doi.org/10.1038/s41929-024-01232-2.
(72) Liu, G.; Shih, A. J.; Deng, H.; Ojha, K.; Chen, X.; Luo, M.; McCrum, I. T.; Koper, M. T. M.; Greeley, J.; Zeng, Z. Site-Specific Reactivity of Stepped Pt Surfaces Driven by Stress Release. *Nature* **2024**, *626* (8001), 1005–1010. https://doi.org/10.1038/s41586-024-07090-z.

(73) Sakong, S.; Huang, J.; Eikerling, M.; Groß, A. The Structure of the Electric Double Layer: Atomistic versus Continuum Approaches. *Curr. Opin. Electrochem.* **2022**, *33*, 100953. https://doi.org/10.1016/j.coelec.2022.100953.
(74) Huang, J. Density-Potential Functional Theory of Electrochemical Double Layers: Calibration on the Ag(111)-KPF_6 System and Parametric Analysis. *J. Chem. Theory Comput.* **2023**, *19* (3), 1003–1013. https://doi.org/10.1021/acs.jctc.2c00799.
(75) Bruch, N.; Eikerling, M.; Huang, J. Density-Potential Functional Theory of Metal-Solution Interfaces. In *Encyclopedia of Solid-Liquid Interfaces*; Elsevier, 2024; pp 308–331. https://doi.org/10.1016/B978-0-323-85669-0.00138-0.
(76) Zhang, Z.; Huang, J. Microstructure of Electrical Double Layers at Highly Charged States. *JACS Au* **2025**. https://doi.org/10.1021/jacsau.5c00508.
(77) Tang, W.; Zhao, S.; Huang, J. Origin of Solvent Dependency of the Potential of Zero Charge. *JACS Au* **2023**, *3* (12), 3381–3390. https://doi.org/10.1021/jacsau.3c00552.
(78) Grahame, D. C.; Soderberg, B. A. Ionic Components of Charge in the Electrical Double Layer. *J. Chem. Phys.* **1954**, *22* (3), 449–460. https://doi.org/10.1063/1.1740089.
(79) Hamelin, A.; Stoicoviciu, L. Study of Gold Low-Index Faces in Kpf, Solutions Part Ii. Analysis of the Experimental Results. *J. Electroanal. Chem. Interfacial Electrochem.* **1987**.
(80) Hamelin, A.; Stoicoviciu, L. Study of Gold Low Index Faces in KPF6 solutionsPART I. EXPERIMENTAL BEHAVIOUR AND DETERMINATION OF THJ3 POINTS OF ZERO CHARGE. *J. Electroanal. Chem. Interfacial Electrochem.* **1987**, *234* (1), 93–105. https://doi.org/10.1016/0022-0728(87)80164-X.
(81) Samec, Z.; Doblhofer, K. Mechanism of Peroxodisulfate Reduction at a Polycrystalline Gold Electrode. *J. Electroanal. Chem.* **1994**, *367* (1), 141–147. https://doi.org/10.1016/0022-0728(93)03041-M.
(82) Hamelin, A.; Stoicoviciu, L.; Silva, F. The Temperature Dependence of the Double-Layer Properties of Gold Faces in Perchloric Acid Solutions: Part II. The (110) Gold Face. *J. Electroanal. Chem. Interfacial Electrochem.* **1987**. https://doi.org/https://doi.org/10.1016/0022-0728(87)88033-6.
(83) Valette, G. Double Layer on Silver Single-Crystal Electrodes in Contact with Electrolytes Having Anions Which Present a Slight Specific Adsorption PART I. THE (110) FACE. *J. Electroanal. Chem. Interfacial Electrochem.* **1981**, *122*, 285–297. https://doi.org/10.1016/S0022-0728(81)80159-3.
(84) Valette, G. Double Layer on Silver Single Crystal Electrodes in Contact with Electrolytes Having Anions Which Are Slightly Specifically Adsorbed: Part II. The (100) Face. *J. Electroanal. Chem. Interfacial Electrochem.* **1982**, *138* (1), 37–54. https://doi.org/10.1016/0022-0728(82)87126-X.
(85) Valette, G. Double Layer on Silver Single Crystal Electrodes in Contact with Electrolytes Having Anions Which Are Slightly Specifically Adsorbed: Part III. The (111) Face. *J. Electroanal. Chem. Interfacial Electrochem.* **1989**, *269* (1), 191–203. https://doi.org/10.1016/0022-0728(89)80112-3.
(86) Beltramo, G. L.; Ibach, H.; Giesen, M. A Novel Approach to Measure the Step Line Tension and the Step Dipole Moment on Vicinal Au(001) Electrodes. *Surf. Sci.* **2007**, *601* (8), 1876–1885. https://doi.org/10.1016/j.susc.2007.02.012.

(87) Beltramo, G. L.; Ibach, H.; Linke, U.; Giesen, M. Determination of the Step Dipole Moment and the Step Line Tension on Ag(001) Electrodes. *Electrochimica Acta* **2008**, *53* (23), 6818–6823. https://doi.org/10.1016/j.electacta.2008.01.032.
(88) Huang, J.; Chen, S.; Eikerling, M. Grand-Canonical Model of Electrochemical Double Layers from a Hybrid Density–Potential Functional. *J. Chem. Theory Comput.* **2021**, *17* (4), 2417–2430. https://doi.org/10.1021/acs.jctc.1c00098.
(89) Zhang, M.-K.; Cai, J.; Chen, Y.-X. On the Electrode Charge at the Metal/Solution Interface with Specific Adsorption. *Curr. Opin. Electrochem.* **2022**, *36*, 101161. https://doi.org/10.1016/j.coelec.2022.101161.
(90) Muscat, J. P.; Newns, D. M. Chemisorption on Metals. *Prog. Surf. Sci.* **1978**, *9* (1), 1–43. https://doi.org/10.1016/0079-6816(78)90005-9.
(91) Kornyshev, A. A.; Schmickler, W. On the Coverage Dependence of the Partial Charge Transfer Coefficient. *J. Electroanal. Chem. Interfacial Electrochem.* **1986**, *202* (1), 1–21. https://doi.org/10.1016/0022-0728(86)90104-X.
(92) Schmickler, W.; Guidelli, R. The Partial Charge Transfer. *Electrochimica Acta* **2014**, *127*, 489–505. https://doi.org/10.1016/j.electacta.2014.02.057.
(93) Gibbs, J. W. On the Equilibrium of Heterogeneous Substances. *Am. J. Sci.* **1878**, *3* (96), 441–458. https://doi.org/10.2475/ajs.s3-16.96.441.
(94) Couchman, P. R.; Everett, D. H. A Comment on Certain Parameters and Equations in Surface Thermodynamics. *J. Electroanal. Chem. Interfacial Electrochem.* **1976**, *67* (3), 382–386. https://doi.org/10.1016/S0022-0728(76)80051-4.
(95) Couchman, P. R.; Davidson, C. R. The Lippmann Relation and Surface Thermodynamics. *J. Electroanal. Chem. Interfacial Electrochem.* **1977**, *85* (2), 407–409. https://doi.org/10.1016/S0022-0728(77)80307-0.
(96) Gibbs, J. W. *The Collected Works of J. Willard Gibbs...: Thermodynamics*; Longmans, Green and Company, 1928; Vol. 1.
(97) Huang, J.; Domínguez-Flores, F.; Melander, M. Variants of Surface Charges and Capacitances in Electrocatalysis: Insights from Density-Potential Functional Theory Embedded with an Implicit Chemisorption Model. *PRX Energy* **2024**, *3* (4), 43008. https://doi.org/10.1103/PRXEnergy.3.043008.
(98) Valincius, G. Electrocapillary Equations of Solid Electrodes. *J. Electroanal. Chem.* **1999**, *478* (1), 41–49. https://doi.org/10.1016/S0022-0728(99)00411-8.
(99) Kramer, D. Dependence of Surface Stress, Surface Energy and Surface Tension on Potential and Charge. *Phys Chem Chem Phys* **2008**, *10* (1), 168–177. https://doi.org/10.1039/B710065E.
(100) Valincius, G. Elastic Electrocapillary Properties of Polycrystalline Gold. *Langmuir* **1998**, *14* (21), 6307–6319. https://doi.org/10.1021/la980440s.
(101) Zhang, L.-L.; Li, C.-K.; Huang, J. A Beginners' Guide to Modelling of Electric Double Layer under Equilibrium, Nonequilibrium and AC Conditions. *J Electrochem* **2022**, *28* (2), 4. https://doi.org/https://electrochem.xmu.edu.cn/CN/10.13208/j.electrochem.210847.
(102) Bikerman, J. J. XXXIX. Structure and Capacity of Electrical Double Layer. *Lond. Edinb. Dublin Philos. Mag. J. Sci.* **1942**, *33* (220), 384–397. https://doi.org/10.1080/14786444208520813.

(103) Freise, V. Zur Theorie Der Diffusen Doppelschicht. *Z. Für Elektrochem. Berichte Bunsenges. Für Phys. Chem.* **1952**, *56* (8), 822–827. https://doi.org/10.1002/bbpc.19520560826.
(104) Eigen, M.; Wicke, E. The Thermodynamics of Electrolytes at Higher Concentration. *J. Phys. Chem.* **1954**, *58* (9), 702–714. https://doi.org/10.1021/j150519a007.
(105) Grahame, D. C. Differential Capacity of Mercury in Aqueous Sodium Fluoride Solutions. I. Effect of Concentration at 25°. *J. Am. Chem. Soc.* **1954**, *76* (19), 4819–4823. https://doi.org/10.1021/ja01648a014.
(106) Bockris, J. O.; Devanathan, M. A. V.; Müller, K. On the Structure of Charged Interfaces. In *Electrochemistry*; Elsevier, 1965; pp 832–863. https://doi.org/10.1016/B978-1-4831-9831-6.50068-0.
(107) Rowley, C. N.; Roux, B. The Solvation Structure of Na^+ and K^+ in Liquid Water Determined from High Level *Ab Initio* Molecular Dynamics Simulations. *J. Chem. Theory Comput.* **2012**, *8* (10), 3526–3535. https://doi.org/10.1021/ct300091w.
(108) Valiskó, M.; Boda, D. The Effect of Concentration- and Temperature-Dependent Dielectric Constant on the Activity Coefficient of NaCl Electrolyte Solutions. *J. Chem. Phys.* **2014**, *140* (23), 234508. https://doi.org/10.1063/1.4883742.
(109) Verkroost, A. W. M.; Sluyters-Rehbach, M.; Sluyters, J. H. Evidence for the Occurrence of Specific Adsorption of Fluoride and Bifluoride Ions from Aqueous KF+KHF2 Solutions at Constant Ionic Strength at the Mercury-Solution Interface. *J Electroanal Chem* **1970**, *24* (1), 1–9. https://doi.org/10.1016/S0022-0728(70)80002-X.
(110) Conway, B. E. Individual Solvated Ion Properties and Specificity of Ion Adsorption Effects in Processes at Electrodes. *Chem. Soc. Rev.* **1992**, *21* (4), 253. https://doi.org/10.1039/cs9922100253.
(111) Grahame, D. C. Properties of the Electrical Double Layer at a Mercury Surface. I. Methods of Measurement and Interpretation of Results. *J. Am. Chem. Soc.* **1941**, *63* (5), 1207–1215. https://doi.org/10.1021/ja01850a014.
(112) Baugh, L. M.; Parsons, R. The Adsorption of Potassium Hexafluorophosphate at the Mercury-Water Interface. *J Electroanal Chem* **1972**, *40* (2), 407–417. https://doi.org/10.1016/S0022-0728(72)80386-3.
(113) Mott, N. F.; Parsons, R.; Watts-Tobin, R. J. The Capacity of a Mercury Electrode in Electrolytic Solution. *Philos. Mag.* **1962**, *7* (75), 483–493. https://doi.org/10.1080/14786436208212180.
(114) Hills, G. J.; Reeves, R. M. The Mercury-Aqueous Solution Interface in the Presence of Hexafluorophosphate and Fluoride Ions. *J Electroanal Chem* **1971**, *31* (2), 269–285. https://doi.org/10.1016/S0022-0728(71)80159-6.
(115) Schiffrin, D. J. Specific Adsorption of Fluoride Ions on Mercury and the Structure of the Mercury/Solutions Interface. *Trans. Faraday Soc.* **1971**, *67*, 3318–3342. https://doi.org/10.1039/tf9716703318.
(116) Payne, Richard. The Electrical Double Layer in Dimethyl Sulfoxide Solutions. *J. Am. Chem. Soc.* **1967**, *89* (3), 489–496. https://doi.org/10.1021/ja00979a004.
(117) Tielrooij, K. J.; Garcia-Araez, N.; Bonn, M.; Bakker, H. J. Cooperativity in Ion Hydration. *Science* **2010**, *328* (5981), 1006–1009. https://doi.org/10.1126/science.1183512.

(118) Grahame, D. C. Properties of the Electrical Double Layer at a Mercury Surface. II. The Effect of Frequency on the Capacity and Resistance of Ideal Polarized Electrodes [1]. *J. Am. Chem. Soc.* **1946**, *68* (2), 301–310. https://doi.org/10.1021/ja01206a045.
(119) Dreyer, W.; Guhlke, C.; Landstorfer, M. A Mixture Theory of Electrolytes Containing Solvation Effects. *Electrochem. Commun.* **2014**, *43*, 75–78. https://doi.org/10.1016/j.elecom.2014.03.015.
(120) Perdew, J. P.; Kurth, S. Density Functionals for Non-Relativistic Coulomb Systems in the New Century. In *A Primer in Density Functional Theory*; Fiolhais, C., Nogueira, F., Marques, M. A. L., Eds.; Springer: Berlin, Heidelberg, 2003; pp 1–55. https://doi.org/10.1007/3-540-37072-2_1.
(121) Lundqvist, S.; March, N. H. *Theory of the Inhomogeneous Electron Gas*; Springer Science & Business Media, 2013.
(122) Constantin, L. A.; Fabiano, E.; Della Sala, F. Performance of Semilocal Kinetic Energy Functionals for Orbital-Free Density Functional Theory. *J. Chem. Theory Comput.* **2019**, *15* (5), 3044–3055. https://doi.org/10.1021/acs.jctc.9b00183.
(123) Johnson, P. B.; Christy, R. W. Optical Constants of the Noble Metals. *Phys. Rev. B* **1972**, *6* (12), 4370–4379. https://doi.org/10.1103/PhysRevB.6.4370.
(124) Kuznetsov, A. M.; Ulstrup, J. *Electron Transfer in Chemistry and Biology: An Introduction to the Theory*; John Wiley & Sons Ltd: Chichester, UK, 1999.
(125) Nightingale, E. R. Jr. Phenomenological Theory of Ion Solvation. Effective Radii of Hydrated Ions. *J. Phys. Chem.* **1959**, *63* (9), 1381–1387. https://doi.org/10.1021/j150579a011.
(126) Le, J.; Cuesta, A.; Cheng, J. The Structure of Metal-Water Interface at the Potential of Zero Charge from Density Functional Theory-Based Molecular Dynamics. *J. Electroanal. Chem.* **2018**, *819*, 87–94. https://doi.org/10.1016/j.jelechem.2017.09.002.
(127) Schmickler, W. A Jellium-Dipole Model for the Double Layer. *J. Electroanal. Chem. Interfacial Electrochem.* **1983**, *150* (1), 19–24. https://doi.org/10.1016/S0022-0728(83)80185-5.
(128) Badiali, J. P.; Rosinberg, M. L.; Vericat, F.; Blum, L. A Microscopic Model for the Liquid Metal-Ionic Solution Interface. *J. Electroanal. Chem. Interfacial Electrochem.* **1983**, *158* (2), 253–267. https://doi.org/10.1016/S0022-0728(83)80611-1.
(129) Schmickler, W.; Henderson, D. The Interphase between Jellium and a Hard Sphere Electrolyte. A Model for the Electric Double Layer. *J. Chem. Phys.* **1984**, *80* (7), 3381–3386. https://doi.org/10.1063/1.447092.
(130) Kornyshev, A. A. Metal Electrons in the Double Layer Theory. *Electrochimica Acta* **1989**, *34* (12), 1829–1847. https://doi.org/10.1016/0013-4686(89)85070-4.
(131) Li, L.; Liu, Y.-P.; Le, J.-B.; Cheng, J. Unraveling Molecular Structures and Ion Effects of Electric Double Layers at Metal Water Interfaces. *Cell Rep. Phys. Sci.* **2022**, *3* (2), 100759. https://doi.org/10.1016/j.xcrp.2022.100759.
(132) Ivaništšev, V.; Nazmutdinov, R. R.; Lust, E. A Comparative DFT Study of the Adsorption of H2O Molecules at Bi, Hg, and Ga Surfaces. *Surf. Sci.* **2013**, *609*, 91–99. https://doi.org/10.1016/j.susc.2012.11.009.

(133) Li, C.-Y.; Le, J.-B.; Wang, Y.-H.; Chen, S.; Yang, Z.-L.; Li, J.-F.; Cheng, J.; Tian, Z.-Q. In Situ Probing Electrified Interfacial Water Structures at Atomically Flat Surfaces. *Nat. Mater.* **2019**, *18* (7), 697–701. https://doi.org/10.1038/s41563-019-0356-x.
(134) Xiao-Yu, L.; Cai, Y.-C.; Meng, Z.-D.; Jia, Z.-T.; Ye, J.-Y.; Tian, N.; Zhou, Z.-Y.; Huang, J.; Sun, S.-G.; Wang, T. Probing the Breathing of Reactive Electrical Double Layer. ChemRxiv August 13, 2024. https://doi.org/10.26434/chemrxiv-2024-hrnb5.
(135) Borukhov, I.; Andelman, D.; Orland, H. Steric Effects in Electrolytes: A Modified Poisson-Boltzmann Equation. *Phys. Rev. Lett.* **1997**, *79* (3), 435–438. https://doi.org/10.1103/PhysRevLett.79.435.
(136) Gongadze, E.; Iglič, A. Decrease of Permittivity of an Electrolyte Solution near a Charged Surface Due to Saturation and Excluded Volume Effects. *Bioelectrochemistry* **2012**, *87*, 199–203. https://doi.org/10.1016/j.bioelechem.2011.12.001.
(137) Gongadze, E.; Van Rienen, U.; Kralj-Iglič, V.; Iglič, A. Spatial Variation of Permittivity of an Electrolyte Solution in Contact with a Charged Metal Surface: A Mini Review. *Comput. Methods Biomech. Biomed. Engin.* **2013**, *16* (5), 463–480. https://doi.org/10.1080/10255842.2011.624769.
(138) Wicke, E.; Eigen, M. Über Den Einfluß Des Raumbedarfs von Ionen in Wäßriger Lösung Auf Ihre Verteilung in Elektrischen Feld Und Ihre Aktivitätskoeffizienten. *Z. Für Elektrochem. Berichte Bunsenges. Für Phys. Chem.* **1952**, *56* (6), 551–561. https://doi.org/10.1002/bbpc.19520560607.
(139) Yu, Y.-X.; Wu, J. Structures of Hard-Sphere Fluids from a Modified Fundamental-Measure Theory. *J. Chem. Phys.* **2002**, *117* (22), 10156–10164. https://doi.org/10.1063/1.1520530.
(140) Huang, J. Hybrid Density-Potential Functional Theory of Electric Double Layers. *Electrochimica Acta* **2021**, *389*, 138720. https://doi.org/10.1016/j.electacta.2021.138720.
(141) Cheng, J.; Sprik, M. Alignment of Electronic Energy Levels at Electrochemical Interfaces. *Phys. Chem. Chem. Phys.* **2012**, *14* (32), 11245–11267. https://doi.org/10.1039/C2CP41652B.
(142) Le, J.-B.; Cheng, J. Modeling Electrochemical Interfaces from Ab Initio Molecular Dynamics: Water Adsorption on Metal Surfaces at Potential of Zero Charge. *Curr. Opin. Electrochem.* **2020**, *19*, 129–136. https://doi.org/10.1016/j.coelec.2019.11.008.
(143) Trasatti, S. Interfacial Behaviour of Non-Aqueous Solvents. *Electrochimica Acta* **1987**, *32* (6), 843–850. https://doi.org/10.1016/0013-4686(87)87072-X.
(144) Shandilya, A.; Schwarz, K.; Sundararaman, R. Interfacial Water Asymmetry at Ideal Electrochemical Interfaces. *J. Chem. Phys.* **2022**, *156* (1), 014705. https://doi.org/10.1063/5.0076038.
(145) Marcandalli, G.; Monteiro, M. C. O.; Goyal, A.; Koper, M. T. M. Electrolyte Effects on CO_2 Electrochemical Reduction to CO. *Acc. Chem. Res.* **2022**, *55* (14), 1900–1911. https://doi.org/10.1021/acs.accounts.2c00080.
(146) Nitopi, S.; Bertheussen, E.; Scott, S. B.; Liu, X.; Engstfeld, A. K.; Horch, S.; Seger, B.; Stephens, I. E. L.; Chan, K.; Hahn, C.; Nørskov, J. K.; Jaramillo, T. F.; Chorkendorff, I. Progress and Perspectives of Electrochemical CO_2 Reduction on Copper in Aqueous Electrolyte. *Chem. Rev.* **2019**, *119* (12), 7610–7672. https://doi.org/10.1021/acs.chemrev.8b00705.

(147) Corson, E. R.; Guo, J.; Tarpeh, W. A. ATR-SEIRAS Method to Measure Interfacial pH during Electrocatalytic Nitrate Reduction on Cu. *J. Electrochem. Soc.* **2024**, *171* (4), 046503. https://doi.org/10.1149/1945-7111/ad3a22.
(148) Zaera, F. Probing Liquid/Solid Interfaces at the Molecular Level. *Chem. Rev.* **2012**, *112* (5), 2920–2986. https://doi.org/10.1021/cr2002068.
(149) Le, J.-B.; Chen, A.; Li, L.; Xiong, J.-F.; Lan, J.; Liu, Y.-P.; Iannuzzi, M.; Cheng, J. Modeling Electrified Pt(111)-H $_{ad}$ /Water Interfaces from Ab Initio Molecular Dynamics. *JACS Au* **2021**, *1* (5), 569–577. https://doi.org/10.1021/jacsau.1c00108.
(150) Kornyshev, A. A. Double-Layer in Ionic Liquids: Paradigm Change? *J. Phys. Chem. B* **2007**, *111* (20), 5545–5557. https://doi.org/10.1021/jp067857o.
(151) De Souza, J. P.; Bazant, M. Z. Continuum Theory of Electrostatic Correlations at Charged Surfaces. *J. Phys. Chem. C* **2020**, *124* (21), 11414–11421. https://doi.org/10.1021/acs.jpcc.0c01261.
(152) Lang, N. D.; Kohn, W. Theory of Metal Surfaces: Charge Density and Surface Energy. *Phys. Rev. B* **1970**, *1* (12), 4555–4568. https://doi.org/10.1103/PhysRevB.1.4555.
(153) Lang, N. D. The Density-Functional Formalism and the Electronic Structure of Metal Surfaces. In *Solid State Physics*; Ehrenreich, H., Seitz, F., Turnbull, D., Eds.; Academic Press, 1974; Vol. 28, pp 225–300. https://doi.org/10.1016/S0081-1947(08)60204-0.
(154) Tang, W.; Zhao, S.; Huang, J. Origin of Solvent Dependency of the Potential of Zero Charge. *JACS Au* **2023**, *3* (12), 3381–3390. https://doi.org/10.1021/jacsau.3c00552.
(155) Le, J.; Cuesta, A.; Cheng, J. The Structure of Metal-Water Interface at the Potential of Zero Charge from Density Functional Theory-Based Molecular Dynamics. *J. Electroanal. Chem.* **2018**, *819*, 87–94. https://doi.org/10.1016/j.jelechem.2017.09.002.
(156) Weissmüller, J.; Viswanath, R. N.; Kramer, D.; Zimmer, P.; Würschum, R.; Gleiter, H. Charge-Induced Reversible Strain in a Metal. *Science* **2003**, *300* (5617), 312–315. https://doi.org/10.1126/science.1081024.
(157) Zhang, M.; Chen, Y.; Eikerling, M.; Huang, J. Structured Solvent on a Split Electron Tail: A Semiclassical Theory of Electrified Metal-Solution Interfaces. *Phys. Rev. Appl.* **2025**, *23* (2), 24009. https://doi.org/10.1103/PhysRevApplied.23.024009.
(158) Hamelin, A.; Stoicoviciu, L.; Silva, F. The Temperature Dependence of the Double-Layer Properties of Gold Faces in Perchloric Acid Solutions: Part I. The (210) Gold Face. *J. Electroanal. Chem. Interfacial Electrochem.* **1987**. https://doi.org/https://doi.org/10.1016/0022-0728(87)85134-3.
(159) Valette, G. Hydrophilicity of Metal Surfaces: Silver, Gold and Copper Electrodes. *J. Electroanal. Chem. Interfacial Electrochem.* **1982**, *139* (2), 285–301. https://doi.org/10.1016/0022-0728(82)85127-9.
(160) Schnur, S.; Groß, A. Properties of Metal–Water Interfaces Studied from First Principles. *New J. Phys.* **2009**, *11* (12), 125003. https://doi.org/10.1088/1367-2630/11/12/125003.
(161) Gerischer, H. An Interpretation of the Double Layer Capacity of Graphite Electrodes in Relation to the Density of States at the Fermi Level. *J. Phys. Chem.* **1985**, *89* (20), 4249–4251. https://doi.org/10.1021/j100266a020.
(162) Gerischer, H.; McIntyre, R.; Scherson, D.; Storck, W. Density of the Electronic States of Graphite: Derivation from Differential Capacitance Measurements. *J. Phys. Chem.* **1987**, *91* (7), 1931–1935. https://doi.org/10.1021/j100291a049.

(163) Luque, N. B.; Schmickler, W. The Electric Double Layer on Graphite. *Electrochimica Acta* **2012**, *71*, 82–85. https://doi.org/10.1016/j.electacta.2012.03.083.
(164) Nielsen, H. B.; Adams, D. L. R-Factor Analysis of the Effect of Non-Structural Parameters in LEED, Applied to Al(111). *J. Phys. C Solid State Phys.* **1982**, *15* (3), 615. https://doi.org/10.1088/0022-3719/15/3/026.
(165) Tian, F.; Jinnouchi, R.; Anderson, A. B. How Potentials of Zero Charge and Potentials for Water Oxidation to OH(Ads) on Pt(111) Electrodes Vary with Coverage. *J. Phys. Chem. C* **2009**, *113* (40), 17484–17492. https://doi.org/10.1021/jp905377d.
(166) Kelly, S. R.; Heenen, H. H.; Govindarajan, N.; Chan, K.; Nørskov, J. K. OH Binding Energy as a Universal Descriptor of the Potential of Zero Charge on Transition Metal Surfaces. *J. Phys. Chem. C* **2022**, *126* (12), 5521–5528. https://doi.org/10.1021/acs.jpcc.1c10362.
(167) Groß, A.; Sakong, S. Ab Initio Simulations of Water/Metal Interfaces. *Chem. Rev.* **2022**, *122* (12), 10746–10776. https://doi.org/10.1021/acs.chemrev.1c00679.
(168) Li, L.; Reuter, K.; Hörmann, N. G. Deciphering the Capacitance of the Pt(111)/Water Interface: A Micro- to Mesoscopic Investigation by AIMD and Implicit Solvation. *ACS Electrochem.* **2025**, *1* (2), 186–194. https://doi.org/10.1021/acselectrochem.4c00062.
(169) Santos, E.; Schmickler, W. *Catalysis in Electrochemistry: From Fundamental Aspects to Strategies for Fuel Cell Development*; John Wiley & Sons, 2011.
(170) M. Koper, M. T. Structure Sensitivity and Nanoscale Effects in Electrocatalysis. *Nanoscale* **2011**, *3* (5), 2054–2073. https://doi.org/10.1039/C0NR00857E.
(171) van der Niet, M. J. T. C.; Garcia-Araez, N.; Hernández, J.; Feliu, J. M.; Koper, M. T. M. Water Dissociation on Well-Defined Platinum Surfaces: The Electrochemical Perspective. *Catal. Today* **2013**, *202*, 105–113. https://doi.org/10.1016/j.cattod.2012.04.059.
(172) McCrum, I. T.; Bondue, C. J.; Koper, M. T. M. Hydrogen-Induced Step-Edge Roughening of Platinum Electrode Surfaces. *J. Phys. Chem. Lett.* **2019**, *10* (21), 6842–6849. https://doi.org/10.1021/acs.jpclett.9b02544.
(173) McCrum, I. T.; Koper, M. T. M. The Role of Adsorbed Hydroxide in Hydrogen Evolution Reaction Kinetics on Modified Platinum. *Nat. Energy* **2020**, *5* (11), 891–899. https://doi.org/10.1038/s41560-020-00710-8.
(174) Maciá, M. D.; Campiña, J. M.; Herrero, E.; Feliu, J. M. On the Kinetics of Oxygen Reduction on Platinum Stepped Surfaces in Acidic Media. *J. Electroanal. Chem.* **2004**, *564*, 141–150. https://doi.org/10.1016/j.jelechem.2003.09.035.
(175) Rizo, R.; Herrero, E.; M. Feliu, J. Oxygen Reduction Reaction on Stepped Platinum Surfaces in Alkaline Media. *Phys. Chem. Chem. Phys.* **2013**, *15* (37), 15416–15425. https://doi.org/10.1039/C3CP51642C.
(176) Vidal-Iglesias, F. J.; García-Aráez, N.; Montiel, V.; Feliu, J. M.; Aldaz, A. Selective Electrocatalysis of Ammonia Oxidation on Pt(1 0 0) Sites in Alkaline Medium. *Electrochem. Commun.* **2003**, *5* (1), 22–26. https://doi.org/10.1016/S1388-2481(02)00521-0.
(177) Vidal-Iglesias, F. J.; Solla-Gullón, J.; Montiel, V.; Feliu, J. M.; Aldaz, A. Ammonia Selective Oxidation on Pt(100) Sites in an Alkaline Medium. *J. Phys. Chem. B* **2005**, *109* (26), 12914–12919. https://doi.org/10.1021/jp051269d.
(178) Zhao, X.; Gunji, T.; Kaneko, T.; Yoshida, Y.; Takao, S.; Higashi, K.; Uruga, T.; He, W.; Liu, J.; Zou, Z. An Integrated Single-Electrode Method Reveals the Template Roles of Atomic Steps:

Disturb Interfacial Water Networks and Thus Affect the Reactivity of Electrocatalysts. *J. Am. Chem. Soc.* **2019**, *141* (21), 8516–8526. https://doi.org/10.1021/jacs.9b02049.
(179) Koper, M. T. M.; Lukkien, J. J.; Lebedeva, N. P.; Feliu, J. M.; van Santen, R. A. Adsorbate Interactions and Phase Transitions at the Stepped Platinum/Electrolyte Interface: Experiment Compared with Monte Carlo Simulations. *Surf. Sci.* **2001**, *478* (1), L339–L344. https://doi.org/10.1016/S0039-6028(01)00957-8.
(180) Lebedeva, N. P.; Koper, M. T. M.; Feliu, J. M.; van Santen, R. A. Role of Crystalline Defects in Electrocatalysis: Mechanism and Kinetics of CO Adlayer Oxidation on Stepped Platinum Electrodes. *J. Phys. Chem. B* **2002**, *106* (50), 12938–12947. https://doi.org/10.1021/jp0204105.
(181) M. Koper, M. T. Introductory Lecture Electrocatalysis: Theory and Experiment at the Interface. *Faraday Discuss.* **2009**, *140* (0), 11–24. https://doi.org/10.1039/B812859F.
(182) Stoffelsma, C.; Rodriguez, P.; Garcia, G.; Garcia-Araez, N.; Strmcnik, D.; Marković, N. M.; Koper, M. T. M. Promotion of the Oxidation of Carbon Monoxide at Stepped Platinum Single-Crystal Electrodes in Alkaline Media by Lithium and Beryllium Cations. *J. Am. Chem. Soc.* **2010**, *132* (45), 16127–16133. https://doi.org/10.1021/ja106389k.
(183) Liu, J.; Huang, J. A Mean-Field Model for the Double Layer of Stepped Platinum Single-Crystal Electrodes. *J. Electroanal. Chem.* **2019**, *846*, 113136. https://doi.org/10.1016/j.jelechem.2019.05.018.
(184) Besocke, K.; Krahl-Urban, B.; Wagner, H. Dipole Moments Associated with Edge Atoms; a Comparative Study on Stepped Pt, Au and W Surfaces. *Surf. Sci.* **1977**, *68*, 39–46. https://doi.org/10.1016/0039-6028(77)90187-X.
(185) Ross, P.; Jr. The Role of Defects in the Specific Adsorption of Anions on Pt(111). *J. Chim. Phys.* **1991**, *88*, 1353–1380. https://doi.org/10.1051/jcp/1991881353.
(186) Gómez, R.; Climent, V.; Feliu, J. M.; Weaver, M. J. Dependence of the Potential of Zero Charge of Stepped Platinum (111) Electrodes on the Oriented Step-Edge Density: Electrochemical Implications and Comparison with Work Function Behavior. *J. Phys. Chem. B* **2000**, *104* (3), 597–605. https://doi.org/10.1021/jp992870c.
(187) Kant, R.; Mishra, G. K. Theory for Heterogeneous Electron Transfer Kinetics on Nanocorrugated Atomic Stepped Metal Electrodes. *J. Phys. Chem. C* **2023**, *127* (14), 6884–6899. https://doi.org/10.1021/acs.jpcc.2c08690.
(188) Chen, A.; Le, J.-B.; Kuang, Y.; Cheng, J. Modeling Stepped Pt/Water Interfaces at Potential of Zero Charge with Ab Initio Molecular Dynamics. *J. Chem. Phys.* **2022**, *157* (9). https://doi.org/10.1063/5.0100678.
(189) Chen, X.; McCrum, I. T.; Schwarz, K. A.; Janik, M. J.; Koper, M. T. M. Co-Adsorption of Cations as the Cause of the Apparent pH Dependence of Hydrogen Adsorption on a Stepped Platinum Single-Crystal Electrode. *Angew. Chem. Int. Ed.* **2017**, *56* (47), 15025–15029. https://doi.org/10.1002/anie.201709455.
(190) Li, P.; Liu, Y.; Chen, S. Microscopic EDL Structures and Charge–Potential Relation on Stepped Platinum Surface: Insights from the Ab Initio Molecular Dynamics Simulations. *J. Chem. Phys.* **2022**, *156* (10). https://doi.org/10.1063/5.0080104.
(191) Sun, Y.; Wu, C.-R.; Wang, F.; Bi, R.-H.; Zhuang, Y.-B.; Liu, S.; Chen, M.-S.; H.-L. Zhang, K.; Yan, J.-W.; Mao, B.-W.; Tian, Z.-Q.; Cheng, J. Step-Induced Double-Row Pattern of Interfacial

Water on Rutile TiO 2 (110) under Electrochemical Conditions. *Chem. Sci.* **2024**, *15* (31), 12264–12269. https://doi.org/10.1039/D4SC01952K.
(192) Wang, F.-T.; Liu, X.; Cheng, J. Water Structures and Anisotropic Dynamics at Pt(211)/Water Interface Revealed by Machine Learning Molecular Dynamics. *Mater. Futur.* **2024**, *3* (4), 41001. https://doi.org/10.1088/2752-5724/ad7619.
(193) Ibach, H.; Schmickler, W. The Instability of Vicinal Electrode Surfaces against Step Bunching II: Theory. *Surf. Sci.* **2004**, *573* (1), 24–31. https://doi.org/10.1016/j.susc.2004.04.058.
(194) Williams, E. D.; Bartelt, N. C. Thermodynamics of Surface Morphology. *Science* **1991**, *251* (4992), 393–400. https://doi.org/10.1126/science.251.4992.393.
(195) Moiseeva, M.; Pichardo-Pedrero, E.; Beltramo, G.; Ibach, H.; Giesen, M. Reconstruction on Au(001) Vicinal Surfaces in UHV and in Sulfuric Acid Solution. *Surf. Sci.* **2009**, *603* (4), 670–675. https://doi.org/10.1016/j.susc.2009.01.006.
(196) See Supplemental Material at [ULR Will Be Inserted by Publisher] for the Theoretical Foundations and Parameterizations of the DPFT., (n.d.).
(197) Zhang, Y.; Binninger, T.; Huang, J.; Eikerling, M. H. Theory of Electro-Ionic Perturbations at Supported Electrocatalyst Nanoparticles. *Phys. Rev. Lett.* **2025**, *134* (6), 66201. https://doi.org/10.1103/PhysRevLett.134.066201.
(198) Tang, W.; Liu, J.; Doblhoff-Dier, K.; Huang, J. Mesoscopic Rough Electrical Double Layers. *Phys. Rev. Lett.* **2025**. https://doi.org/10.1103/bwdx-3yf3.
(199) Climent, V.; Attard, G. A.; Feliu, J. M. Potential of Zero Charge of Platinum Stepped Surfaces: A Combined Approach of CO Charge Displacement and N2O Reduction. *J. Electroanal. Chem.* **2002**, *532* (1), 67–74. https://doi.org/10.1016/S0022-0728(02)00849-5.
(200) Budkov, Y. A.; Kolesnikov, A. L. Electric Double Layer Theory for Room Temperature Ionic Liquids on Charged Electrodes: Milestones and Prospects. *Curr. Opin. Electrochem.* **2022**, *33*, 100931. https://doi.org/10.1016/j.coelec.2021.100931.
(201) Mazur, D. A.; Brandyshev, P. E.; Doronin, S. V.; Budkov, Y. A. Understanding the Electric Double Layer at the Electrode–Electrolyte Interface: Part II - Specific Adsorption and Partial Charge Transfer. *Electrochimica Acta* **2026**, *545*, 147660. https://doi.org/10.1016/j.electacta.2025.147660.
(202) Scalfi, L.; Dufils, T.; Reeves, K. G.; Rotenberg, B.; Salanne, M. A Semiclassical Thomas–Fermi Model to Tune the Metallicity of Electrodes in Molecular Simulations. *J. Chem. Phys.* **2020**, *153* (17), 174704. https://doi.org/10.1063/5.0028232.
(203) Wang, Z.; Chen, M.; Wu, J.; Ji, X.; Zeng, L.; Peng, J.; Yan, J.; Kornyshev, A.; Mao, B.; Feng, G. Constant-Potential Modeling of Electrical Double Layers Accounting for Electron Spillover. *Phys. Rev. Lett.* **2025**, *134*. https://doi.org/10.1103/PhysRevLett.134.046201.
(204) Hamelin, A. Study of the (210) Face of Gold in Aqueous Solutions. *J. Electroanal. Chem. Interfacial Electrochem.* **1982**, *138* (2), 395–400. https://doi.org/10.1016/0022-0728(82)85090-0.
(205) Neves, R. S.; Robertis, E. D.; Motheo, A. J. Capacitance Dispersion in EIS Measurements of Halides Adsorption on Au(210). *Electrochimica Acta* **2006**, *51* (7), 1215–1224. https://doi.org/10.1016/j.electacta.2005.06.013.
(206) Adnan, A.; Behjati, S.; Félez-Guerrero, N.; Ojha, K.; Koper, M. T. M. Tracking the Surface Structure and the Influence of Cations and Anions on the Double-Layer Region of a Au(111)

Electrode. *Phys. Chem. Chem. Phys.* **2024**, *26* (32), 21419–21428. https://doi.org/10.1039/D4CP02133A.
(207) Nazmutdinov, R. R.; Zinkicheva, T. T. Adsorption of the Fluoride Ion on the Surface of Various Faces of a Single Crystal of Silver: A Quantum-Chemical Study. *Russ. J. Electrochem.* **2005**, *41* (2), 206–212. https://doi.org/10.1007/s11175-005-0035-x.
(208) Tang, W.; Zhao, S.; Eikerling, M.; Huang, J. Low Parsons–Zobel Slope of Metal–Solution Interfaces: A Theoretical Comparison of Three Causes. *AIChE J.* **2025**, e70133. https://doi.org/10.1002/aic.70133.
(209) Climent, V.; Gómez, R.; Feliu, J. M. Effect of Increasing Amount of Steps on the Potential of Zero Total Charge of Pt(111) Electrodes. *Electrochimica Acta* **1999**, *45* (4), 629–637. https://doi.org/10.1016/S0013-4686(99)00241-8.
(210) Smoluchowski, R. Anisotropy of the Electronic Work Function of Metals. *Phys. Rev.* **1941**, *60* (9), 661–674. https://doi.org/10.1103/PhysRev.60.661.
(211) J., H.; F. K., S.; H., W. *Solid Surface Physics*; Springer, 2006; Vol. 85.
(212) Liu, J.; Doblhoff-Dier, K.; Koper, M. T. M. Modelling the Double Layer of Polycrystalline Electrodes: Capacitance, Potential of Zero Charge, and Parsons–Zobel Plot. *ACS Electrochem.* **2026**, acselectrochem.5c00544. https://doi.org/10.1021/acselectrochem.5c00544.
(213) Gongadze, E.; Velikonja, A.; Perutkova, Š.; Kramar, P.; Maček-Lebar, A.; Kralj-Iglič, V.; Iglič, A. Ions and Water Molecules in an Electrolyte Solution in Contact with Charged and Dipolar Surfaces. *Electrochimica Acta* **2014**, *126*, 42–60. https://doi.org/10.1016/j.electacta.2013.07.147.
(214) Böcker, J.; Gurskii, Z.; Heinzinger, K. Structure and Dynamics at the Liquid Mercury−Water Interface. *J. Phys. Chem.* **1996**, *100* (36), 14969–14977. https://doi.org/10.1021/jp961065k.
(215) Sellers, H.; Sudhakar, P. V. The Interaction between Water and the Liquid-Mercury Surface. *J. Chem. Phys.* **1992**, *97* (9), 6644–6648. https://doi.org/10.1063/1.463668.

Acknowledgement

Time flies. Since the beginning of my PhD journey in 2022, this project has now drawn to a close. Looking back, these years have been filled not only with scientific exploration and challenges, but also with invaluable support, friendship, and personal growth. There are many people to whom I owe my deepest gratitude.

First and foremost, I would like to express my sincerest gratitude to my supervisor, **Jun Huang**. I am deeply thankful for his continuous guidance, patience, and encouragement throughout my doctoral training. Beyond scientific supervision, Jun has always cared about my personal development and well-being. His thoughtful advice on research, communication, and interpersonal relationships has shaped not only my academic thinking but also my outlook on life. His trust and support gave me the confidence to explore challenging research problems independently, and his rigorous yet warm mentoring style has had a lasting influence on me. I am extremely fortunate to have had his as my supervisor.

I would also like to thank **Prof. Michael Eikerling**, the director of the IET-3 institute, for his kind support and insightful discussions. Despite his demanding schedule, he always took the time to engage patiently in our monthly meetings, offering constructive feedback and valuable suggestions. His openness, calm demeanor, and scientific vision created a motivating research environment, for which I am truly grateful.

My sincere thanks go to my dear group members from YIG. **Chenkun**, **Lulu**, and I first met as master's students at Central South University in China in 2018, and it is remarkable that we later reunited in the same research group in Germany. Over nearly eight years of friendship, we have shared countless academic discussions, travels across Europe during Christmas holidays, and many unforgettable moments. Chenkun is honest, reliable, and exceptionally skilled at gathering and analyzing information, while Lulu is thoughtful, warm-hearted, and always willing to help others, whether in research or daily life. Both of you have inspired and supported me during difficult times, and I sincerely wish you all the best in your future careers and lives.

I would also like to thank **Weiqiang**, a former postdoctoral researcher in YIG and now a faculty member at Zhengzhou University in China. Sharing an office with him for nearly two years was a truly enriching experience. He is knowledgeable, cheerful, and generous in sharing ideas, and I learned a great deal from both his scientific insight and positive attitude. I wish him a bright and successful future.

My thanks extend to other group members and colleagues, including **Zixi**, **Xiwei**, **Qiuhan**, **Octavius**, and **Atakan**, all of whom are highly talented and inspiring researchers. I am also grateful to our visiting students **Da** and **Mengke**, whose focus and dedication to research greatly motivated me.

I would like to express my appreciation to **Xinwei** and **Yufan**, PhD students from IET-3, whom I first met in Changsha, China, in 2018. Having started and completed their PhDs earlier than me, they generously shared their experiences and advice on both research and daily life, which was extremely helpful during my own doctoral journey.

Finally, I would like to thank **all other colleagues at IET-3** for creating a supportive, collaborative, and friendly working environment. The discussions, exchanges, and shared experiences at Forschungszentrum Jülich have made my PhD years both productive and memorable.

To everyone who has accompanied and supported me during this journey—thank you. This PhD would not have been possible without you.

Band / Volume 707
Autonomous Image Analysis to Accelerate the Discovery and Integration of Energy Materials
A. Colliard Granero (2026), xiv, 156 pp
ISBN: 978-3-95806-910-7 (Print)
ISBN: 978-3-95806-911-4 (E-Book)

Band / Volume 708
Effect of Soil Mechanical Properties, Root Tip Geometry, and Mucilage on Penetration Restistance to Root Growth
R. K. Janakiram (2026), xxviii, 98 pp
ISBN: 978-3-95806-914-5 (Print)
ISBN: 978-3-95806-915-2 (E-Book)

Band / Volume 709
European Energy Transition – Germany in the Heart of Europe
T. Klütz, P. Dunkel, T. Busch, J. Linssen, D. Stolten (2026), V, 54 pp
ISBN: 978-3-95806-916-9 (Print)
ISBN: 978-3-95806-917-6 (E-Book)

Band / Volume 710
Development of High-Efficiency Perovskite/Silicon Tandem Solar Cells
Q. Yang (2026), 264 pp
ISBN: 978-3-95806-920-6 (Print)
ISBN: 978-3-95806-921-3 (E-Book)

Band / Volume 711
No-Regret-Maßnahmen der integrierten Netzplanung mit Fokus auf Wasserstoff
T. G. Busch (2026), xx, 325 pp
ISBN: 978-3-95806-922-0 (Print)
ISBN: 978-3-95806-923-7 (E-Book)

Band / Volume 712
Data-Driven Modeling for Digital Representations in Energy Systems
M. C. Zimmer (2026), xv, 166 pp
ISBN: 978-3-95806-926-8 (Print)
ISBN: 978-3-95806-927-5 (E-Book)

Band / Volume 713
Towards integrated PV applications: development of lightweight silicon heterojunction solar modules and their damp-heat and UV stability
K. Zhang (2026), iii, 179 pp
ISBN: 978-3-95806-928-2 (Print)
ISBN: 978-3-95806-929-9 (E-Book)

Band / Volume 714
Zinc-Based Catalysts for the Electrochemical CO_2 Reduction
I. Stamatelos (2026), vii, 136 pp
ISBN: 978-3-95806-932-9 (Print)
ISBN: 978-3-95806-933-6 (E-Book)

Band / Volume 715
Charakterisierung innovativer keramischer Materialien für Elektrolysezellen
L. P. Wehner (2026), xiv, 110 pp
ISBN: 978-3-95806-936-7 (Print)
ISBN: 978-3-95806-937-4 (E-Book)

Band / Volume 716
Process Optimization and Scale-Up for $Ba(Zr,Ce,Y)O_{3-\delta}$-Based Proton-Conducting Electrolysis Half-Cells
L.-A. Schäfer (2026), iv, 141 pp
ISBN: 978-3-95806-940-4 (Print)
ISBN: 978-3-95806-941-1 (E-Book)

Band / Volume 717
Kostenoptimale Energieausfälle in erneuerbaren Energiesystemen
D. Franzmann (2026), xix, 235 pp
ISBN: 978-3-95806-942-8 (Print)
ISBN: 978-3-95806-943-5 (E-Book)

Band / Volume 718
***Semiclassical Thermodynamics* of Metal-Solution Interfaces: A Density-Potential Functional Theory Study**
Z. Zhang (2026), 143 pp
ISBN: 978-3-95806-946-6 (Print)
ISBN: 978-3-95806-947-3 (E-Book)

Weitere ***Schriften des Verlags im Forschungszentrum Jülich*** unter
http://wwwzb1.fz-juelich.de/verlagextern1/index.asp

Energie & Umwelt / Energy & Environment
Band / Volume 718
ISBN 978-3-95806-947-3

Mitglied der Helmholtz-Gemeinschaft

JÜLICH
Forschungszentrum